CHAOTIC TRANSPORT IN RYDBERG ATOMS, TRAPPING IN MOLECULES

A Thesis
Presented to
The Academic Faculty

by

Rytis Paškauskas

In Partial Fulfillment
of the Requirements for the Degree
Doctor of Philosophy in the
School of Physics

Georgia Institute of Technology
December 2007

CHAOTIC TRANSPORT IN RYDBERG ATOMS, TRAPPING IN MOLECULES

Approved by:

Predrag Cvitanović, Advisor
School of Physics
Georgia Institute of Technology

Jean Bellissard
School of Mathematics
Georgia Institute of Technology
School of Physics
Georgia Institute of Technology

Turgay Uzer
School of Physics
Georgia Institute of Technology

Markus Kindermann
School of Physics
Georgia Institute of Technology

Kurt Wiesenfeld
School of Physics
Georgia Institute of Technology

Date Approved: 12 November, 2007

To Rūta and Kazimieras, my parents

TABLE OF CONTENTS

DEDICATION iii

LIST OF TABLES vii

LIST OF FIGURES viii

SUMMARY xi

I INTRODUCTION 1

1.1 The crossed-fields problem 1

1.2 Complex energy flow in OCS molecule 4

1.3 Using methods of dynamical systems theory 7

1.4 Outline of the thesis 10

II SOME ASPECTS OF DYNAMICAL SYSTEMS' THEORY 12

2.1 Fundamental concepts 12

2.1.1 Continuous time flows 13

2.2 Phase space and the surface of section 13

2.3 Linearization and Jacobian 15

2.4 Hamiltonian systems 17

2.5 Some techniques used in the method of surface of section 18

2.5.1 Projection $\mathcal{M} \to \mathcal{S}$ 18

2.5.2 Projection $T\mathcal{M} \to T\mathcal{S}$, general and symplectic case. 20

2.5.3 Non-transversal surfaces of section 22

2.6 Methodology of computing periodic orbits 23

2.6.1 Newton's method and shooting algorithm 24

2.7 Zero modes: the Maupertuis principle 25

III CROSSED FIELDS 27

3.1 Static properties of the phase space 27

3.1.1 Hamiltonian and the equations of motion 27

3.1.2 Time reversibility 28

3.1.3 Geometric parameters 29

3.1.4 Boundaries in phase space 30

3.2 Limits of strong fields . . . 32
3.2.1 Strong magnetic field limit . . . 33
3.2.2 Zero magnetic field: Integrable limit . . . 33
3.2.3 Separating transformation, complete solution . . . 34
3.2.4 Definition of h_i and η_3 in general case . . . 36
3.2.5 Planar limit . . . 37
3.2.6 Levi-Civita regularization . . . 40
3.2.7 The perturbation of heteroclinic connection . . . 42
3.3 Boundaries and nodes . . . 49
3.3.1 Symmetry lines . . . 50
3.3.2 Stable and unstable manifolds . . . 50
3.4 Poincaré section(s) . . . 50
IV PERIODIC ORBIT PARTITION OF THE PHASE SPACE OF THE PLANAR CROSSED-FIELDS PROBLEM . . . 52
4.1 Dynamical modes in terms of periodic orbits . . . 54
V NORMALLY HYPERBOLIC INVARIANT MANIFOLDS . . . 63
5.1 Normal hyperbolicity . . . 65
5.2 Normally hyperbolic manifolds . . . 66
5.3 Invariant curves . . . 68
5.4 Numerical implementation . . . 72
5.4.1 Approximation of the linear operators . . . 74
5.5 Accuracy of the eigenvalues . . . 75
5.5.1 Hyperbolic directions . . . 76
5.6 Notes concerning the implementation . . . 77
5.7 Initial conditions . . . 78
5.8 Constraints . . . 80
VI DYNAMICAL SKELETON OF A SADDLE IN CROSSED-FIELDS PROBLEM 82
6.1 Transformations by Lie series and structure of the linearization . . . 82
6.2 The foliation of a saddle by invariant curves . . . 84

VII CHAOS IN THE OCS MOLECULE 86
7.1 The Hamiltonian model 87
7.2 Discrete symmetries 88
7.2.1 Angular symmetries 89
7.2.2 Approximate radial symmetry 90
7.2.3 Surface of section 91
7.3 Observations of trapping and transitions 93
7.3.1 Time-frequency analysis 97
7.4 Periodic orbit choreography in OCS 98
7.5 Trappings and transitions: bottlenecks and mechanisms 103
7.5.1 Calculations: Initial conditions 105
VIII CONCLUSIONS 112
APPENDIX A CROSSED-FIELDS RELATED MATERIAL 114
REFERENCES 117
VITA 125

LIST OF TABLES

7.1 Rotation numbers of the two-dimensional invariant tori at the bifurcation points A, B, C, D shown in Fig. 4. 109

A.1 Physical constants, relevant for scaling to atomic units in the crossed-fields problem. The bottom line shows scaling factor of the magnetic field. 114

A.2 The shortest periodic points in the homoclinic tangle of figure 4.7 to figure 4.11, S_4, planar crossed fields problem. 116

LIST OF FIGURES

2.1 Reduction of the Jacobian $J(x,\tau)$ to derivative of the map $D\mathcal{F}_{\mathcal{S}}(x)$. 21

2.2 Counting problem, caused by nontransversal intersections. 23

3.1 The zero velocity curve of the crossed-fields Hamiltonian 30

3.2 Plots of potential in the planar limit, with $s = 1$, $\mu = 2$. 38

3.3 Plots of frequency ratio $r(a) = \Omega_2(a)/\Omega_1(a)$ versus a for an integrable limit of planar crossed-fields. 39

3.4 Tangecy and symmetry lines in planar crossed-fields Hamiltonian 51

4.1 A chaotic trajectory in the crossed-fields Hamiltonian 52

4.2 Stable and unstable manifold of a hyperbolic fixed point $p(\mathcal{O}_0)$ (solid dot). The other fixed point $p(\mathcal{O}_1)$ is indicated by a hollow dot. Unstable manifold in red, stable in blue. The discontinuities are caused by non-transversality of the surface of section. 53

4.3 Projections of the two principal periodic orbits ($\mathcal{O}_0$ and $\mathcal{O}_1$), describing main dynamical modes of reactive trajectories in the planar crossed-fields problem. Points where orbits intersect the surface of section $\mathcal{S}$ (Eq. (3.99)) are shown as $p(\mathcal{O}_0)$ and $p(\mathcal{O}_1)$. Note that, the (x, p_x) projection of the zero velocity curve (black) does not form a boundary for the trajectories. 54

4.4 A cartoon of the homoclinic tangle generated by the orbit $\mathcal{O}_0$. Shown are half-branches of W^s and W^u which are relevant for the description of symbolic dynamics in the tangle. As a first approximation to the strange attractor, we use the area S_0 (shaded area, right panel) between two branches of W^s and W^u, joining at the *primary intersection point* p_{PIP}. The strange attractor is contained within S_0. $p(\mathcal{O}_1)$ indicates location of the second fixed point. 55

4.5 A cartoon, showing development of S_0 (see Figure 4.4). In the left panel superposed are S_0 (cyan) and $\mathcal{F}_{\mathcal{S}}(S_0)$ (brown). We can notice that the left corner of S_0 starts to stretch, and the top right corner starts to fold. We can conclude that dynamics of S_0 displays "stretch-and-fold" dynamics, which are most salient features of the Smale horseshoe. The right panel shows ${\mathcal{F}_{\mathcal{S}}}^2(S_0)$ (dark gray) superposed with $\mathcal{F}_{\mathcal{S}}(S_0)$ and S_0. We can see that more complex structures emerge, suggesting that the actual orbital dynamics is much more complicated that the Smale horseshoe. In fact we can identify regions in the new lobe that will generate a complete Smale horseshoe (see left panel of Figure 4.6). 56

4.6 Construction of an embedded Smale horseshoe using W^s and W^u of $p(\mathcal{O}_0)$. . 57

4.7 Embedded strange attractor of the planar crossed-fields problem, represented by its fixed points. 58

4.8 Embedded strange attractor with six symbol symbolic dynamics. Left panel: primitive orbits. Right panel: all prime orbits with up to six intersections with $\mathcal{S}$. 59

4.9 Focusing on attractor near elliptic orbit $\mathcal{O}_1$ (a). 60

4.10 Focusing on attractor near elliptic orbit $\mathcal{O}_1$ (a). 61

4.11 Periodic orbits in an attractor, described by 15 symbols 62

6.1 Projections to the surface of section $\mathcal{S}$ of two dimensional tori of crossed-fields Hamiltonian in 3-dof setting. 85

7.1 Space filling model of OCS molecule 86

7.2 Cartoon of the OCS and equipotential surfaces of the potential V given by Eq (Eq. (7.3)) in the (R_1, R_2) plane. 88

7.3 Upper panel: Time-series of one component $P_1(t)$ of a trajectory which is initially close to the periodic orbit $\mathcal{O}_a$. The energy is $E = 0.09\,\text{a. u.}$. Time t is plotted in units of T_0, the period of $\mathcal{O}_a$ ($T_0 = 0.063\,\text{ps} = 2843.88\,\text{a. u.}$). The integration time is approximately $512T_0 = 34\,\text{ps}$. Lower panel: Ridges of the time-frequency decomposition of $P_1(t)$. The frequencies of $P_1(t)$ are denoted ξ_{P_1}, and are represented in units of T_0^{-1}. The gray band locates the transition region. 94

7.4 Upper panel: Time-series of one component $P_1(t)$ of a trajectory which is initially close to the periodic orbit $\mathcal{O}_a$. The energy is $E = 0.1\,\text{a. u.}$. Time t is plotted in units of T_0, the period of $\mathcal{O}_a$ ($T_0 = 0.063\,\text{ps} = 2843.88\,\text{a. u.}$). The integration time is approximately $512T_0 = 34\,\text{ps}$. Lower panel: Ridges of the time-frequency decomposition of $P_1(t)$. The frequencies of $P_1(t)$ are denoted ξ_{P_1}, and are represented in units of T_0^{-1}. The gray band locates the transition region. 95

7.5 Upper panel: Time-series of one component $P_1(t)$ of a trajectory which is initially close to the periodic orbit $\mathcal{O}_e$. The energy is $E = 0.09\,\text{a. u.}$. Time t is plotted in units of T_0, the period of $\mathcal{O}_a$ ($T_0 = 0.063\,\text{ps} = 2843.88\,\text{a. u.}$). The integration time is approximately $512T_0 = 34\,\text{ps}$. Lower panel: Ridges of the time-frequency decomposition of $P_1(t)$. The frequencies of $P_1(t)$ are denoted ξ_{P_1}, and are represented in units of T_0^{-1}. The gray band locates the transition region. 96

7.6 Upper panel: Time-series of one component $P_1(t)$ of a trajectory which is initially close to the periodic orbit $\mathcal{O}_e$. The energy is $E = 0.09\,\text{a. u.}$. Time t is plotted in units of T_0, the period of $\mathcal{O}_a$ ($T_0 = 0.063\,\text{ps} = 2843.88\,\text{a. u.}$). The integration time is approximately $512T_0 = 34\,\text{ps}$. Lower panel: Ridges of the time-frequency decomposition of $P_1(t)$. The frequencies of $P_1(t)$ are denoted ξ_{P_1}, and are represented in units of T_0^{-1}. The gray band locates the transition region. 97

7.7 Elementary ($k = 1$) periodic orbits *ocsOb* (red) and $\mathcal{O}_e$ (black) at $E = 0.01$ in various projections. 99

7.8 Bifurcation and stability diagram of periodic orbit $\mathcal{O}_b$. 100

7.9 Plots of periodic orbit $\mathcal{O}_a$, at $E = 0.10$. 101

7.10 Plots of periodic orbit $\mathcal{O}_b$, at $E = 0.10$. 101

7.11 Bifurcation and stability diagram for orbits $\mathcal{O}_c$, $\mathcal{O}_d$, $\mathcal{O}_e$. 102

7.12 Projections of an orbit $\mathcal{O}_c$ and intersection point with the surface of section $p(\mathcal{O}_c)$ for the $E = 0.10$. 103

7.13 Projections of an orbit $\mathcal{O}_d$ and intersection point with the surface of section $p(\mathcal{O}_d)$ for the $E = 0.10$. 103

7.14 Projections of an orbit $\mathcal{O}_e$ and intersection point with the surface of section $p(\mathcal{O}_e)$ for the $E = 0.10$. 103

7.15 Projections of the trajectory near a periodic orbit $\mathcal{O}_a$ (with period T_0), analyzed in Figure 7.3. The trajectory is represented in (R_1, R_2) plots, broken down into segments, corresponding to the *trapping stage* (left panel) and chaotic stage (center panel). The bottleneck of transition from diffusion to hyperbolicity can be identified as a two-dimensional invariant torus (right panel.) The trajectory is sampled at fixed time intervals $T_0/2$. The orbit $\mathcal{O}_a$ is shown as a solid curve in the center. 107

7.16 Poincaré section of the trajectory near a periodic orbit $\mathcal{O}_a$, analyzed in Figs. 7.3 and Figure 7.5.1. The bottleneck (a two-dimensional torus) is a loop (blue) at the bifurcation point ("D" in Figure 7.17). The trajectory is trapped in the vicinity of a loop (which is clearly seen from the inset). The escape stage is shown as two "tentacles," which extend along the unstable manifolds of a resonant periodic orbit (the five red dots around the center). . 110

7.17 Fine structure of invariant tori, scanned along the transition channel. The plot shows how Lyapunov exponents depend on the rotation number ω. The points of frequency halving bifurcations ("A"– "D") can be interpreted as bottlenecks of transition from diffusion to hyperbolicity. Red dots: family of loops arising from the periodic orbit $\mathcal{O}_a$. Black dots: frequency halved loop, emerging at the bifurcation point "A". Insets display (R_1,P_1) projections of loops near the bifurcation point "A". Red: loop with elliptic normal stability and $\omega = \omega_1 \approx 0.24067$. Black: loop with hyperbolic normal stability and $\omega = \omega_2 = (\omega_1 + 1)/2 \approx 0.62033$. 111

SUMMARY

With this work we have examined what dynamical systems approach is available for the scientist to tackle the formidable problem of describing complex systems and whether conceptual works of mathematics applied to realistic dynamical systems can be practicable and useful. The underlying ideas are grounded in one subject of dynamical systems theory, the periodic orbit theory, which offers formulae to compute averages of chaotic systems with the best accuracy available. On the conceptual level, the theory manages to find a common denominator between such apparently different concepts, as periodic orbits, averages in chaotic systems, spectrum of a Green's operator (asymptotic approximation is involved in the latter).

The price to pay is severe: one has to have means to compute periodic orbits in a given dynamical system.

In this work we develop methods to partition the phase space of a complex two degree of fredom Hamiltonian system, called the planar crossed-fields in terms of periodic orbits. I also have studied extensions to three degree of freedom setting, and discussed relevance of high-dimensional complex saddles.

Finally, we have developed methodology to compute unstable invariant tori in three degree of freedom setting and applied these methods to explain trapping of trajectories in the planar carbonyl-sulfide (OCS) molecule.

CHAPTER I

INTRODUCTION

We investigate chaotic ionization of highly excited hydrogen atom in crossed electric and magnetic fields (Rydberg atom) and intra-molecular relaxation of highly excited planar OCS (both 3-dof Hamiltonian systems).

1.1 The crossed-fields problem

By applying strong electromagnetic fields on an atom, it is possible to promote one or several of its electrons to a high-energy state. Such an electron is loosely bound to the atomic core; this electron spends most of the time at distances from the core so immense, that, if the atom were solid, it could be visible to the naked eye. Electrons in such atoms have extreme properties, they behave almost like classical particles and offer a natural laboratory for the investigation of many physical phenomena which they display with exceptional clarity.

Atoms with such properties are called Rydberg atoms. In Chapter 3 we study classical chaos in such a setting, with hydrogen atoms placed in crossed electric and magnetic fields at right angles (the **crossed-fields** problem).

A quantum state of an electron in a "free" Rydberg atom is approximately hydrogenic [21]. Such states are characterized by very large principal quantum numbers ($n \gtrsim 50$) [61, 46] and Rydberg formula for the energy levels [46] holds. Deviations from the hydrogenic eigenenergies are induced by the screening effect of the charge cloud of the remaining near-core electrons, and are described by the quantum defect δ_l, entering the Rydberg formula as a correction to the principal quantum number n [46].

In these conditions, electrons becomes sensitive to even weak stray laboratory-scale electric fields [7], and dynamical phenomena such as, for example, manifestations of chaos can be studied experimentally [116]. Among experimentally observed phenomena are the quasi-Landau (QL) oscillations in the quantum photo-absorption spectra, high energy chaotic ionization, Ericson fluctuations (closely related to the phenomenon of *chaotic scattering*)

and full spatial localization of electronic wave packets [122]. While low-energy atoms in weak external fields have been studied since the beginning of the modern quantum mechanics (see Zeeman and Stark effects in [9, 14]), only in the past few decades the increases in the level of experimental sophistication have allowed to reach for the realm of Rydberg atoms in strong external fields.

One of the landmark experimental studies is the work of Garton and Tomkins [47] on the oscillations in the photo-absorption spectrum of rubidium atoms in magnetic field. They have detected quasi-Landau (QL) resonance, characterized by the energy spacing

$$\Delta\varepsilon_1 = \gamma(E)\hbar\omega_c\,, \quad (\omega_c = eB/m_e)\,,$$

where the energy dependent factor $\gamma(E)$ was related to a classical two-dimensional periodic orbit of the electron, in particular to its period $T = 2\pi/\gamma_{10}\omega_c$ [110]. It was found, for example, that $\gamma(0) = 1.5$ at the ionization energy $E = 0$. It took the next 13 years to observe the second resonance, with $\gamma_{20} = 0.64$ [63]. Shortly thereafter theoretical investigations of hydrogen in magnetic field (this problem is often called the "Diamagnetic Kepler Problem," or DKP) have revealed that all periodic solutions contribute to the semi-classical spectrum [82] and it took another 10 years to complete this study [112]. As a result of two decades of sustained research [42, 60, 64, 83], this problem has been extensively investigated and theory of photo-absorption of hydrogenic atoms in external fields near the ionization threshold [30, 11, 120] has been developed.

A superficially similar arrangement, resulting from addition of an electric field, perpendicular to the magnetic field (the crossed-fields problem) [109], remains the least understood of all Rydberg problems [118, 116]. The experimental challenge has been taken up in [120, 94, 95], where a class of QL resonances in rubidium Rydberg atoms was identified. Similar to the original resonances in [47], those of the crossed-fields problem were also associated with a small set of planar ($z = 0$) periodic orbits.

Evidence of chaotic scattering in the crossed-fields problem came when Main and Wunner detected Ericson fluctuations in the quantum spectrum [84], which was further asserted from experiments with ionization of hydrogen in circularly polarized fields [16] – a problem

intimately connected to the crossed-fields. In experimental work on localization of electronic wave packets in all three spatial dimensions [122], observations have led to new insights into the dynamics of the electron in the correspondence principle regime.

And so, the Rydberg atoms allow us to enter the elusive domain of semiclassical physics. It has been known from studies of the asymptotic behavior of the wave equation [4, 5], the simplest variant of the Schrödinger's equation and the Gutzwiller's trace formula [55, 56] that periodic orbits play a central role in the spectrum. Furthermore, almost inevitably, when Rydberg atom is placed in external fields, part of its classical Hamiltonian dynamics is "chaotic." In crossed-fields problem the chaotic dynamics are mixed with regular. The three dimensionality of this problem makes it still very obscure and uncharted terrain, even when only the classical dynamics is considered. This problem is so complex because no continuous symmetry survives the extensive symmetry breaking induced by the two fields.

Relativistic corrections have been shown to play a minor role in the crossed-fields problem, therefore the Hamiltonian H in scaled units (for scaling, see Appendix A.1, Eq. (3.1) and Chapter 3) can be written as

$$H = p^2/2 + BL_z/2 + B^2\rho^2/8 - 1/r + Fx, \tag{1.1}$$

where $p^2 = p_x^2 + p_y^2 + p_z^2$, $\rho^2 = x^2 + y^2$, $L_z = p_y x - p_x y$, $r = \sqrt{x^2 + y^2 + z^2}$. The perturbative regime of classical dynamics was studied using Kepler orbits as unperturbed states of Hamiltonian with $F = B = 0$ in [109], and later in [53] using the Kustaanheimo-Stiefel regularization procedure [72, 111]. The action-angle representation, found in [53] showed that the principal quantum number of the unperturbed problem n remains a "good" approximate quantum number. The dynamics of trajectories with small, nonzero F and B was interpreted as if regular in the n manifold and slowly mixing (Arnol'd diffusion) between the manifolds. The intra-manifold chaos and the diffusion along the resonance channels were investigated in [119]. Geometric analysis of the lowest nontrivial terms in the normal form has revealed that a nontrivial *phase space topology* is present even in the vanishing fields limit [100, 22]. Systematic studies of periodic orbits in the crossed-fields problem start with [38], where four periodic orbits were identified, labeled by S_{Sp}, S_+, S_-, $S_\perp$ and an

analogy with orbits in the three-body problem was drawn.

To summarize; in the crossed-fields the external electromagnetic fields couple to atomic fields, as if by attaching "handles" to them, and by probing the atoms we are provided with a unique experimental glimpse into the fundamental phenomena that arise when quantum meets classical. The prominence of this paradigm in diverse areas of physics range from atoms and molecules, to excitonic systems, to plasmas and neutron stars [29, 101]. Both its theoretical features and experimental accessibility are the basis of the continually renewed interest in this problem.

1.2 Complex energy flow in OCS molecule

Chemical reactions typically proceed through a complex choreography of energy flow processes that deliver the needed vibrational energy to the reactive mode. The manner and time in which energy travels determine the outcome of the reaction and the properties of the products. The conventional wisdom concerning this fundamental process is that vibrational energy travels very fast, and well before a reaction takes place, it distributes itself statistically among the modes of the molecule, assumed to resemble an ensemble of coupled oscillators. Reaction rate theories based on these assumptions, known collectively as statistical theories [91], have been vindicated in a number of chemical reactions. However, there is increasing evidence that the approach to equilibrium usually proceeds more slowly than predicted by statistical theories [37] and also that it is nonuniform, proceeding by intriguing fits and starts. This anomalous diffusion is caused by variety of phase space structures, such as resonant islands or tori [123] that can strongly slow down the trajectories passing nearby [123, 102], and therefore are said to be "sticky" [92]. To date, the theories so successfully applied in pioneering works [26, 27, 54, 86, 106] to lower-dimensional systems have not been extended beyond 2 degrees of freedom (dof) due to severe technical difficulties [50, 51, 114].

In Chapter 7 we investigate these phenomena in carbonyl sulfide (OCS) molecule. This chemical compound is a major pollutant and an ingredient of "biogeochemical cycle of sulfur" and "greenhouse effect". Its relevance has increased together with the increasing level

of emission, caused by anthropogenic activities (combustion and agriculture [115]). Because the breakup energy of its "weaker" C-S is low, OCS is a highly reactive compound. Describing precise reaction scenarios and the reaction rates remains a problem of great practical importance.

Answering the question of *how vibrational energy flows in molecules* succinctly seems a hopeless task, considering complexity of inter-atomic interactions in a molecule. The statistical (or RRKM) theories [52, 96, 40, 91] posited an answer: Vibrational energy travels "very fast", distributes among the vibrational modes, and reaches a statistical equilibrium well before a reaction takes place. Such theories remain a tool of chemists to this day. Origins of this assumption lie the ansatz of molecular chaos (see Section 1.3) and the successes of thermodynamics have established firmly this ansatz. Nevertheless, there is an increasing body of evidence that processes in high dimensional systems that violates this ansatz. The doubts into validity of the molecular chaos assumption were set in motion with the work of Fermi-Pasta-Ulam [36, 37]. Soon thereafter, studies of small perturbations of integrable Hamiltonian systems – the Kolmogorov-Arnol'd-Moser theory [70, 71, 1] (see also Section 1.3) uncovered a generic mechanism of how the metric transitivity fails.

It is commonly assumed that in "typical" Hamiltonian systems with N degrees of freedom with N large, in the thermodynamic $N \to \infty$ limit the relative measure of N-dimensional invariant tori (N local integrals) tend to either zero or one [43]. The implication is that chaotic systems with large N approach conditions of the stochastic ansatz, and hence that the trapping phenomenon described in Chapter 7 is insignificant. On the other hand, it has been established recently that high order resonances form robust islands of secondary structures with positive measure [59].

Models of OCS have served as a test-bed for studying intra-molecular dynamics in the chaotic regime [17] and these classical findings have been confirmed in parallel quantal wave packet calculations [49]. In Chapter 7 we use the Hamiltonian [39], Eq. (7.1)

$$H = T(R_1, R_2, \alpha, P_1, P_2, P_\alpha) + V(R_1, R_2, \alpha), \tag{1.2}$$

where T is the standard kinetic energy of a rotation-less triatomic molecule represented by

two inter-atomic distances R_1, R_2, and a bending angle α (with their canonically conjugate momenta P_1, P_2 and P_α). The potential V consists of Morse potentials V_i for each diatomic pair and an interaction potential V_I of the Sorbie-Murrell form [17], Chapter 7 and Eq. (7.3).

The dynamics, given by Hamiltonian of Eq. (1.2) of the collinear version of OCS (with $\alpha = \pi$, $P_\alpha = 0$) was first studied by Carter and Brumer [17]. They characterized the motion of this system at a number of energies, extending up to $20,000\,\mathrm{cm}^{-1}$ (which amounts to $E = 0.09$). After integrating trajectories for 2.4 ps, they arrived at a relaxation time (as defined in Refs. [105, 35, 57]) of 0.17 ps. However, they found that this system does not relax to statistical equilibrium after 2.4 ps. When this contradiction was investigated by integrating the equations for much longer times (45 ps), two distinct timescales for relaxation were found, the longer of which characterized energy redistribution that was incomplete even after 45 ps [28]. Sudden transitions between relatively long-lived regions of localized mode energies were observed all the way to the picosecond time scale.

Davis and Wagner continued to study collinear OCS [28]. This 2-dof model allows the use of Poincaré surfaces of section as a visualization tool for phase space structures. They revealed that even at the high energy of $20,000\ \mathrm{cm}^{-1}$ ($E = 0.09$), the system has a "divided phase space", with coexisting regular and chaotic regions. They observed that trajectories could be trapped in restricted regions of phase space for many vibrational periods, after which they would suddenly move to other regions of phase space to repeat the pattern.

Further progress came with the recognition that then-recent "lobe dynamics" [81, 8] could help explain non-statistical relaxation in 2-dof systems [26]. With increasing perturbation strength, the two dimensional invariant tori of a 2-dof Hamiltonian system develop sets of "holes," with the systematics of Cantor sets. These holes, dubbed "cantori" [81], form leaky barriers that can act as bottlenecks to the phase space transport. These bottlenecks are associated with broken tori with irrational frequency ratios, with those with "noble" number ratios being generically the very last to be destroyed by an increasing perturbation. These numbers are the most robust as they are the most poorly approximated by rationals [58]. For OCS, this has been confirmed [26] in a region between two resonances $\omega_{\mathrm{CO}}/\omega_{\mathrm{CS}} = 3/1$ and $\omega_{\mathrm{CO}}/\omega_{\mathrm{CS}} = 5/2$. The noblest irrational number between the rationals 5/2 and 3/1 is

$2+\gamma$, where $\gamma = (\sqrt{5}-1)/2 \approx 0.6180339887$ is the so-called golden mean [81, 58]. These results, obtained from classical mechanics, were confirmed using a quantal wave packet calculation [49]. These results could not be extended to the planar, 3-dof OCS due to severe technical and computational difficulties [50, 51]. However, there were indications that this problem of intra-molecular energy flow in higher dimensions is also related to the resonant and non–resonant structures [86].

1.3 Using methods of dynamical systems theory

The two physical problems, described in Sections 1.1 and 1.2, have in common that the Hamiltonians (Eq. (1.1) and Eq. (1.2)) generate both regular and chaotic trajectories, i.e. they are mixed systems from a dynamical systems point of view. These Hamiltonians define velocity vector, which in turn defines a flow φ on the phase space $\mathcal{M}$. These concepts are studied by the theory of dynamical systems, (also called the "qualitative theory of ordinary differential equations"). Hamiltonian flows constitute a special class of dynamical systems. These flows arise as a natural setting to study problems of physics, and their distinctive characteristic is the existence of conserved integrals, constraining dynamics to sub-manifolds of the $2D$ dimensional phase space $\mathcal{M}$. There is always at least one integral, called the Hamiltonian (or "energy") and the dynamics are constrained to a $2D-1$ dimensional "energy shell."

The prerequisite to application of the theory is a good control of invariants of the dynamical system under investigation: equilibrium points, periodic orbits, quasi-periodic manifolds. The theory brings is the methodology of how to compute expectation values of physical observables in chaotic systems by relating the spectrum of a certain *evolution* operator to dynamical invariants, such as equilibria and periodic orbits. Its predictive power and elegance rivals those of statistical physics and quantum field theory.

A basic feature of dynamical systems is the notion of asymptotic behavior of a (typical) solution. This leads to certain invariant sets and in particular to *attractors* of the dynamical system. Dynamical systems have two kinds of classical attractors which persist under small perturbations of the differential equations. These are the stable equilibria and the

stable nontrivial periodic solutions or oscillators For a physical example, consider states of a harmonic oscillator and the Kepler problem. The corresponding phase space is chockablock with invariants (all orbits are periodic). Classical physics approach is to assume that these states become attractive under perturbations, and one can use them as zeroth-order approximations to physical systems by accounting for weak nonlinearities using the perturbation theory (for example see Chapter 3).

A great new development was the discovery [78] and very general description of a *strange attractor* [108]. It is robust in the sense that its properties persist under perturbations of the differential equation (i.e., it is structurally stable [107, 12, 13, 98, 99, 87]. A good model, capturing the two essential ingredients of strange attractors, is the "Baker's Map" [121, Chapter 4]. Every point in the (two dimensional) phase space is everywhere locally unstable, i.e. has positive Lyapunov exponent. Therefore the map is often (informally) called *stretching*. The global constraints force the the stretched volume of the phase space to fold back, introducing *mixing* into the system. If a deterministic system is locally unstable (positive Lyapunov exponent) an globally mixing (positive entropy) it is said to be a *chaotic* dynamical system.

Already Poincaré was familiar with this vision of chaos, with unstable periodic orbits providing instability, and interweaving of their stable and unstable manifolds providing global mixing. In a chaotic system, any open ball of initial conditions no matter how small, will in finite time overlap with any other finite region and in this sense spread over the extent of the entire asymptotically accessible state space. The focus of the theory of such systems shifts to a description of the geometry of the space of possible outcomes, and evaluation of averages over this space.

In many of the real world systems that are considered chaotic, complexity comes about from their ability to comprise attractors of a very different nature in one state space. A good example of this situation is provided by the crossed-fields problem, studied in Chapter 4.

A typical "chaotic" system is bounded, and a scale L, measuring the size of the system, can be prescribed. Any two trajectories that start out very close to each other (with initial difference in coordinates $\delta\mathbf{x}(0)$, separate exponentially with time, and in finite (in practice, a short) time their separation $\delta\mathbf{x}(t)$ attains the magnitude of L, the size of the whole system.

This property of *sensitivity to initial conditions* can be quantified as

$$|\delta\mathbf{x}(t)| \sim \exp(\lambda t)|\delta\mathbf{x}(0)|.$$

The rate of separation is described in terms of the factor in the exponent, called the *Lyapunov exponent*. The practical consequence is that for any finite accuracy $\epsilon = |\delta\mathbf{x}(0)|$ of the initial data, the dynamics is practically unpredictable beyond the finite *Lyapunov time*,

$$T_{\rm Lyap} = \frac{1}{\lambda} \ln \frac{L}{\epsilon}\,.$$

The second necessary ingredient is the property of *mixing*, which can be described as the coming together again and again of trajectories. This is not unusual, especially when the phase space has boundaries. The trajectories necessarily fold back at the boundaries.

A closed invariant set A is called an attractor if all nearby solutions lead to A as $t \to \infty$. The Bowen-Ruelle theorem states that for an Axiom A system, except for an initial set of Lebesgue measure zero, time averages exist for continuous phase functions. More precisely, except for this initial set, a solution $t \mapsto \varphi^t$ tends to some attractor A. The attractor A has a canonical invariant ergodic measure μ and if f is continuous function on the phase space, then

$$\lim_{T\to\infty} \int_0^T \frac{1}{T} f(\varphi^t) dt = \int_A f d\mu\,. \tag{1.3}$$

The invariant measures in chaotic systems are unusually complex, non-differentiable, and in all imaginable ways unpleasant to deal with functions of the phase space. In fact, hidden in the complexity of chaotic attractors there is a rigid skeleton, an invariant set, called the "repeller" with the structure of a Cantor set, and with periodic orbits as its elements. The periodic orbit theory [23] has the advantage that one does not need to compute the invariant measure explicitly. It expresses the density evolution in terms of a linear operator $\mathcal{L}^t$:

$$\rho(x) \xrightarrow{\mathcal{L}^t} \int_{\mathcal{M}} \delta(x - \varphi^t(y))\rho(y)\,, \tag{1.4}$$

and reformulates the problem of finding the spectrum of $\mathcal{L}^t$ in terms of finding zeros of the dynamical *Zeta* function $\zeta(s)$,

$$\zeta(s) = \prod_{p_i \in \text{unstable cycles}} \left(1 - \frac{\exp(\iota s A)}{\Lambda_{p_i}}\right). \tag{1.5}$$

expressed as an infinite product. Each unstable periodic orbit ("cycle") contributes a term in this product, where A is a value of an observable computed on the orbit, and Λ_{p_i} is the Lyapunov multiplier of the orbit [23].

The main instrument of computing averages is the *trace formula*, a weighted sum over such periodic orbits. There are methods to accelerate the convergence of the sum, but that requires knowledge the orbital order, that is of the symbolic dynamics.

The critique of dynamical systems approach is the "overhead", caused by a need of sophisticated numerical calculations. It requires solid skills, developed by years of practice, in locating particular solutions of nonlinear equations in high dimensional spaces.

On the other hand, statistical methods, quite often produce reasonable results requiring only rather pedestrian numerical simulations. In statistical physics, it is inevitable to make assumptions about the asymptotic behavior of the system, the first and most famous example being the Boltzmann ansatz.

The dynamical systems approach deals with problems in a definitive way: the invariants are genuine objects of a dynamical system, and description of mechanisms of transitions or spectra in terms of these objects provide a faithful, no-assumption description of physical phenomena.

1.4 Outline of the thesis

Throughout the work we explore several concepts, which can be summarized as follows:

Periodic orbits can be interpreted as nonlinear modes of dynamics.

Unstable invariant structures (saddles, periodic, quasi-periodic orbits) play a major role in trapping of trajectories and as bottlenecks of transitions.

Stable and unstable manifolds and their intersections can be used to partition the phase space for symbolic dynamics.

In Chapter 2 and Chapter 5 we present concepts of the dynamical systems theory and develop general methods that use these concepts to solve physical problems studied in this work. In particular, Chapter 2 is devoted to presenting our methods of projection from

continuous time flows to the mapping of the surface of section and their applications to periodic orbit searches. Then, in Chapter 5, we apply our methodology to searching for 2-dimensional invariant tori.

Chapter 3 presents our introductory study of various limiting cases of the crossed-fields problem. We focus on the strong magnetic field and perturbative limits. We end this chapter with the study of the onset of chaos using the Melnikov analysis.

In Chapter 4, we present our work on the symbolic dynamics of crossed-fields problem in 2-dof in the regime of strong chaos.

Chapters 6 and 7 are devoted to study of 3-dof chaotic Hamiltonian systems, and to the role of 2-dimensional invariant tori in processes of trapping (see Chapter 7) and symbolic dynamics (see Chapter 6). In Chapter 6 we use methods, developed in Chapter 5, and high order normal forms to compute a high dimensional saddle of the crossed-fields problem in 3-dof setting. In Chapter 7 we present a detailed study of trapping in the carbonyl sulfide (OCS) molecule.

CHAPTER II

SOME ASPECTS OF DYNAMICAL SYSTEMS' THEORY

In problems of chaotic molecular or atomic dynamics, a natural approach is to use the methods of dynamical systems theory. In this chapter we summarize some basic concepts of the theory. We also discuss practical issues such as reduction to the surface of section and finding complicated periodic orbits on constant energy shell, used in Chapter 4. These ideas will be extended to computations of quasi-periodic invariant structures in Chapter 5

2.1 Fundamental concepts

A dynamical systems is usually defined by a pair $(\mathcal{M}, \varphi^t)$. These constituent symbols stand for:

A "phase space" $\mathcal{M}$, whose elements or "points" represent possible states of the system. Phase space may be compact or open.

"Time" t, which may be discrete or continuous and extend only into the future or into the future as well as the past.

The time evolution law φ. It is the rule that allows us to determine the state of the system at each moment of time t from its state at any particular moment. Thus if our system was initially at a state $x \in \mathcal{M}$, it will find itself after time t at a new state, which is uniquely determined by x and t, and thus can be denoted by $F(x,t)$. Fixing t, we obtain a flow φ, a transformation $\varphi^t(x) : x \mapsto F(x,t)$ of the phase space into itself. These transformations for different t are related to each other. Namely, they are said to satisfy (semi-)group (composition) property $\varphi^t \circ \varphi^{t'} = \varphi^{t+t'}$ and may or may not be defined for all x and t.

2.1.1 Continuous time flows

A continuous time dynamical system is usually given infinitesimally (for example, by means of differential equations) and the reconstruction of the dynamics from this infinitesimal description involves integration of a system of ordinary differential equations. We assume that the phase space $\mathcal{M}$ is a smooth manifold of dimension m and thus the time evolution is given by a smooth function $F(x,t) = \varphi^t(x)$, $x \in \mathcal{M}$, $t \in \mathbb{R}$. When we fix $x \in \mathcal{M}$, and vary t we obtain a parameterized smooth curve on $\mathcal{M}$. Let $\xi(x)$ be the tangent vector to this curve at $t = 0$, that is, at the point x. Properly speaking, the vector $\xi(x)$ belongs to the tangent space $T_x\mathcal{M}$, which is an m-dimensional linear space "attached" to $\mathcal{M}$ at the point x. The map $x \mapsto \xi(x)$ forms a *vector field* on $\mathcal{M}$. Consider the *tangent bundle* $T\mathcal{M} = \bigcup_{x\in\mathcal{M}} T_x\mathcal{M}$. Let $U \subset \mathcal{M}$ be a coordinate neighborhood with coordinates $(s_1, \ldots, s_m)$. Then the tangent bundle TU is simply a direct product $U \times \mathbb{R}^m$ and a vector field is determined by a map from U to $\mathbb{R}^m$, that is by m real-valued functions $v_1, \ldots, v_m$, as follows. Denoting $\frac{\partial}{\partial s_i}$ the basic vector fields which associate to every point the ith vector of the standard basis in $\mathbb{R}^m$ we can represent every vector field locally as $\sum_{i=1}^m v_i(s_1, \ldots, s_m)\frac{\partial}{\partial s_i}$. If our initial point x is represented by coordinates $s_i^0, \ldots, s_m^0$ then the evolution of this point is obtained by solving the system of first-order ordinary differential equations

$$\frac{ds_i}{dt} = v_i(s_1, \ldots, s_m) \tag{2.1}$$

with initial conditions $s_i(0) = s_i^0$ for $i = 1, \ldots, m$. Thus, at least for small t, the transformation φ^t can be recovered from the vector field. For larger t one should take compositions of maps defined in local coordinates. For all t we can write a formal expression

$$F(x,t) = \int_0^t v(F(x,t'))\, dt'. \tag{2.2}$$

2.2 Phase space and the surface of section

There are useful relations between continuous-time and discrete-time dynamical systems. Usually it is possible to associate a map to any flow, but the opposite of this statement in general is not true [69, Chapter 0.3].

A local, but very useful method is the construction of a *Poincaré (first-return) map*. Let us take a point $x \in \mathcal{M}$ such that $\xi(x) \neq 0$ and an $m-1$ dimensional (co-dimension-one) sub-manifold $\mathcal{S}$ containing x and transverse to the vector field. The latter property simply means that for every point $y \in \mathcal{S}$ the vector $\xi(x)$ is not tangent to $\mathcal{S}$. If we assume that the point x is periodic for the flow, that is, $\varphi^{t_0}(x) = x$ for some $t_0 > 0$, then every nearby orbit of the flow intersects the surface $\mathcal{S}$ at a time close to t_0 so we have defined for a neighborhood U of x on $\mathcal{S}$ a map $\mathcal{P}_{\mathcal{S}} : U \to \mathcal{S}$ such that $\mathcal{P}_{\mathcal{S}}(x) = x$. This map is called a *section map* or *first-return map* or *Poincaré map* for the flow. The manifold $\mathcal{S}$ is called the *surface of section*. Let φ^t be a (semi-) flow on the manifold $\mathcal{M}$, and a periodic point p of period $T(p) > 0$. We assume that $(x,t) \mapsto \varphi^t x$ is continuous, and that in a neighborhood of $(p, T(p))$, the map $(x,t) \mapsto \varphi^t x$ has at least one continuous derivative. Let $\mathcal{S}$ be a sub-manifold of co-dimension 1 transversal at p to the orbit of p. For x near p in $\mathcal{M}$, there is a unique $\tau(x)$ near $T(p)$ in $\mathbb{R}$ such that $\varphi^{\tau(x)} x \in \mathcal{S}$. The function τ has as many derivatives as the map, and the first return map $\mathcal{P} : x \mapsto \varphi^{\tau(x)} x$ from a neighborhood of p in $\mathcal{S}$ to $\mathcal{S}$. Explicit construction of the derivative on the Poincaré section is illustrated in Figure 2.5.2.

Going in the opposite direction, we can consider diffeomorphism $f : \mathcal{S} \mapsto \mathcal{S}$ and construct a *suspension flow* on the *suspension manifold* $\mathcal{S}_f$ which is obtained from the direct product $\mathcal{S} \times [0,1]$ by identifying pairs of points of the form $(x,1)$ and $(f(x),0)$ for $x \in \mathcal{S}$. The suspension flow ${\sigma^t}_f$ is determined by the "vertical" vector field $\frac{\partial}{\partial t}$ on $\mathcal{S}_f$.

The surface of section is the main concept in the *"Method of the surface of section"* (see Section 2.5). In the studies of geometric properties of continuous time flows it is useful to reduce the flows in the phase space to the map of the surface of section, usually defined by an equation

$$\mathcal{S} : \Sigma(x) = 0 \quad x \in \mathcal{M}\,, \tag{2.3}$$

and study the associated discrete-time system $\mathcal{F}_{\mathcal{S}} : \mathcal{S} \mapsto \mathcal{S}$.

Contrary to the *locally defined* Poincaré map, global surfaces of section are typically non-transversal.

2.3 Linearization and Jacobian

Constructs of linearization plays a central role in the theory of smooth dynamical systems. If $U \subset \mathbb{R}^m$ is an open neighborhood of x_0 and $\mathcal{F}_\mathcal{S} : U \to \mathbb{R}^m$ is a differentiable map, we can represent $\mathcal{F}_\mathcal{S}$ near the point x_0 as the constant part $\mathcal{F}_\mathcal{S}(x_0)$ plus the linear part $D\mathcal{F}_\mathcal{S}(x_0)(x - x_0)$ plus higher order terms. The differential $D\mathcal{F}_\mathcal{S}$ is a linear operator in $\mathbb{R}^m$ that is represented in coordinate form by the matrix of partial derivatives. if $\mathcal{F}_\mathcal{S}(t_1, \ldots, t_m) = ((\mathcal{F}_\mathcal{S})_1(t_1, \ldots, t_m), \ldots, (\mathcal{F}_\mathcal{S})_m(t_1, \ldots, t_m))$, then

$$D\mathcal{F}_\mathcal{S}(x_0)(t_1, \ldots, t_m) = \left(\frac{\partial(\mathcal{F}_\mathcal{S})_i}{\partial t_j}\right)_{i,j=1,\ldots,m}, \tag{2.4}$$

where the partial derivatives are calculated at the values of the coordinates corresponding to the point x_0. The picture remains essentially the same for differentiable maps of smooth manifolds with the only difference that instead of the standard coordinate system in $\mathbb{R}^m$ one should use appropriate local coordinate systems near a point and its image. A more invariant way to express the same idea is to describe the differential $D\mathcal{F}_\mathcal{S}(x_0)$ of the map $\mathcal{F}_\mathcal{S} : \mathcal{S} \to \mathcal{S}$ as a linear map of the tangent space $T_{x_0}\mathcal{M}$ into the space $T_{\mathcal{F}_\mathcal{S}(x_0)}\mathcal{M}$ if $\mathcal{F}_\mathcal{S}$ is a diffeomorphism the differential is invertible. This construction can be globalized by considering the tangent bundle $T\mathcal{M} = \bigcup_{x\in\mathcal{M}} T_x\mathcal{M}$ which can be provided with the structure of a differentiable manifold whose dimension is twice the dimension of $T\mathcal{M}$. Any local coordinate system on $\mathcal{M}$ induces a coordinate system in $T\mathcal{M}$ which is global in the tangent direction. Namely, tangent vectors to the coordinate curves form a basis in each tangent space and the $2n$ coordinates of a tangent vector include n coordinates of its base point plus the coordinates of the vector with respect to that basis.

When we consider iterates of a map $\mathcal{F}_\mathcal{S}$ (Eq. (2.5)), the differential $D\mathcal{F}_\mathcal{S}{}^n(x) : T_x\mathcal{M} \to T_{\mathcal{F}_\mathcal{S}{}^n(x)}\mathcal{M}$ of the nth iterate is a composition of the differentials $Df_{\mathcal{F}_\mathcal{S}{}^i(x)} : T\mathcal{M} \xrightarrow{\mathcal{F}_\mathcal{S}{}^i(x)} T_{\mathcal{F}_\mathcal{S}{}^{i+1}(x)}\mathcal{M}$, $i = 0, \ldots, n-1$:

$$x_1 \xrightarrow{\mathcal{F}_\mathcal{S}(x_1)} x_2 \xrightarrow{\mathcal{F}_\mathcal{S}(x_2)} x_3 \ldots \xrightarrow{\mathcal{F}_\mathcal{S} x_{i-1}} x_i \tag{2.5}$$

$$T_{x_1}\mathcal{S} \xrightarrow{D\mathcal{F}_\mathcal{S}(x_1)} T_{x_2}\mathcal{S} \xrightarrow{D\mathcal{F}_\mathcal{S}(x_2)} T_{x_3}\mathcal{S} \ldots \xrightarrow{D\mathcal{F}_\mathcal{S}{}^{i-1}(x)} T_{\mathcal{F}_\mathcal{S}{}^i(x)}\mathcal{S} \tag{2.6}$$

The situation for flows is similar. Given that the law of evolution is determined by a

system of ordinary differential equations

$$\frac{dx}{dt} = v(x) \tag{2.7}$$

The derivative is called the Jacobian $J(x,t) = \frac{\partial F(x,t)}{\partial x}$. The time evolution of the Jacobian is

$$\frac{dJ(x,t)}{dt} = \frac{\partial v(x)}{\partial x} J(x,t) \tag{2.8}$$

The formal solution for all t can be derived from Eq. (2.2) by differentiation of F:

$$J(x,t) = \int_0^t \frac{\partial v(x)}{\partial x}(F(x,t'))J(x,t')dt \tag{2.9}$$

The initial conditions are

$$J(x,0) = \mathbf{1}\,. \tag{2.10}$$

The Eq. (2.9) and Eq. (2.10) are usually integrated numerically together with the evolution law, given by Eq. (2.7).

In this localized picture the asymptotic properties of $\mathcal{F}_{\mathcal{S}}$ correspond to the properties of products of linear maps thus obtained, when the number of factors goes to infinity. Once the behavior of such products is understood, the question arises as to what extent this behavior reflects the properties of the original nonlinear system. The crucial point here is that the differential at any given point approximates well the behavior of points near the point at which the differential has been calculated. The quality of this approximation depends on the nonlinear terms, for example, on the size of second derivatives grows (by the chain rule), so, a priori, the quality of the linear approximation should deteriorate. Under certain conditions the influence of nonlinear terms can be controlled, so that we obtain a picture of the behavior of those orbits that stay near the original orbit for sufficiently long time. Considerations of this kind represent the content of what is usually called the local analysis of smooth dynamical systems.

An ideal setting for the local approach appears when the original orbit is periodic, say, ${\mathcal{F}_{\mathcal{S}}}^n(x_0) = x_0$. Then the sequence of differentials is also periodic and the main role in the local analysis is played by the iterates of a single linear operator $D{\mathcal{F}_{\mathcal{S}}}^n(x_0)$, which represents the infinitesimal behavior of nearby orbits for the period. In particular, the eigenvalues of

that operator play a crucial role in the local analysis near a point x_0. For continuous-time dynamical systems the role of the differential is played by the variational equation (Eq. (2.9)) whose right-hand side represents the infinitesimal generator for the one-parameter group of differentials of the maps forming the flow.

Though the local analysis concerns itself with the relative behavior of nearby orbits of, in the case of a neighborhood of a periodic orbit, with the behavior if orbits or orbit segments as long as they stay near the periodic orbit, the main goal of the theory of smooth dynamical systems is to understand the global behavior of nonlinear maps. Sometimes local analysis plays a crucial role in the global consideration. This happens, for example, if a periodic point represents an attractor, that is, if neighboring orbits approach it asymptotically with time. More generally, we may try to localize certain parts of the phase space that play a particularly important role for the asymptotic behavior and to study the orbits inside and nearby this part. It is also possible that the behavior of orbits with certain initial conditions is particularly important due to the nature of a particular physical problem which is represented by the dynamical system.

2.4 Hamiltonian systems

Hamiltonian systems, or Hamiltonian flows constitute a special class of dynamical systems. Their characteristic feature is existence of conserved quantities. Each conserved quantity corresponds to an integral, a function of phase space variables, that is left unchanged by the flow. Any Hamiltonian flow has at least one such function, the Hamiltonian H, corresponding to the energy of the system E. It is customary to express the relation by $H(x) = E$, but for our purposes it is more useful to use the notation $H(x) - E \to H(x; E)$. The energy shell the is defined as a sub-manifold of $\mathcal{M}$, such that

$$H(x; E) = 0 \tag{2.11}$$

The derivative of the energy is defined as $DH(x; E)$. It is a $2D$ dimensional vector with components

$$(DH(x; E))_i = \frac{\partial H(x; E)}{\partial x_i} \tag{2.12}$$

2.5 Some techniques used in the method of surface of section

In most applications the reduction to the surface of section is achieved by parameterizing the phase space $\mathcal{M}$ in such a way, that one of the level surfaces of one of the parameters coincides with the surface of section. Without loss of generality we can set the level surface at zero. The parameters can be taken as new coordinates, with the exception of one parameter, corresponding to the surface. Furthermore the derivative of the surface (mapping of tangent space of the surface to the tangent space of the same surface) will be constructed. In Hamiltonian flows, additional reduction can be achieved by eliminating one more parameter.

2.5.1 Projection $\mathcal{M} \to \mathcal{S}$

The reduction of dimension using one or more equations of constraints, such as the energy condition Eq. (2.11), or the surface of section condition Eq. (2.3), is a very common procedure to eliminate a set of chosen coordinates, thus reducing the dimensionality of the phase space. This method is called projection. The reverse procedure (restoring the full set of the original coordinates) involves solving the equations of constraints.

Without loss of generality we can assume that a transformation $T : \mathcal{M} \mapsto \mathcal{M}$ is given, not necessarily linear in x, and that $y = T(x)$ defines new parameterization of the phase space $y = (y_0, \ldots, y_{n-1})$. Suppose that Eq. (2.3) is equivalent to setting $y_0 = 0$, i.e. that $T(x) = (\Sigma(x), y_1(x), \ldots, y_{n-1}(x))$.

Given a Hamiltonian system, one additional coordinate can be eliminated. We can assume, that the surface of section $\mathcal{S}$ is parameterized by $z = (y_2, \ldots, y_{n-1})$. Supposing a point z on the surface $\mathcal{S}$ is given, and that we *know* a value of y_1 that is "close" to the surface. Then coordinate in the phase space $\mathcal{M}$ can be found by solving the energy equation $H(x(y); E) = 0$ for $y_1 = y_1(z; E)$.

One method to find such solution, once an approximate solution is given, is the Newton's method. Assuming, that such x_0 is given, that $T(x_0) = (0, y_1 + \varepsilon, z_0)$, corresponding to point z_0 on the $\mathcal{S}$, we obtain a one-dimensional linear iteration

$$H(x_0; E) + \left[DH(x_0; E)DT^{-1}(x_0)\right]_1 \varepsilon = 0 \tag{2.13}$$

Supposing the iterations converge, we achieve the following two goals: a) the coordinate on the surface z is preserved and b) the Hamiltonian condition $H(x;E)=0$ is satisfied.

The above method is useful when it is imperative to preserve the surface of section coordinate. If this condition can be relaxed, and is is required to find a solution on the surface of section, close to a given initial condition x_0. In this case there is available a large pool of options one can choose from. Two examples follow, two- and one- step solution.

There are two points to have in mind. The equation $\Sigma(x)=0$ has to be satisfied, and equation $H(x,E)$ has to be satisfied. In general these equations are both nonlinear and we look for a solution using Newton's iterations, assuming that such an initial condition can be found, which will guarantee convergence of the iterations.

Our approach is to construct a suitable *cost function*, whose (local or global) minimum corresponds to our solution. Then, provided there is a good initial condition, the solution is found by iterations using Newton iteration scheme. In general, suppose the cost functional is $\mathcal{I}(x)\geq 0$ is given such that $\mathcal{I}(x_0)=0$. To find the solution x_0 we start with an initial guess x, and iterate

$$x \to x-(D\mathcal{I}(x))^{-1}\mathcal{I}(x)$$

In this context we will always use the "distance" between two points as a cost,

$$\mathcal{I}_0(x,x')=d(x',x)^2/2$$

motivated by the attempt to find the solution which is the "closest" to an initial guess. The precise definition of norm – or distance – can be adapted to the problem. We have used Euclidean norm $d(x,x')=\sqrt{\sum_i (x_i-x_i')^2}$, but other norms can be used as well[1]

In general we have two constraints, $H(x,E)=0$ and $\Sigma(x)=0$, therefore the constrained variations read

$$\mathcal{I}_{\mathcal{S}_E}(\delta,\lambda,\mu)=\frac{\delta^2}{2}+\lambda H(x+\delta,E)+\mu\Sigma(x+\delta) \tag{2.14}$$

[1] A weighted Euclidean norm $d_a(x,x')=\sqrt{\sum_i [a_i(x_i-x_i')]^2}$ is useful in the OCS Hamiltonian (see Eq. (7.1)), where typical trajectories in (R_1, R_2, α) oscillate on small "1" scale in R_i, while the corresponding momenta oscillate on a "10^2" scale. Scaling "large" variables down may lead to improved stability of computations.

The variation $\delta\mathcal{I}_{\mathcal{S}}$ and derivative $D\mathcal{I}_{\mathcal{S}}$ reads

$$\delta\mathcal{I}_{\mathcal{S}_E} = \begin{cases} \delta + \lambda DH(x_0) + \mu D\Sigma(x_0) \\ DH(x_0)\delta + H(x_0, E) \\ D\Psi(x_0)\delta + \mathcal{S}(x_0, E) \end{cases} \qquad D\mathcal{I}_{\mathcal{S}_E} = \begin{pmatrix} \mathbf{1} & DH(x) & \Sigma(x) \\ DH(x) & \Sigma(x) & 0 \end{pmatrix} \tag{2.15}$$

If the equation $\Sigma(x) = 0$ is linear in x, the above method can be simplified. The problem can be solved in two steps. First, a coordinate on the energy shell is found. Second, Eq. (2.13) is solved to put the coordinate on $\mathcal{S}$. For the first step the cost function is

$$\mathcal{I}_E(\delta, \mu) = \frac{\delta^2}{2} + \lambda H(x + \delta, E) \tag{2.16}$$

and variation and derivative read as

$$\delta\mathcal{I}_E = \begin{cases} \delta + \lambda DH(x_0) \\ DH(x_0)\delta + H(x_0, E) \end{cases} \qquad D\mathcal{I}_E = \begin{pmatrix} \mathbf{1} & DH(x) \\ DH(x) & 0 \end{pmatrix}. \tag{2.17}$$

Curiously, for the matrix in Eq. (2.17), we can provide eigenvalues explicitly.

$$\mathcal{P}(\lambda) = |D(x_0, E) - \lambda\mathbf{1}| = \left| \begin{pmatrix} 1 - \lambda\mathbf{1} & DH(x_0) \\ DH(x_0) & \lambda \end{pmatrix} \right| \tag{2.18}$$

along the last row (column), from right to left: the first term is $(-1)^{2m}\lambda(1-\lambda)^m$; the second term is $DH(x_0)_m$ times the remaining determinant, which then is expanded by the row, which contains only zeros except for one (possibly) nonzero entry of $DH(x_0)_m$, obtaining $-(-1)^{2m}DH(x_0)^2(-1)^{2(m-1)}(1-\lambda)^{m-1}$. The remaining terms are obtained in a similar fashion. The result is

$$\mathcal{P}(\lambda) = (1-\lambda)^{m-1}\left(\lambda(1-\lambda) - |DH(x_0)|^2\right) \tag{2.19}$$

In particular, the coefficient of λ^0 is the determinant $|D(x_0, E)| = -|DH(x_0)|^2$, which can be read off the Eq. (2.19).

2.5.2 Projection $T\mathcal{M} \to T\mathcal{S}$, general and symplectic case.

In the preceding section we have described several techniques of how to manipulate projection operators to obtain different coordinate representations of a point in the phase space.

Commonly it is also necessary to control the projections of infinitesimal displacements from a given point in the phase space. It is necessary to know what controls projections of tangent spaces $T\mathcal{M} \to T\mathcal{S}$. This projection involves reduction of matrices, from $n \times n$ in the original phase space $T\mathcal{M} \sim \mathbb{R}^n$ to $(n-1) \times (n-1)$ in the reduced phase space $T\mathcal{S} \sim \mathbb{R}^{n-1}$. How to project the Jacobian J of the flow to the surface of section in the absence of any symmetries is pictorially explained in Figure 2.5.2. Because of symplectic symmetry, inherent to

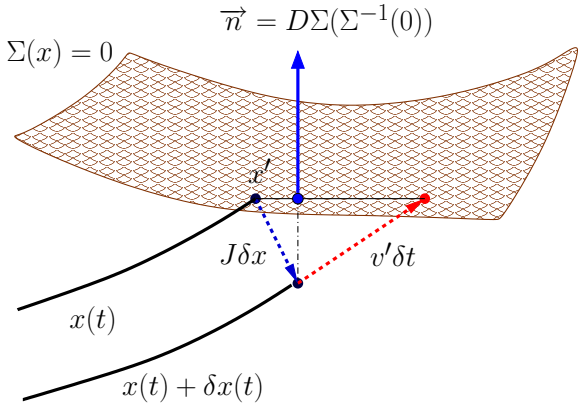


Figure 2.1: Reduction of the Jacobian $J(x, \tau)$ to derivative of the map $D\mathcal{F}_\mathcal{S}(x)$. If $x(t)$ intersects the Poincaré section at $x' \in \mathcal{S}$ at time τ, the nearby $x(t) + \delta x(t)$ trajectory intersects it time $\tau + \delta t$ later. As $(\overrightarrow{n} \cdot v' \delta t) = -(\overrightarrow{n} \cdot J\, \delta x)$, the difference in arrival times is given by $\delta t = -(\overrightarrow{n} \cdot J\, \delta x)/(\overrightarrow{n} \cdot v')$, and the projection of the Jacobian to the surface of section is $D\mathcal{F}_\mathcal{S}(x_0) \simeq \tilde{J}_{ij} = J_{ij} - v'_i(\overrightarrow{n} \cdot J)_j/(\overrightarrow{n} \cdot v')$.

Hamiltonian systems, marginal eigenvalues always come in pairs. In many cases energy is the only conserved quantity. Then we can reduce the phase space by restricting the flow on the energy shell and to $\mathcal{S}_E \sim \mathbb{R}^{n-2}$.

The derivative maps tangent spaces, $D\mathcal{F}_\mathcal{S} : TM_x \mapsto TM_{F(x,t)}$, and if the flow is generated by a Hamiltonian, it additionally satisfies symplectic symmetry requirement $\Omega(D\mathcal{F}_\mathcal{S}(x)\xi, D\mathcal{F}_\mathcal{S}(x)\xi') = \Omega(\xi, \xi')$. In coordinates we obtain the relation

$$\mathbf{J}\mathbb{I}^\top\mathbf{J} = \mathbb{I} \tag{2.20}$$

More generally, if (X, Ω) and (Y, Ξ) are symplectic vector spaces, a smooth map $f : X \mapsto Y$ is called symplectic (canonical) if it preserves the symplectic (canonical) forms, that is, if

$$\Xi(\mathbf{D}f(z) \cdot z_1, \mathbf{D}f(z) \cdot z_2) = \Omega(z_1, z_2)$$

We will exploit this definition define the surface of section manifold and to endow its tangent space with the symplectic structure. The projection operator $\Pi : V \mapsto W$, $\Pi(v,w)$, $v \in V$, $w \in V^*$

$$\Pi(u,v)x = x - \langle v,x\rangle u/\langle v,u\rangle \tag{2.21}$$

or in matrix form it is

$$(\mathbf{P}(u,v))_{ij} = \mathbf{1}_{ij} - \frac{u_i v_j}{\langle v,u\rangle} \tag{2.22}$$

We construct the derivative matrix of the induces first-return map. The normal vector to the co-dimension-one surface of section is $n(x)$, $x \in \mathcal{S}$. The surface of section maps $x' = \mathcal{F}_{\mathcal{S}}(x)$. We denote derivative of the Hamiltonian as a vector by $h(x) = \mathbf{d}H(x)$, and $h = h(x)$, $h' = h(x')$, and similarly $v = v(x)$, $v' = v(x')$. We also denote $\tilde{n}(x) = \mathbb{I}n(x)$. We construct the Jacobian as

$$\tilde{\mathbf{J}} = \mathbf{P}(v(x'),n(x'))\mathbf{J}\mathbf{P}(\mathbb{I}n(x),\mathbb{I}v(x)) \tag{2.23}$$

In practice, one constructs a local coordinate chart at each point on the $\mathcal{S}$ such that for example at least locally $\mathcal{S}$ is defined by $x_m = 0$. In that case the normal $n(x)_i = \delta_{im}$, and the $(\mathbb{I}n(x))_i = \delta_{i\sigma(m)}$, where $\sigma(m)$ is the index of the canonically conjugate variable to x_m.

$$\begin{aligned}\tilde{\mathbf{J}}_{ij} = \quad & \mathbf{J}_{ij} - v(x')_i\mathbf{J}_{mj}/v(x')_m - \mathbf{J}_{i\sigma(m)}h(x)_j/h(x)_{\sigma(m)} \\ & + v(x')_i\mathbf{J}_{m\sigma(m)}h(x)_j/(v(x')_m h(x)_{\sigma(m)})\end{aligned} \tag{2.24}$$

One needs to take the square sub-matrix with rows and columns corresponding to indices m and $\sigma(m)$ excluded. The resulting matrix has a symplectic structure.

2.5.3 Non-transversal surfaces of section

In practice, now matter how hard we try to invent a suitable global surface of section $\mathcal{S}$, the phase space topology will not cooperate. Globally defined surfaces $\mathcal{S}$ will satisfy the condition of non-transversality, defined by Eq. (2.25), somewhere. The Poicaré surface of section is transversal only locally. Non-transversality may be invisible when applications call for only a small number of periodic orbits. Whenever a large number of orbits is required, the "defects" in $\mathcal{S}$ become a significant nuisance.

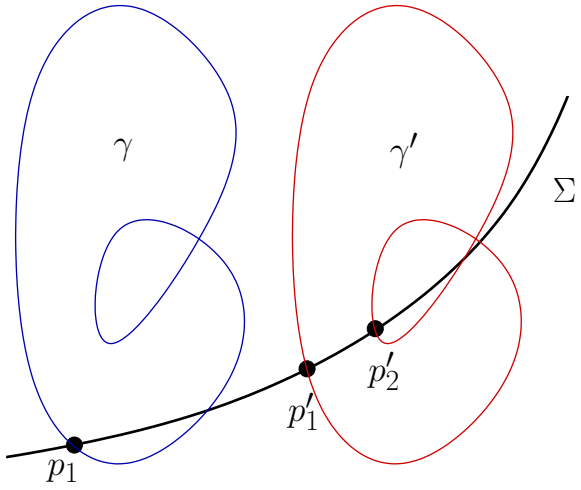


Figure 2.2: Counting problem, caused by nontransversal intersections. Two loops γ and γ' are identical, but have different number of intersections with the surface of section $\mathcal{S}$.

$$\begin{cases} \Sigma(x) = 0 \\ H(x, E) = 0 \\ D\Sigma(x) \cdot v(x) = 0 \end{cases} \tag{2.25}$$

Points where $v(x)$ is parallel to $\Sigma(x)$ are called tangential points. They are obtained by solving Eq. (2.25). If this equation does not have a solution, the surface $\Sigma(x)$ is globally transversal to the flow. Whenever $\dim \mathcal{S} > 3$, there are more independent variables than there are equations and Eq. (2.25) may be expected to have a family of solutions.

Existence solutions to Eq. (2.25) results in discontinuous maps $\mathcal{F}_\mathcal{S}$. This causes problem predicting the number of intersections with $\mathcal{S}$ of a particular periodic orbit, bearing severe consequences to the symbolic dynamics. This issue is illustrated in Figure 2.5.3

2.6 Methodology of computing periodic orbits

Successful implementation statistical approach to chaotic dynamical systems relies heavily on the competency to compute periodic orbits.

Here we briefly summarize our method of computing periodic as fixed points on the surface of section. This methods refines multiple shooting algorithm, by combining it with the local stable and unstable manifold information and symbolic dynamics. This method is

suitable for searches of short and extremely long and complex orbits.

Fastest algorithms of periodic orbit searches utilize the *Jacobian* of the orbit defined by Eq. (2.9). Whenever this matrix is evaluated at any point on the periodic orbit, one of it's eigenvalues, related to indifference with respect to translation along the orbit, is equal to one. Existence of such "marginal" eigenvalues is a cause of nuisance when applying numerical methods.

The computational overhead, required for reducing the flow to a map of $\mathcal{S} \mapsto \mathcal{S}$ and to Eq. (2.4) pays off here, because we have reduced the dimension of the map and explicitly eliminated (two in Hamiltonian case) marginal eigenvalues. We can proceed with calculations as if crossed-fields problem was defined in terms of a symplectic map.

2.6.1 Newton's method and shooting algorithm

A primitive cycle of $\mathcal{F}_\mathcal{S}$ is a point x, such that

$$x \xrightarrow{\mathcal{F}_\mathcal{S}} x$$

Newton's method is based on the linearization of the map $\mathcal{F}_\mathcal{S}(x) = x$, assuming x_0 is given "close to x", $x \approx \mathcal{F}_\mathcal{S}(x_0) + D\mathcal{F}_\mathcal{S}(x_0)(x - x_0)$. This expression has the solution implicitly; the explicit solution is obtained by converting this linearization into an iterative scheme:

$$x \mapsto x - (D\mathcal{F}_\mathcal{S})^{-1}(\mathcal{F}_\mathcal{S}(x) - x) \tag{2.26}$$

The longer cycles consist of a cyclic sequence of points on the surface, $\{x_i\}_{0 \le i < N}$ such that

$$x_0 \xrightarrow{\mathcal{F}_\mathcal{S}} x_1 \quad x_1 \xrightarrow{\mathcal{F}_\mathcal{S}} x_2 \quad \dots \quad x_{N-1} \xrightarrow{\mathcal{F}_\mathcal{S}} x_0 \tag{2.27}$$

The shooting algorithm consists in applying the Newton's method to an equation $F(x_0, \dots, x_{N-1}) = 0$, obtained by combining the entire itinerary and taking all intersection points as a set of independent variables $x = (x_0, \dots, x_{N-1})$:

$$F(x_0, \dots, x_{N-1}) = (\mathcal{F}_\mathcal{S}(x_0) - x_1, \mathcal{F}_\mathcal{S}(x_1) - x_2, \dots, \mathcal{F}_\mathcal{S}(x_{N-1}) - x_0) \tag{2.28}$$

The matrix of partial derivatives $DF(x)$ has a block-cyclic form

$$DF(x) = \begin{pmatrix} D\mathcal{F}_{\mathcal{S}}(x_0) & -1 & & \\ & D\mathcal{F}_{\mathcal{S}}(x_1) & -1 & \\ & & \cdots & \\ -1 & & & D\mathcal{F}_{\mathcal{S}}(x_{n-1}) \end{pmatrix} . \tag{2.29}$$

By experimentation we have arrived at the conclusion that the topology of the phase spaces and domains of convergence of Newton method are similar. In order to compute the correct periodic orbits, it is necessary to be able to set initial guess within the boundaries of symbolic partition. To provide such information it is necessary to know a priori approximate location of orbits. The way out of this vicious circle is provided by synthetic longer orbits from stable and unstable manifolds of shorter orbits.

2.7 Zero modes: the Maupertuis principle

The problem of elimination of marginal eigenvalues from the derivative matrix and corresponding reduction from the phase space to tangent space transverse to the orbit is tightly related to other problems in physics, such as "zero modes" in the field theory [89] and in mechanics. We present an example of reduction in mechanics: the variational principle to determine the shape of a trajectory of a mechanical system (the Maupertuis principle) and the resulting equations, in which dimension has been reduced by one, eliminating the tangential directions.

The cost function for a conservative mechanical system with Lagrangian $L = v^2/2 + A(x)v - V(x)$ is $I = \int_\gamma |v| dl + \int_\gamma A(x) dx$, where $dl = \sqrt{dx^2}$. The variational principle asserts that I is stationary on a solution of Lagrange equations of motion (AKA "true paths").

The first variation is $\delta I = \int_\gamma \left[\frac{\partial |v|}{\partial x} - \frac{d}{dl} \left(|v| \hat{\boldsymbol{\tau}} \right) \right] \delta x dl + \int_\gamma (\delta A dx - dA \delta x)$, which yields

$$\frac{\partial |v|}{\partial x} - \frac{d}{dl} \left(\hat{\boldsymbol{\tau}} |v| \right) + F \hat{\boldsymbol{\tau}} = 0 . \tag{2.30}$$

The equation (2.30) is used to obtain variational equations for trajectory. Assuming that trajectory is parameterized in some independent parameter σ, we can write it as

$$\delta \int_{\sigma_0}^{\sigma_1} T(x(\sigma)) s(x'(\sigma)) d\sigma + \delta \int_{\sigma_0}^{\sigma_1} A(x(\sigma) x'(\sigma) d\sigma = 0$$

Without independent parameterization:

$$0 = \int \nabla T dl \delta x + \int T \frac{(dx d\delta x)}{dl} .$$

Second term is integrated by parts to obtain

$$\nabla T - \frac{d}{dl}(T\hat{\boldsymbol{\tau}}) = 0 ,$$

where $T(x) = \sqrt{2(E - V(x))}$, $s(x') = \sqrt{\sum (x')^2}$. Expanding the differentials one gets

$$\nabla T(x)(\mathbf{1} - \hat{\boldsymbol{\tau}}\hat{\boldsymbol{\tau}}) - T\frac{d\hat{\boldsymbol{\tau}}}{dl} = 0$$

Integration by parts results in variational equation

$$\frac{\partial T(x)}{\partial x_i} s(x') - \frac{d}{d\sigma}\left(T(x)\frac{\partial s(x')}{\partial x_i'}\right) + \sum_j \left(\frac{\partial A_i(x)}{\partial x_j} - \frac{\partial A_j(x)}{\partial x_i}\right) x_j' = 0$$

which we will use to determine trajectories between two given points. Note that the magnetic term is $x_j' F_{ji}$, and in the crossed fields problem it is $B(x_1'\hat{x}_2 - x_2'\hat{x}_1)$. Note that $x'/s = \hat{\boldsymbol{\tau}}$ tangent vector to the trajectory, and $s(x')d\sigma = \sqrt{\sum (dx)^2} = dl$ is the length element. Dividing the above equation by $s(x')$, on obtains parameterization independent variational equation

$$\nabla T(x) - \frac{d}{dl}\left(T(x)\hat{\boldsymbol{\tau}}\right) + \hat{\boldsymbol{\tau}} \cdot \hat{\mathbf{F}}(x) = 0 \tag{2.31}$$

CHAPTER III

CROSSED FIELDS

This chapter provides preliminary investigations to subsequent Chapter 4 and Chapter 6. Apart from introducing key equations, such as the Hamiltonian in Eq. (3.1), we will study limits of strong fields, perturbative regime, and the onset of chaos via geometric perturbation theory (also called the Melnikov analysis).

3.1 Static properties of the phase space

3.1.1 Hamiltonian and the equations of motion

The crossed-fields **Hamiltonian** (in atomic units) looks deceptively simple:

$$H_B = \frac{1}{2}\left(p_x - By/2\right)^2 + \frac{1}{2}\left(p_y + Bx/2\right)^2 + \frac{1}{2}p_z^2 - 1/r + Fx, \tag{3.1}$$

but comes with a bewildering wealth of dynamics (see Chapter 4). Commonly $B = 1$ scaling is used, but we shall keep all three parameters (for discussion of scaling, see Appendix A.1). Without loss of generality we may choose $F > 0$.

The **equations of motion** are obtained using standard Hamiltonian formalism and Eq. (3.1)

$$\begin{cases} \dot{x} &= p_x - By/2 \\ \dot{p}_x &= -x/r^3 - Bp_y/2 - B^2x/4 - F \\ \dot{y} &= p_y + Bx/2 \\ \dot{p}_y &= -y/r^3 + Bp_x/2 - B^2y/4 \\ \dot{z} &= p_z \\ \dot{p}_z &= -z/r^3 \end{cases} \tag{3.2}$$

Detailed analysis of the phase space dynamics will require knowledge of the behavior of a distribution of trajectories, which locally is governed by the properties of the first variational

equation:

$$\begin{cases} d\dot{x} & = dp_y - (B/2)dy \\ d\dot{p}_x & = \left[(3x^2 - r^2)/r^5 - B^2/4\right] dx + (3xy/r^5)dy - (B/2)dp_y + (3xz/r^5)dz \\ d\dot{y} & = (B/2)dy + dp_y \\ d\dot{p}_y & = (3xy/r^5)dx + (B/2)dp_x + \left[(3y^2 - r^2)/r^5 - (B^2/4)\right] dy + +(3xz/r^5)dz \\ d\dot{z} & = dp_z \\ d\dot{p}_z & = (3xz/r^5)dx + (3yz/r^5)dy + \left[(3z^2 - r^2)/r^5\right] dz \end{cases} \tag{3.3}$$

3.1.2 Time reversibility

Hamiltonian system are said to be time reversible if the symmetry operation

$$T(P_1, \ldots, P_N, Q_1, \ldots, O_N) = (-P_1, \ldots, -P_N, Q_1, \ldots, Q_N) \tag{3.4}$$

leaves the Hamiltonian $H(Q_1, \ldots, P_N)$ invariant and the equations of motion acquire an overall sign change. Because the Hamiltonian of Eq. (3.1) has terms, that are linear in $P_i Q_j$, and are not invariant with respect to symmetry operation T, this Hamiltonian is considered as non time-reversible (see for example [65]). The equations of motion Eq. (3.2) maintain their form if time direction is reversed *together* with the signs of y and p_x. We can show, that there is a linear coordinate transformation (singular at $B = 0$), which transforms the Hamiltonian of Eq. (3.1) into a Hamiltonian of Eq. (3.6), which is explicitly time reversible in the new set of coordinates. The transformation

$$\begin{cases} Q_1 & = (-p_y - Bx/2)/\sqrt{B} \\ P_1 & = (-p_x + By/2)/\sqrt{B} \\ Q_2 & = (p_y - Bx/2)/\sqrt{B} \\ P_2 & = (-p_x - By/2)/\sqrt{B} \\ Q_3 & = z \\ P_3 & = p_z \end{cases} \tag{3.5}$$

has the following properties:

1. It is symplectic, i.e. it preserves the Poincaré invariant

$$\sum P_i dQ_i = p_x dx + p_y dy + p_z dz\,.$$

2. The Hamiltonian, expressed in the new variables has momentum dependence in the potential.

3. The Hamiltonian in new variables is "time-reversible" in the usual sense (of Eq. (3.4)) and in particular trajectories of have the symmetry of an oscillator $T(q_i, P_i) = (q_i, -P_i)$ in each degree-of-freedom.

The proof follows by construction. The new Hamiltonian in the new variables

$$\tilde{H} = \frac{1}{2}\left[B(P_1^2 + Q_1^2) + P_3^2\right] - \sqrt{B}/\tilde{r} - \frac{1}{\mathcal{R}_F^2\sqrt{B}}(Q_1 + Q_2), \tag{3.6}$$

where $\tilde{r}^2 = (P_1 - P_2)^2 + (Q_1 + Q_2)^2 + BQ_3^2$. Because $\tilde{r}$ is a homogeneous polynomial of order two in momenta, the $\tilde{r}$ is T-invariant. All the remaining terms in Eq. (3.6) contain only square terms of P_i, and therefore $\tilde{H}$ can be easily shown to be T-invariant.

3.1.3 Geometric parameters

In many instances it is worthwile to eliminate the original (F, E) parameters in favor of a new set of parameters (s,μ) which may not be directly measurable, but are more convenient for the analysis. In particular they scale as distance and therefore have a geometric interpretation. We introduce $s = F^{-1/2}$, and $\mu = -2/E$, and assuming we are in the range of $E < 0$; we require that $\mu > 0$. An artificial singularity in the range of ultra-high energies, $E = 0$ and higher, is not relevant because all the effects, attributed to chaotic dynamics are present already at negative energies.

$$F = 1/s^2 \quad E = -2/\mu \tag{3.7}$$

The merits of geometric parameters will be used studying geometric constraints imposed by the Hamiltonian on the phase space, and when studying the integrable and nearly integrable limits.

3.1.4 Boundaries in phase space

The Hamiltonian of the crossed-fields problem (Eq. (3.1)) defines a one-parameter family of 5-dimensional invariant surfaces, parametrized by energy. For a fixed energy, this surface defines a region of the phase space, that can be used to sample the trajectories, and that can be reached, at least in principle by trajectories with a given energy. In the context of lunar dynamics, three body and other celestial mechanics problems, this domain is usually called the Hill's region. The boundary of this domain is called the zero velocity surface. Its

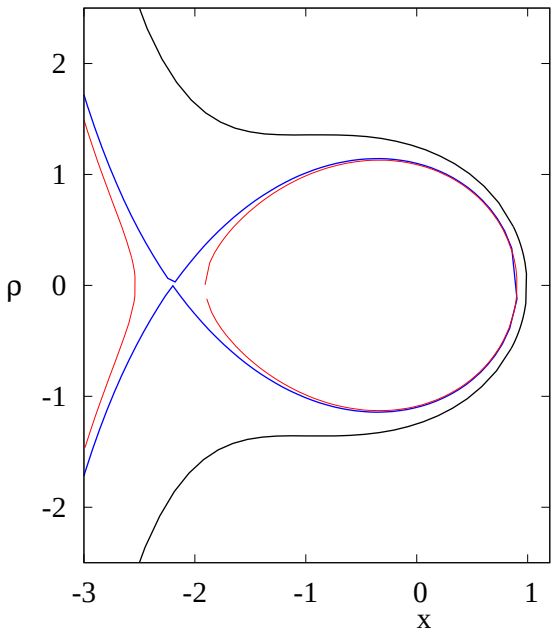


Figure 3.1: The zero velocity curve (see Eq. (3.9)) of the crossed-fields Hamiltonian of Eq. (3.1) for several energy parameters and fixed electric field parameter $s = 2.2$. Because of symmetry, $p_x = y/2$ and $p_y = -x/2$, the placeholder ρ may be replaced by any of (y,$z = 0$), $2p_x$. Several curves reflect the setting studied in this thesis ($s = 2.2$, $\mu = 2.5$, black curve) and examples of critical energy ($s = \mu = 2.2$, blue curve) and of a spatially bounded setting with energy slightly (1%) below the critical value ($s = 2.2$, $\mu = 2.178$, red curve).

projection on the configuration space (x, y, z) does not cover entire space. The boundaries of this surface are defined by the zero velocity condition in Eq. (3.1), which has the form of $H_B = v^2/2 + \text{pot. energy}$. In particular we solve

$$E = -1/r + Fx \tag{3.8}$$

The zero velocity curve has the explicit form

$$y^2 + z^2 = -x^2 + \frac{s^4}{(x + 2s^2/\mu)^2}, \tag{3.9}$$

We have defined $\rho = \sqrt{y^2 + z^2}$ and plotted several representative curves with $s = 2.5$ in Figure 3.1.4. Depending on the value of s/μ, the phase space comprises two disjoint domains ($s/\mu > 1$), or one domain ($s/\mu \leq 1$) (see Figure 3.1.4). In the former case interesting dynamics happens inside a closed volume which is approximately an ellipsoid of rotation, centered at the origin with the major semi-axes

$$\begin{aligned} a_x &= \frac{s^2}{\mu}\left(1 - \sqrt{1 - \frac{\mu^2}{s^2}}\right) \\ a_\rho &= \frac{\mu}{2} \end{aligned}$$

In the limit $\mu \ll s$ this volume approaches the sphere with radius $R = \mu/2$. The open volume consists of left half-plane, approximately, with a wall at $x = -2s^2/\mu$.

These volumes are separated by a boundary layer, with a width $d \approx \frac{2s^2}{\mu}\sqrt{1 - \frac{\mu^2}{s^2}}$. When $s/\mu < 1$, the boundary layer vanishes, in a merging of the two domains. There opens a channel between the two domains, of diameter roughly $\frac{2s^2}{\mu}\sqrt{\frac{\mu^4}{s^4} - 1}$.

In the critical case ($s/\mu = 1$) the domains just touch at a point. This point is actually a dynamical equilibrium point, $v = 0$. Its linear stability is of type center-center-saddle. For $\mu > s$ there is a Hopf cycle in the neighborhood of $(x = -\frac{s^2}{\mu}, y = 0, z = 0)$. The critical situation reflects a pivotal situation, the corresponding energy is called the "Stark" (saddle point) energy $E = -2/\mu = -2\sqrt{F}$.

The system becomes open, making it possible for the body under investigation (electron) to penetrate from nuclear to external region through a channel in a neighborhood of a saddle point. The dynamics in this area is especially sensitive and complicated. In the context of atomic physics this phenomenon models (chaotic) ionization. In a more general setting this system is a suitable model to investigate problems of absolutely different origins: chemical reactions and astrodynamics for it is a minimalist model to capture complicated dynamics of three degrees of freedom systems near saddles of potential energy surface.

One way to parametrize the hills region is to use a set of parameters (p, θ_1, θ_2,θ_3,θ_4), where

$$
\begin{aligned}
x(p) &= p && (3.10)\\
y(p,\theta_1) &= \rho(p)\cos\theta_1 && (3.11)\\
z(p,\theta_1) &= \rho(p)\sin\theta_1 && (3.12)\\
p_x(p,\theta_1,\theta_2,\theta_3) &= \nu(p,\theta_1)\cos\theta_2\cos\theta_3 + By(p,\theta_1)/2 && (3.13)\\
p_y(p,\theta_1,\theta_2,\theta_3) &= \nu(p,\theta_1)\cos\theta_2\sin\theta_3 - Bp/2 && (3.14)\\
p_z(p,\theta_1,\theta_2,\theta_3) &= \nu(p,\theta_1)\sin\theta_2 && (3.15)
\end{aligned}
$$

where $\rho(p)$ and $\nu(p,\theta_1)$ are defined as:

$$
\begin{aligned}
\rho(p) &= = \sqrt{-p^2 + s^4/(p+2s^2/\mu)^2} && (3.16)\\
\nu(p,\theta_1) &= \sqrt{E + 1/r(p) - p/s^2} && (3.17)\\
r(p) = &= \sqrt{\rho^2(p) + p^2} && (3.18)
\end{aligned}
$$

The parameter $p \subset \mathbb{R}$ spans the range of allowed values of the x coordinate (in fact p is equal to x). The range is defined by requiring that the left-hand side of Equations (3.16)–(3.18) be real. The remaining parameters are angular; the range of θ_1 is a circle, $\theta_1 \in S^1$; the range of a pair θ_2 and θ_3 is a sphere, $(\theta_2,\theta_3) \in S^2$.

3.2 Limits of strong fields

The crossed-fields scaled Hamiltonian has two parameters, s and E, and depending on their magnitudes several limiting regimes are possible. Different limits imply different types of qualitative dynamics. The limit of strong magnetic field corresponds to large s and, strong electric field and strong Coulomb field. The first limit, of strong magnetic field occurs when influence of potential is small, is realized for small electric field parameter and high energy or large distance from the origin. The second - electric - limit occurs when electric field parameter is large. The third - Coulomb - limit corresponds to low energy and field parameter not too large. The phase space dynamics is qualitatively different in each of these limits. In the coulomb or electric field limits trajectory is concentrated in the core, near origin of coordinates. Velocity exhibits very large fluctuations, when solution approaches

singularity. In contrast, the magnetic field limit, forces solution to explore larger part of configuration space, not spending much time in the core.

3.2.1 Strong magnetic field limit

The qualitative behavior of trajectories can be roughly divided in two parts: magnetic propagation in smooth potential and reflection off the hard wall. Given a particular small neighborhood in configuration space where third and higher derivatives of $1/r$ potential are small, we expand this potential in power series and retain only the quadratic terms,

Any such trajectory in plane and most of trajectories in 3d will eventually hit the core region. Owing to steep potential curve the motion may be approximated by an instantaneous reflection.

3.2.2 Zero magnetic field: Integrable limit

If a singular limit of magnetic field $B = 0$ in Eq. (3.1), the dynamics changes drastically. The Hamiltonian looks similar,

The *Stark Hamiltonian* describes motion of a particle in coupled Coulomb potential and linear homogeneous fields. It is a zero magnetic field limit of Crossed Fields Hamiltonian

$$H = \frac{1}{2}\left(y_1^2 + y_2^2 + y_3^2\right) - \frac{1}{r} + \frac{x_1}{s^2} = -\frac{2}{\mu}\,. \tag{3.19}$$

This Hamiltonian has only one length scale, which means that the only relevant parameter is a ratio of length scales s and μ.

$$\lambda = s/\mu \tag{3.20}$$

Bounded solutions are only possible if energy is negative, which translates to $\mu > 0$.

The semi-parabolic coordinates (ξ, η, ϕ) are introduced as a contact transformation,

$$x = (\xi^2 - \eta^2)/2, \quad y = \xi\eta\cos(\phi), \quad z = \xi\eta\sin(\phi)$$

$$\begin{aligned} x_1 &= x, \quad X_1 = p_x, & & y_1 = \eta, \quad Y_1 = p_\eta, \\ x_2 &= y, \quad X_2 = p_y, & \text{and} \quad & y_2 = \xi, \quad Y_2 = p_\xi, \\ x_3 &= z, \quad X_3 = p_z. & & y_3 = \phi, \quad Y_3 = p_\phi, \end{aligned}$$

or, equivalently, via a generating function

$$W \;=\; p_1(\xi^2-\eta^2)/2 + p_y\xi\eta\cos(\phi) + p_z\xi\eta\sin(\phi)\,,$$

leading to

$$\begin{aligned} Y_1 &= \frac{\partial W}{\partial y_1} \;=\; X_1 y_2 + X_2 y_1\cos(y_3) + X_2 y_2\sin(y_3) \\ Y_2 &= \frac{\partial W}{\partial y_2} \;=\; -X_1 y_1 + X_2 y_1\cos(y_3) + X_2 y_2\sin(y_3) \\ Y_3 &= \frac{\partial W}{\partial y_3} \;=\; X_1 y_2 + X_2 y_1\cos(y_3) + X_2 y_2\sin(y_3)\,. \end{aligned} \tag{3.21}$$

In this section we investigate limit when $E=-2/\mu$ and $F=1/s^2$ are held fixed and B increases from zero to one. Limit when $B=0$ describes separable Hamiltonian. We investigate resonance conditions in the integrable limit and apply Poincaré theorem and its generalizations [75, 76] to determine which D dimensional tori frequency lock in corresponding resonance conditions and survive as $D-1$ dimensional tori. We shall attempt to find (numerical) solutions for nonzero magnetic field by continuation of unperturbed tori. Our goal is to continue solutions to $B=1$ limit.

3.2.3 Separating transformation, complete solution

Hamiltonian of Eq. (3.1) is separable in modified parabolic coordinates

$$x_1 \;=\; (\xi_1^2-\xi_2^2)/2, \quad x_2 \;=\; \xi_1\xi_2\cos\xi_3, \quad x_3 \;=\; \xi_1\xi_2\sin\xi_3 \;\;. \tag{3.22}$$

The system has Liouville form and its integration is standard, leading to equations

$$\begin{aligned} \tilde{H} &= 2r\,(H+2/\mu)+2 = h_1(\xi_1,\eta_1,\eta_3)+h_2(\xi_2,\eta_2,\eta_3) \\ dt &= (\xi_1^2+\xi_2^2)\,d\tau = 2r\,d\tau\,, \end{aligned}$$

where

$$h_1(\xi_1,\eta_1,\eta_3) \;= \tfrac{\eta_1^2}{2} + \tfrac{\eta_3^2}{\xi_1^2} + \tfrac{2\xi_1^2}{\mu} + \tfrac{\xi_1^4}{2s^2} \tag{3.23}$$

$$h_2(\xi_2,\eta_2,\eta_3) \;= \tfrac{\eta_2^2}{2} + \tfrac{\eta_3^2}{\xi_2^2} + \tfrac{2\xi_2^2}{\mu} - \tfrac{\xi_2^4}{2s^2}\,, \tag{3.24}$$

with constraint $h_1+h_2=2$. Moreover, by requiring that $\eta_i^2\xi_i^2 \geq 0$, we find additional constraints $h_1>0$, and $h_2>0$. Hence $0<h_i<2$, but sharper constraints will be imposed

as we examine the form of Eq. (3.23) and Eq. (3.24) more closely. We find it convenient to introduce parameter $-1 \leq a \leq 1$.

$$1+a \quad = 2p_1 = h_1, \qquad 1-a \quad = 2p_2 = h_2\,.$$

The cyclic momentum $\eta_3 = const$ and we note that degree of freedom associated with ξ_3, η_3 is rotational and doubly degenerate. The remaining degrees of freedom are oscillator-like.

$$\frac{1}{2}\left(\frac{d\xi_1}{d\tau}\right)^2 = h_1 - \frac{\eta_3^2}{\xi_1^2} - \frac{2\xi_1^2}{\mu} - \frac{\xi_1^4}{2s^2} \tag{3.25}$$

$$\frac{1}{2}\left(\frac{d\xi_2}{d\tau}\right)^2 = h_2 - \frac{\eta_3^2}{\xi_2^2} - \frac{2\xi_2^2}{\mu} + \frac{\xi_2^4}{2s^2}\,. \tag{3.26}$$

In particular, multiplying both sides of Eq. (3.25) by ξ_1^2 and examining the right hand side, one concludes that (ξ_1, η_1) is describe libration for all parameter values, whereas multiplication of equation Eq. (3.26) by ξ_2^2 and examination of its right hand side confirms that librational or rotational modes can be realized, much like in an inverted quartic potential. To integrate Eq. (3.25), Eq. (3.26) we make the ansatz

$$\xi_1^2 = P_1 + A_1 x_1^2\,, \qquad \xi_2^2 = P_2 + A_2 x_2^2\,, \tag{3.27}$$

and require that both $x_1(\tau)$ and $x_2(\tau)$ satisfy

$$\left(\frac{dx_i}{d\tau}\right)^2 = \Omega_i^2(1-(1+k_i^2)x_i^2 + k_i^2 x_i^4) \tag{3.28}$$

Given form of equations motion in this form is standard form of Jacobi functions, hence the solutions are

$$x_i(\tau) = \mathrm{cn}(\Omega_i(\tau - \tau_i)|k_i) \tag{3.29}$$

(see [88] for a discussion of Jacobi elliptic functions from a dynamical systems point of view). It is of interest to locate the separatrix of this system. The Hamiltonian $h_2(\xi_2, \eta_2)$ has two heteroclinic points. In original cartesian coordinates there is only one homoclinic critical point which is an image of the parabolic transformation of the two heteroclinic points of $h_2(\xi_2, \eta_2)$. The transformation maps two points and their manifolds onto each other, which is done by folding through a horizontal symmetry axis and twisting by π the (ξ_2, η_2) plane.

The heteroclinic point can be detected by solving for $k_i = 1$. Note that if $k_i = 1$, then $x_i' = \Omega_i|1 - x_i^2|$, and if $x = 1 + \varepsilon$, then $\varepsilon' = 2\Omega_i|\varepsilon|$, which shows exponential convergence from the left and exponential divergence from the right of critical point $\varepsilon = 0$. Another way to look at it is to note that $\mathrm{cn}(t|1) = \tanh t$. Only $k_2 = 1$ can be solved consistently with other requirements.

Consistency conditions are then

$$\begin{aligned} \frac{P_1^3}{2s^2} + \frac{2P_1^2}{\mu} - h_1 P_1 + \eta_3^2 &= 0\,, \qquad \frac{3P_1^2}{s^2} + \frac{8P_1}{\mu} - 2h_1 = -A_1\Omega_1^2 \\ \frac{3P_1}{s^2} + \frac{4}{\mu} &= \Omega_1^2(1+k_1^2)\,, \qquad A_1 = -s^2\Omega_1^2 k_1^2 \end{aligned} \tag{3.30}$$

$$\begin{aligned} \frac{P_2^3}{2s^2} - \frac{2P_2^2}{\mu} + h_2 P_2 - \eta_3^2 &= 0\,, \qquad \frac{3P_2^2}{s^2} - \frac{8P_2}{\mu} + 2h_2 = A_2\Omega_2^2 \\ -\frac{3P_2}{s^2} + \frac{4}{\mu} &= \Omega_2^2(1+k_2^2)\,, \qquad A_2 = s^2\Omega_2^2 k_2^2 \end{aligned} \tag{3.31}$$

3.2.4 Definition of h_i and η_3 in general case

The range of allowed free parameters will be determined. The parameters at our disposition are h_1, h_2, η_3, which so far are constrained only by trivial requirements, $h_1 > 0, h_2 > 0$, $h_1 + h_2 = 2$. We will find sharper boundaries of parameter ranges. Define parameters

$$p_1 = h_1/2, \qquad p_2 = h_2/2, \qquad a = s/\mu\,.$$

Two basic inequalities have to be considered.

The first inequality is

$$-\eta_3^2 + h_1 x - 2x^2/\mu - x^3/(2s^2) > 0, \qquad x > 0\,.$$

We find that there is one critical point,

$$x_1^c = \frac{4s^2}{3\mu}(r_+ - 1), \qquad r_+ = \sqrt{1 + \frac{3p_1}{4a^2}}\,,$$

and substituting value of x_1^c into inequality, we obtain the condition for η_3,

$$0 \le \eta_3^2 \le \frac{4^3 s^4}{3^3\mu^3}\left(\frac{1}{2} - \frac{3r_+^2}{2} + r_+^3\right)\,.$$

The second inequality reads

$$-\eta_3^2 + h_2 x - 2x^2/\mu + x^3/(2s^2) > 0, \qquad x > 0\,.$$

In this case we must enforce that two critical points exist,

$$x_\pm^c = \frac{4s^2}{3\mu}(1 \pm r_-), \qquad r_- = \sqrt{1 - \frac{3p_2}{4a^2}}\,,$$

which requires that $r_-^2 > 0$, that is,

$$p_2 < 4a^2/3\,,$$

and we find that

$$\eta_3^2 \leq \frac{4^3 s^4}{3^3\mu^3}\left(\frac{1}{2} - \frac{3r_-^2}{2} + r_-^3\right), \qquad \eta_3^2 \geq \frac{4^3 s^4}{3^3\mu^3}\left(\frac{1}{2} - \frac{3r_-^2}{2} - r_-^3\right).$$

Combine them all to find that

$$\frac{32s^4}{27\mu^3}\max\left(0, 1 - 3r_-^2 - 2r_-^3\right) \leq \eta_3^2 \leq \frac{32s^4}{27\mu^3}\min\left(1 - 3r_+^2 + 2r_+^3, 1 - 3r_-^2 + 2r_-^3\right).$$

The space of solutions for a fixed energy has two independent parameters. It is convenient to take p_1 and η_3. The domain of definition is a simply connected, energy-dependent area in the (p_1, η_3) plane.

3.2.5 Planar limit

Limiting case of $\eta_3 = 0$ corresponds to planar problem, such that $x_3 = y_3 \equiv 0$.

$$x_1 \;=\; (\xi_1^2 - \xi_2^2)/2, \quad x_2 \;=\; \sigma_{x_2}\xi_1\xi_2 \quad . \tag{3.32}$$

We notice, that if we take only absolute value of x_2, then parabolic transformation takes care of a symmetry $x_2 \to -x_2$. This symmetry is only exact in the integrable limit. When $B \neq 0$, it is no longer a symmetry. The exact symmetry for $B \neq 0$ will be discussed below. In the integrable limit usual time reversal symmetry is also present. Hence the symmetry reduced domain is defined by $(\xi_1, |\eta_1|, \xi_2, |\eta_2|)$.

The dynamics is defined by two separate Hamiltonians h_1 and h_2, which are of the form

$$h_i(\xi_i, \eta_i) = \frac{\eta_i^2}{2} + V_i(\xi_i)$$

where $V_1(\xi_1) = \frac{2\xi_1^2}{\mu} + \frac{\xi_1^4}{2s^2}$, $V_2(\xi_2) = \frac{2\xi_2^2}{\mu} - \frac{\xi_2^4}{2s^2}$ (see Figure 3.2.5). We also have that $h_1 = 1+a$, $h_2 = 1 - a$.

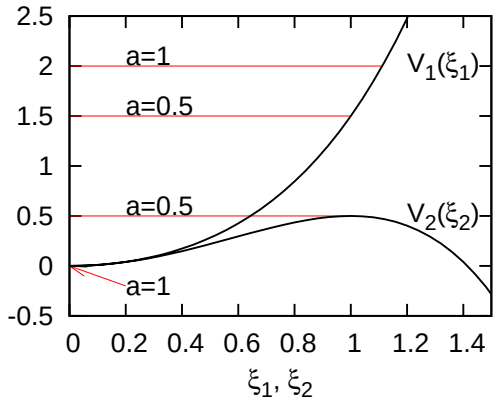


Figure 3.2: Plots of potential in the planar limit, with $s = 1$, $\mu = 2$.

In this situation both $\xi_1 \geq 0$ and $\xi_2 \geq 0$, can reach zero. Since $A_1 < 0$, one is lead to conclude that $P_1 > 0$ and $A_1 = -P_1$. Similarly, $A_2 > 0$, hence $P_2 = 0$. From (3.30) with definitions of (3.25) one finds

$$P_1 = 2s\lambda\left(\sqrt{1 + p_1/\lambda^2} - 1\right), \qquad \Omega_1^2 = \frac{2P_1}{s^2} + \frac{4}{\mu}, \qquad k_1^2 = \frac{1}{2}\frac{1}{1 + 2s\lambda/P_1}.$$

Introduce shorthand notation $\Gamma_1 = \sqrt{1 + p_1/\lambda^2}$, then simplifies to

$$P_1 = 2s\lambda(\Gamma_1 - 1), \qquad \Omega_1^2 = \frac{4\Gamma_1}{\mu}, \qquad k_1^2 = \frac{\Gamma_1 - 1}{2\Gamma_1}. \tag{3.33}$$

In the second case one has to solve equations

$$\frac{2h_2}{s^2} = \Omega_2^4 k_2^2, \qquad \frac{4}{\mu} = \Omega_2^2(1 + k_2^2),$$

which can be written in terms of

$$\Gamma_2 = \sqrt{1 - p_2/\lambda^2}$$

as

$$\Omega_2^2 = \frac{2(1 + \Gamma_2)}{\mu}, \qquad A_2^2 = 2s\lambda(1 - \Gamma_2), \qquad k_2^2 = \frac{1 - \Gamma_2}{1 + \Gamma_2}. \tag{3.34}$$

A torus with frequency ratio $r(a) = \Omega_2(a)/\Omega_1(a)$ can be found by solving $r^2(a) = (1+\Gamma_2)/(2\Gamma_1)$, which is an equation in interaction parameter λ and a only:

$$r^2(a) = \frac{\sqrt{2}\lambda + \sqrt{2\lambda^2 + a - 1}}{2\sqrt{2\lambda^2 + a + 1}}\,. \tag{3.35}$$

From this equation we obtain tight bounds for parameter a: $a \geq \max(-1, 1-2\lambda^2)$, $a \leq 1$, i.e.

$$a_{\min} = \begin{cases} 1 - 2\lambda^2, & \lambda \leq 1 \\ -1, & \lambda \geq 1 \end{cases}$$

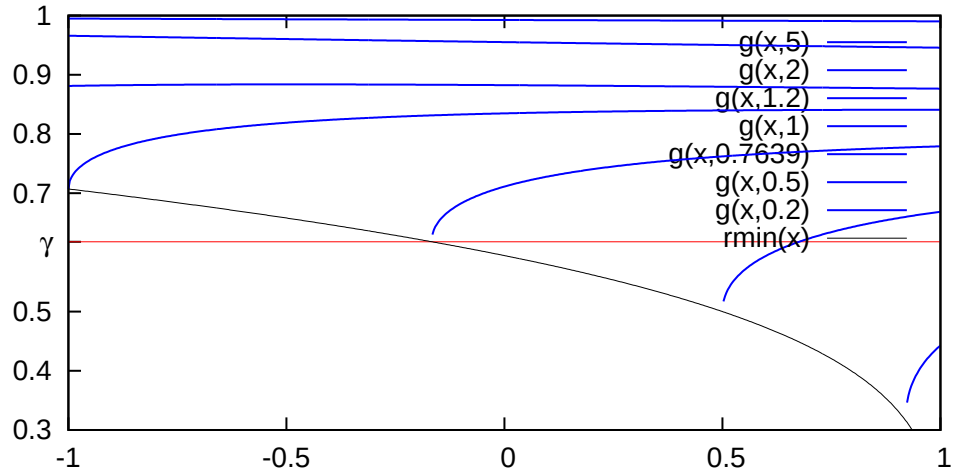


Figure 3.3: Plots of frequency ratio $r(a) = \Omega_2(a)/\Omega_1(a)$ versus a for an integrable limit of planar crossed-fields.

The border between the two regions is marked by parameters for which the systems transitions from closed to open, $s = \mu$, and higher energies and more open system does not create new frequencies. We note that $r^2(a_{\max}) = \lambda/\sqrt{\lambda^2+1}$ and

$$r^2(a_{\min}) = \begin{cases} \lambda/2, & \lambda \leq 1 \\ (1 + \sqrt{\lambda^2 - 1}/\lambda)/2, & \lambda \geq 1 \end{cases}$$

In particular we find that $r(a) = \gamma$ only for $0.4133 < \lambda < 0.7639$, where γ is golden mean. We also find that $\lim_{\lambda\to\infty} r(a) = 1$.

Using this information we can select parameter values for which invariant torus is exactly resonant.

If $\lambda = s/\mu$ is large, system is closed and centered in the vicinity of the origin; influence of the electric field is small and motion experiences predominantly forces arising from the Coulomb potential. The motion in Coulomb potential is globally closed and degenerate, therefore frequency ratio approaches $r(a) = 1$ for all parameter a values (see Figure 3.3). The much richer dynamical picture can be expected to emerge when $\lambda < 1$ as frequency ratio range is larger. In particular, golden mean torus exists only if $0.4133 < \lambda < 0.7639$.

Value of $\lambda = 1/2$ is a good candidate for study. This problem has scaling invariance, such that only the ratio of s/μ is relevant. Frequency ratios range between $1/2 \leq \Omega_2(a)/\Omega_1(a) \leq 5^{-1/4} \approx 0.66874$.

3.2.6 Levi-Civita regularization

The Levi-Civita regularization procedure eliminates the singular behavior of Coulomb potential by rescaling both time and coordinates (so-called "square root" transformation. See Kustaanheimo-Stiefel transformation [72, 111] for generalizations to 3-dof and [6] for a spinor formalism of Kustaanheimo-Stiefel transform).

If we rewrite the Hamiltonian of Eq. (3.1), with $z \equiv 0$, $p_z \equiv 0$, and redefined $y_1 \equiv x$, $y_2 \equiv y$, $Y_1 \equiv p_x$, $Y_2 \equiv p_y$, $y \equiv [y_1, y_2]^{\mathrm{T}}$, and finally set $B \equiv \epsilon$, we obtain

$$\begin{aligned} H &= \frac{1}{2}\left((Y_1 - \epsilon y_2)^2 + (Y_2 + \epsilon y_1)^2\right) - \frac{1}{\sqrt{y_1^2 + y_2^2}} + \frac{y_1}{s^2} \\ &= \frac{1}{2}\left(Y + \epsilon\sigma y\right)^2 - \frac{1}{\sqrt{y_1^2 + y_2^2}} + \frac{y_1}{s^2} \end{aligned} \tag{3.36}$$

where

$$\sigma = \begin{pmatrix} 0 & 1 \\ -1 & 0 \end{pmatrix}$$

A contact transformation

$$y = \frac{1}{2}\Lambda(\mathbf{z})\mathbf{z}, \quad Y = \mathbf{z}^{-2}\Lambda(\mathbf{z})\mathbf{Z}, \qquad\qquad \Lambda(\mathbf{z}) = \begin{pmatrix} z_1 & -z_2 \\ z_2 & z_1 \end{pmatrix} \tag{3.37}$$

is called Levi-Civita transformation. The transformations Eq. (3.37) have the following nice

properties:

$$\begin{aligned} d\mathbf{y} &= \Lambda(\mathbf{z})d\mathbf{z} \\ \mathbf{Y}d\mathbf{y} &= \mathbf{Z}d\mathbf{z} \\ \Lambda(\mathbf{z})\Lambda^T(\mathbf{z}) &= \mathbf{z}^2 \end{aligned}$$

The reduction comprises change of variables by Eq. (3.37) and reparametrization of time variable $t \mapsto \tau$ by

$$dt = \mathbf{z}^2 d\tau\,. \tag{3.38}$$

The regularized Hamiltonian is obtained using the usual procedure bring the Hamiltonian into a regularized form

$$K(\mathbf{z},\mathbf{Z}) = \mathbf{z}^2\left(H + 2/\mu\right) + 2 = \frac{\mathbf{Z}^2}{2} + \frac{2\mathbf{z}^2}{\mu} + \frac{z_1^4 - z_2^4}{2s^2} + \frac{\varepsilon\mathbf{z}^2(\mathbf{z}\sigma\mathbf{Z})}{8} + \frac{\varepsilon^2\mathbf{z}^6}{32} \tag{3.39}$$

$$= K_+(z_1,Z_1) + K_-(z_2,Z_2) + \varepsilon K_1(\mathbf{z},\mathbf{Z}) + O(\varepsilon^2)\,. \tag{3.40}$$

We have introduced new integrable Hamiltonians $K_\pm$ which can be parameterized by a single parameter χ, measuring distance to the heteroclinic manifold of K_-. Interior of the cavity, bounded by the zero-velocity curve (see Figure 3.1.4, corresponds to $\chi > 0$. Heteroclinic motion corresponds to $\chi = 0$.

$$K_+(z_1,Z_1) = \frac{Z_1^2}{2} + \frac{2}{\mu}z_1^2 + \frac{z_1^4}{2s^2} = 2(1 - \frac{s^2}{\mu^2}(1-\chi^2)) \tag{3.41}$$

$$K_-(z_2,Z_2) = \frac{Z_2^2}{2} + \frac{2}{\mu}z_2^2 - \frac{z_2^4}{2s^2} = \frac{2s^2}{\mu^2}(1-\chi^2) \tag{3.42}$$

$$\begin{aligned} z_1^{(0)} &= A_1\,\mathrm{cn}\,(\Omega_1\tau + c_1|m_1); \\ z_2^{(0)} &= A_2\,\mathrm{sn}\,(\Omega_2\tau + c_2|m_2), \quad 0 < \chi < 1, \\ z_2^{(0)} &= A_2'/\,\mathrm{sn}\,(\Omega_2\tau + c_2'|m_2), \qquad \chi > 1. \end{aligned}$$

where

$$\begin{array}{lll} A_1 = \sqrt{\frac{2s^2}{\mu}\left(\sqrt{\frac{\mu^2}{s^2}+\chi^2}-1\right)}, & \Omega_1 = \sqrt{\frac{2}{\mu}\left(\sqrt{\frac{\mu^2}{s^2}+\chi^2}+1\right)}, & m_1 = \frac{\sqrt{\frac{\mu^2}{s^2}+\chi^2}-1}{\sqrt{\frac{\mu^2}{s^2}+\chi^2}+1} \\ A_2 = \sqrt{\frac{2s^2(1-\chi)}{\mu}}, & \Omega_2 = \sqrt{\frac{2(1+\chi)}{\mu}}, & m_2 = \frac{1-\chi}{1+\chi} \\ A_2' = \sqrt{\frac{2s^2(1+\chi)}{\mu}} & & \end{array} \tag{3.43}$$

The perturbed equations of motion are

$$\dot{Z}_1 = -\frac{2z_1^3}{s^2} - \frac{4z_1}{\mu} - \frac{\epsilon(2z_1(Z\sigma z) + z^2 Z_2)}{2} - \frac{6\epsilon^2 z^4 z_1}{8} \tag{3.44}$$

$$\dot{z_1} = Z_1 - \frac{\epsilon z^2 z_2}{2} \tag{3.45}$$

$$\dot{Z}_2 = \frac{2z_2^3}{s^2} - \frac{4z_2}{\mu} - \frac{\epsilon(2z_2(Z\sigma z) - z^2 Z_1)}{2} - \frac{6\epsilon^2 z^4 z_2}{8} \tag{3.46}$$

$$\dot{z_2} = Z_1 + \frac{\epsilon z^2 z_1}{2} \tag{3.47}$$

$$\tag{3.48}$$

3.2.7 The perturbation of heteroclinic connection

The two equilibria are connected via invariant manifolds, forming the so-called *heteroclinic* connection. The perturbation in the form of terms with pre-factor ϵ, destroy the connection. The stable and unstable manifolds are structurally stable in the sense, that they persist the perturbation. Their invariant character dictates, that if two such manifolds have a (transverse) intersection point, they necessarily have an infinity of them. The *heteroclinic tangle* arising from this topological necessity, gives rise to the chaotic layer in the neighborhood of manifolds. For small perturbations, the size of this layer maybe estimated, and the interpretation in terms of the splitting of the separatrices maybe given. Such approach is called a *geometric* perturbation theory, or the *Melnikov* method.

I shall treat the Hamiltonian $\tilde{H}$ perturbatively, disregarding the $O(\varepsilon^2)$ term completely and assuming that initially $0 < \chi \ll 1$. The procedure will be equivalent to considering motion on a projection of a phase space to (z_2, Z_2) and regarding K_1 as a periodic forcing. This method is in essence a reduction method. Expand $\mathbf{Z} = \mathbf{Z}^{(0)} + \varepsilon\mathbf{Z}^{(1)} + \ldots$ and substitute into Hamilton equations, to obtain the equations of motion for $\mathbf{Z}^{(1)}$. Looking only at a subspace $\mathbf{Z}_2$ the resulting equations are equivalent to those obtained from one degree of freedom Hamiltonian K_- plus a Hamiltonian perturbation εK_1. In this case rigorous proof exist that a $\mathbf{Z}_2^{(0)} + \varepsilon\mathbf{Z}_2^{(1)}$ approximate the true solution uniformly during the time interval of one traverse between heteroclinic points, which increases to infinity as the initial parameters approach the heteroclinic manifold. I exploit this fact and compute the change in K_- during

one traversal, i.e.

$$\Delta K_-(\mathbf{Z}^{(0)})- = \int_{-\infty}^{\infty} \frac{dK_-(\mathbf{Z}^{(0)}(\tau))}{d\tau} d\tau \tag{3.49}$$

Computation shows that

$$\frac{dK_-}{d\tau} = \varepsilon[K_-, K_1] \tag{3.50}$$

and therefore $\Delta K_- \sim M(t,0)$ where $M(t,0)$ is a Melnikov function, a measure of splitting of stable and unstable manifolds after perturbation. Relevant results of the Melnikov theory carry onto this case, i.e. if $M(t,0)$ has only simple zeros for sufficiently small ε then stable and unstable manifolds intersect transversally.

I parameterize the heteroclinic trajectory by θ re-scale the time once again $\Omega_1 d\tau = d\theta$ introduce shorthand notation $W = \Omega_2/\Omega_1$ and introduce a free parameter $\phi = c_2 - c_1/W$ (the second free parameter is fixed by choosing $z_2(\theta = 0)$ to be a point in the middle between the two equilibrium points).

$$\begin{aligned} z_1^{(0)}(\Omega_1\tau + c_1) &\approx \zeta_1(\theta) = A_1 \,\mathrm{cn}\,(\theta + \phi|m) \\ z_2^{(0)}(\Omega_2\tau + c_2) &\approx \zeta_2(\theta) = A_2 \left((1 + \frac{\chi}{2}) \tanh W\theta - \frac{\chi W\theta}{2} \,\mathrm{sech}^2\, W\theta \right) \end{aligned}$$

$$\begin{aligned} \mathrm{cn}\,(u) &= \frac{2\pi}{\sqrt{m}K} \sum_{n=1}^{\infty} \frac{q^{n-\frac{1}{2}}}{1+q^{2n-1}} \cos(2n-1)\frac{\pi u}{2K} \\ &\equiv \frac{2\pi}{\sqrt{m}K} \sum_{n=1}^{\infty} C_n \cos(2n-1)\frac{\pi u}{2K} \\ \mathrm{cn}^3\,(u) &= \frac{8\pi^3}{m^{\frac{3}{2}}K^3} \sum_{n=1}^{\infty} T_n \cos(2n-1)\frac{\pi u}{2K} \end{aligned}$$

where $q = \exp\,(-\frac{\pi K'}{K})$, K and K' are complete elliptic integrals of first kind of arguments m and $1-m$ respectively.

Then I substitute $\zeta_1(\theta)$ and $\zeta_2(\theta)$ in the $[K_-, K_1]$, and compute ΔK_-. The result can be put in a form

$$\begin{aligned} &\Delta K_-(\phi) = a \textstyle\sum_{n=1}^{\infty} C_n(\delta) \sin\left((2n-1)\omega(\delta)\phi\right) \\ &\left(-\frac{12 x_n(\delta)}{\pi} + \mathrm{csch}\,(\frac{\pi x_n(\delta)}{2})((x_n^2(\delta)-2)(x_n^2(\delta)+6) - \frac{8\pi^2(2+\delta)}{K^2(\frac{\delta}{2+\delta})} \frac{T_n(\delta)}{C_n(\delta)}(x_n^2(\delta)+6)) \right) \end{aligned}$$

Where $\delta = \mu/s - 1 > 0$, $x_n(\delta) = \frac{(2n-1)\pi}{2K(\delta/(2+\delta))}$, T_n, $C_n(\delta) = T_n$,$C_n(K(\delta/(2+\delta)), K'(\delta/(2+\delta)))$.

The fact that ΔK_- was calculated in $\mathbf{Z}$ coordinates is not essential, by virtue of invariance of Poisson brackets under canonical transformations. Therefore the same character of splitting is expected in cartesian coordinates. The main difference is in terminology, namely heteroclinic equilibria are by the coordinate transformation identified, and heteroclinic manifolds in $\mathbf{Z}$ is a homoclinic tangle in $\mathbf{Y}$.

Analysis of terms in ΔK_- shows that for a large range of values of δ zeros of ΔK_- are only those where $\sin(\omega(\delta)\phi) = 0$ and that $M'_\phi \neq 0$ at these points. Therefore stable and unstable manifolds intersect transversally for sufficiently small ε. Since the system possesses scaling property, discussed in the first chapter, I conclude that homoclinic tangle is transversal for arbitrary values of ε. Numerical integration of stable and unstable manifolds backs up this conclusion.

The action is

$$I_+ = \oint Z dz = 4s^2 a_1^2 b_1 \int_0^K sn^2 dn^2 du \tag{3.51}$$

Since

$$\int_0^K \mathrm{sn}^2\,\mathrm{dn}^2\,du = \frac{(2k^2-1)E + (1-k^2)K}{3k^2} \tag{3.52}$$

by substituting this expression and $k_1 = \frac{a_1}{b_1}$, we obtain

$$I_+ = 4s^2 a_1^2 b_1 \frac{(2k_1^2-1)E_1 + (1-k_1^2)K_1}{3k_1^2} \tag{3.53}$$

For K_- the solution splits according to the values of α_-^2:

If $U^2 > 4/s^2$ which corresponds to energies below the equilibrium point energy, then for $4/s^2 < \alpha_-^2 < U^2$ we have two solutions. Solution, corresponding to the bound motion,

$$z(\tau) = sa_2\,\mathrm{sn}(b_2\tau + c_{2b}|\frac{a_2}{b_2}) \tag{3.54}$$

along with conjugate momentum

$$Z_2 = sa_2b_2\,\mathrm{cn}(b_2\tau + c_2)\,\mathrm{dn}(b_2\tau + c_2) \tag{3.55}$$

$$a_2 = s\sqrt{\frac{2}{\mu}\left(1+\sqrt{1-\frac{\alpha_-^2\mu^2}{4}}\right)}$$
$$b_2 = s\sqrt{\frac{2}{\mu}\left(1-\sqrt{1-\frac{\alpha_-^2\mu^2}{4}}\right)}$$

Which is seen to be periodic, with period

$$T_- = \frac{4\mathcal{K}(\frac{a_2}{b_2})}{b_2} \tag{3.56}$$

and solution, corresponding to the unbound motion

$$z(\tau) = \frac{sb_2}{\mathrm{sn}(b_2\tau + c_{2u}|\frac{a_2}{b_2})} \tag{3.57}$$

If $\alpha_-^2 > U^2$, then the solution is .

If $\alpha_-^2 < 0$ then .

The action is

$$I_- = \oint Z dz = 4s^2 a_2^2 b_2 \int_0^K \mathrm{cn}^2\,\mathrm{dn}^2\,du \tag{3.58}$$

Since

$$\int_0^K \mathrm{sn}^2\,\mathrm{dn}^2\,du = \frac{(1+k^2)E-(1-k^2)K}{3k^2} \tag{3.59}$$

by substituting this expression and $k_2 = \frac{a_2}{b_2}$, we obtain

$$I_- = \frac{8s^2U}{3}b_2\left(\mathcal{E} - \frac{(U^2-\alpha_-^2)^{1/2}}{U}\mathcal{K}\right) \tag{3.60}$$

3.2.7.1 Perturbation analysis for orbits near homoclinic manifold

Let us investigate case of close to homoclinic trajectories. In connection with this introduce the parameter χ, such that

$$1 - \frac{\alpha_-^2\mu^2}{4} = \chi^2 \tag{3.61}$$

According to this definition the following parameters have values

$$1+\frac{\alpha_+^2\mu^2}{4}=\frac{\mu^2}{s^2}+\chi^2 \tag{3.62}$$

$$a_1 = \sqrt{\frac{2s^2}{\mu}\left(\sqrt{\frac{\mu^2}{s^2}+\chi^2}-1\right)} \tag{3.63}$$

$$b_1 = \sqrt{\frac{2s^2}{\mu}\left(\sqrt{\frac{\mu^2}{s^2}+\chi^2}+1\right)} \tag{3.64}$$

$$\frac{a_1}{a_2} = \frac{\mu-s}{\mu+s}+\chi^2\cdot... \tag{3.65}$$

$$a_2 = \sqrt{\frac{2s^2(1-\chi)}{\mu}} \tag{3.66}$$

$$b_2 = \sqrt{\frac{2s^2(1+\chi)}{\mu}} \tag{3.67}$$

$$\frac{a_2}{b_2} = 1-2\chi+\chi^2\cdot... \tag{3.68}$$

$$\tag{3.69}$$

In the light of the above expressions I will approximate functions $z_1(\tau)$ and $z_2(\tau)$ as

$$z_1(\tau)\sim\sqrt{\frac{2s^2}{\mu}\left(\sqrt{\frac{\mu^2}{s^2}+\chi^2}-1\right)}\,\mathrm{cn}\left(\sqrt{\frac{2s^2}{\mu}\left(\sqrt{\frac{\mu^2}{s^2}+\chi^2}+1\right)}\tau+c_1|\frac{\mu-s}{\mu+s}\right)$$
$$=A_1\,\mathrm{cn}(\Omega_1\tau+c_1) \tag{3.70}$$

$$\frac{dI_-}{dt}=-\frac{\mu^2}{4s^2\chi}\frac{dI_-}{d\chi}\frac{dK_-}{d\tau}$$
$$=-\frac{4\mu}{3\chi}\left(\frac{2s^2}{\mu}\right)^{1/2}\frac{d}{d\chi}\left(\sqrt{1+\chi}(E-\chi K)\right)\frac{dK_-}{d\tau}$$
$$=2\mu\left(\frac{2s^2}{\mu}\right)^{1/2}\frac{K}{\sqrt{1+\chi}}\frac{dK_-}{d\tau} \tag{3.71}$$

$$\frac{dK_-}{d\tau}=\frac{\epsilon}{2}\left(Z_1Z_2(z_1^2+3z_2^2)-2Z_2^2z_1z_2+\frac{4z_1^3z_2}{\mu}+\frac{4z_1z_2^3}{\mu}-\frac{2z_1^3z_2^3}{s^2}-\frac{2z_1z_2^5}{s^2}\right)+\frac{6}{8}\epsilon^2(z_1^2+z_2^2)^2z_2Z_2$$
$$=\frac{\epsilon}{2}\left(\frac{1}{3}(z_1^3z_2')'+(z_2^3z_1')'+\frac{16}{\mu}(z_1z_2^3+\frac{1}{3}z_1^3z_2)-\frac{2}{3s^2}z_1^3z_2^3-\frac{4}{s^2}z_1z_2^5-\frac{8s^2(1-\chi^2)}{\mu^2}z_1z_2\right)$$
$$+\frac{6}{8}\epsilon^2(z_1^2+z_2^2)^2z_2Z_2 \tag{3.72}$$

$$\int \frac{1}{3}(z_1^3(\tau)z_2'(\tau))'d\tau = 0 \tag{3.73}$$

$$\int (z_2^3(\tau)z_1')'d\tau = 2A_1A_2^3\Omega_1(1+\frac{\chi}{2})^3\,\mathrm{cn}'(\phi) \tag{3.74}$$

Further integrations will be more convenient if there is a change of variables

$$\Omega_1 d\tau = d\theta \tag{3.75}$$

$$\Omega_1\tau = \theta - c_2\frac{\Omega_1}{\Omega_2} \tag{3.76}$$

$$\zeta_1(\theta) = A_1\,\mathrm{cn}(\theta+\phi) \tag{3.77}$$

$$\zeta_2(\theta) = A_2\left(\left(1+\frac{\chi}{2}\right)\tanh(W\theta) - \frac{\chi}{2}W\theta\,\mathrm{sech}^2(W\theta)\right) \tag{3.78}$$

Here

$$W = \sqrt{\frac{1+\chi}{\sqrt{\frac{\mu^2}{s^2}+\chi^2}+1}} \tag{3.79}$$

$$\phi = c_1 - \frac{c_2}{W} \tag{3.80}$$

$$\int \frac{dK_-}{d\tau}d\tau = \frac{1}{\Omega_1}\int \frac{dK_-}{d\tau}d\theta = \frac{\epsilon}{2\Omega_1}\int d\theta\zeta_1\left(-\frac{8s^2\zeta_2}{\mu^2}+\frac{16\zeta_2^3}{\mu}-\frac{4\zeta_2^5}{s^2}\right) + \frac{\epsilon}{2\Omega_1}\int d\theta\zeta_1^3\left(\frac{16\zeta_2}{3\mu}-\frac{2\zeta_2^3}{3s^2}\right) \tag{3.81}$$

Let's integrate

$$\Delta I_- = \int_{\Gamma_\tau}\frac{dI_-}{d\tau}d\tau \sim \frac{2\mu K}{\sqrt{\sqrt{\frac{\mu^2}{s^2}+\chi^2}+1}\sqrt{1+\chi}}\int_{\Gamma_\theta}\frac{dK_-}{d\tau}(\theta)d\theta \tag{3.82}$$

The expression for $\frac{dK_-}{d\tau}$ contains terms proportional to ϵ and terms proportional to ϵ^2. Consider the former group of terms. Among these, there are secular terms, terms proportional to z_1 and terms proportional to z_1^3.

For the terms proportional to z_1 use the expansion of cosine amplitude cn in terms of trigonometric cosines.

$$\mathrm{cn}(u) = \frac{2\pi}{\sqrt{m}K}\sum_{n=1}^{\infty}\frac{q^{n-\frac{1}{2}}}{1+q^{2n-1}}\cos(2n-1)\frac{\pi u}{2K} \tag{3.83}$$

Note that denominator of expansion is proportional to $\sqrt{m}K$, where $m = \frac{\mu-s}{\mu+s}$ in the case of consideration. Therefore K in the denominator of cn cancels K in the numerator of $\frac{dI_-}{d\tau}$, leading to the first part of the integral

$$\begin{aligned}
\mathcal{I}_1 \;=\; & \frac{2\pi\mu\epsilon\sqrt{\frac{\mu+s}{\mu-s}}}{\sqrt{\sqrt{\frac{\mu^2}{s^2}+\chi^2}+1}\sqrt{1+\chi}}\sum_{n=1}^{\infty}\frac{q^{n-\frac{1}{2}}}{1+q^{2n-1}}\int_{\Gamma_\theta}d\theta\sum_i\cos(\omega_n(\theta+\phi))f_i(W\theta) \\
& \frac{2\pi\mu\epsilon\sqrt{\frac{\mu+s}{\mu-s}}}{\sqrt{\sqrt{\frac{\mu^2}{s^2}+\chi^2}+1}\sqrt{1+\chi}}\sum_{n=1}^{\infty}\frac{q^{n-\frac{1}{2}}}{1+q^{2n-1}}\frac{\pi s^3\sqrt{\mu^2-s^2}}{3\mu^3}\sin(\omega_n\phi)\,\mathrm{csch}\,\frac{\pi M_n}{2} \\
& \left(-48+16M_n^2+4M_n^4+\chi(-45+16M_n^2+8M_n^4)-\frac{\pi M_n\chi}{2}\coth\frac{\pi M_n}{2}\left(-45+8M_n^2+2M_n^4\right)\right) \\
& \frac{\pi\epsilon s^{\frac{7}{2}}\sqrt{\mu+s}}{3\mu^2}\sum_{n=1}^{\infty}\frac{q^{n-\frac{1}{2}}}{1+q^{2n-1}}\sin(\omega_n\phi)\,\mathrm{csch}\,\frac{\pi M_n}{2}\left(-96+32M_n^2+8M_n^4+\right. \\
& \left.\chi(-42+16M_n^2+12M_n^4)-\pi M_n\chi\coth\frac{\pi M_n}{2}\left(-45+8M_n^2+2M_n^4\right)\right)
\end{aligned} \tag{3.84}$$

$$\tag{3.85}$$

$$\tag{3.86}$$

$$M_n = \frac{(2n-1)\pi}{2KW} \tag{3.87}$$

$$\begin{aligned}
z_1(\tau) \sim \sqrt{\frac{2s^2}{\mu}\left(\sqrt{\frac{\mu^2}{s^2}+\chi^2}-1\right)}\,\mathrm{cn}\left(\sqrt{\frac{2s^2}{\mu}\left(\sqrt{\frac{\mu^2}{s^2}+\chi^2}+1\right)}\tau + c_1|\frac{\mu-s}{\mu+s}+\frac{\chi^2 s}{\mu\left(\frac{\mu}{s}+1\right)^2}\right) \\
= A_1\,\mathrm{cn}(\Omega_1\tau+c_1)
\end{aligned} \tag{3.88}$$

$$\begin{aligned}
z_2(\tau) &\sim \left(\frac{2s^2(1-\chi)}{\mu}\right)^{1/2}\mathrm{sn}\left(\left(\frac{2(1+\chi)}{\mu}\right)^{1/2}\tau + c_2|1-2\chi\right) \\
&\sim \left(\frac{2s^2(1-\chi)}{\mu}\right)^{1/2}\left(\tanh(\Theta)+\frac{\chi}{2}\left(\sinh(\Theta)\cosh(\Theta)-\Theta\right)\mathrm{sech}^2(\Theta)\right) \\
&= A_2\left((1+\frac{\chi}{2})\tanh(\Omega_2\tau+c_2)-\frac{\chi}{2}(\Omega_2\tau+c_2)\,\mathrm{sech}^2(\Omega_2\tau+c_2)\right)
\end{aligned} \tag{3.89}$$

$$I_1 = \int z_1 z_2 d\tau \sim \frac{1}{\Omega_1}\int_{-\phi}^{4K-\phi} \zeta_1(\theta)\zeta_2(\theta)d\theta = \frac{A_1A_2}{\Omega_1}\left(1+\frac{\chi}{2}\right)\int_{-\phi}^{4K-\phi} \mathrm{cn}(\theta+\phi)\tanh(W\theta)d\theta$$
$$-\frac{A_1A_2W\chi}{2\Omega_1}\int_{-\phi}^{4K-\phi} \mathrm{cn}(\theta+\phi)\ \mathrm{sech}^2(W\theta)\,\theta\,d\theta \quad (3.90)$$

Use the expansion for $\mathrm{cn}(u)$,

$$\mathrm{cn}(u) = \frac{2\pi}{kK}\sum_{n=1}^{\infty}\frac{q^{n-\frac{1}{2}}}{1+q^{2n-1}}\cos(2n-1)\frac{\pi u}{2K} \quad (3.91)$$

And set

$$\omega_n = \frac{(2n-1)\pi}{2K} \quad (3.92)$$

Assume that $\phi \sim K$, then the following approximations hold:

$$\int_{-\infty}^{\infty}\cos(\omega_n(\theta+\phi))\tanh(W\theta)\,d\theta = -\frac{\pi}{W}\,\mathrm{csch}\,\frac{\pi\omega_n}{2W}\sin\omega_n\phi \quad (3.93)$$

$$\int_{-\infty}^{\infty}\cos(\omega_n(\theta+\phi))\,\mathrm{sech}(W\theta)\,\theta\,d\theta = -\frac{\pi}{W^3}\frac{\sin(\omega_n\phi)\left(2W\sinh\frac{\pi\omega_n}{2W} - \pi\omega_n\cosh\frac{\pi\omega_n}{2W}\right)}{\cosh(\frac{\pi\omega_n}{W})-1} \quad (3.94)$$

$$(3.95)$$

$$\Delta K_- = \frac{2\sqrt{2}\epsilon\pi s^{\frac{7}{2}}(\mu+s)^{\frac{1}{2}}}{3K_1\mu^{\frac{5}{2}}}\sum_{n=1}^{\infty}\sin(\omega_n\phi)\,(\,$$
$$-\frac{3x_nC_n}{2}+\pi\,\mathrm{csch}(\frac{\pi x_n}{2})\left(C_n(x_n^2-2)(x_n^2+6)-\frac{8\pi^2(1+\frac{\mu}{s})}{K_1^2}T_n(x_n^2+6)\right)\Big) \quad (3.96)$$

and solution, corresponding to the unbound motion

$$z(\tau) = \frac{sb_2}{sn(b_2\tau + c_{2u}|\frac{a_2}{b_2})} \quad (3.97)$$

3.3 Boundaries and nodes

We shall try to use a combination of manifolds, symmetry lines and fixed points to invent invariant cells in the phase space, which are sufficient to cover the desired sub-domain of the phase space, and which does not suffer from the discontinuity problem introduced by tangencies.

3.3.1 Symmetry lines

Since all Hamiltonian systems are time reversible in the sense, described in Section 3.1.2, union of points in phase space, symmetric to themselves are called symmetry lines. They play a role.

The symmetry lines as sections are not a good idea. The reason is that, the trajectories do not have to respect the symmetry. And so there is no guarantee that all the relevant trajectories will be captured. This thinking fails in most apparent way in the example of stable and unstable manifolds of hyperbolic fixed points. In fact none of the manifolds can be properly computed using symmetry line as a section condition.

3.3.2 Stable and unstable manifolds

Manifolds play a role of invariant lines, that cut across the phase space.

Manifolds are special in their predictive quality. We can them as guides to predict locations of fixed points. In fact our numerical procedures show that when using this information can enhance convergence greatly.

3.4 Poincaré section(s)

The surface of section was designed in such a way, that this orbit should only intersect it once, i.e. it is a primitive orbit of the Poincaré map. Orbit projections are called cycles. An n-cycle has n intersections with the surface of section.

In order to capture details of trajectories, we need to capture each cyclotron oscillation of the orbit. For that purpose we use use y component of velocity as section parameter. The suitable canonical transformation is

$$\begin{cases} x^1 &= \frac{1}{\sqrt{2}}\left(-x/2 - p_y\right) - d_0 \\ p_x^1 &= \frac{1}{\sqrt{2}}\left(-y + 3p_x/2\right) \\ y^1 &= \frac{1}{\sqrt{2}}\left(-3x/2 + p_y\right) \\ p_y^1 &= \frac{1}{\sqrt{2}}\left(-y - p_x/2\right) \\ z^1 &= z^s \\ p_z^1 &= p_z^s \end{cases} \tag{3.98}$$

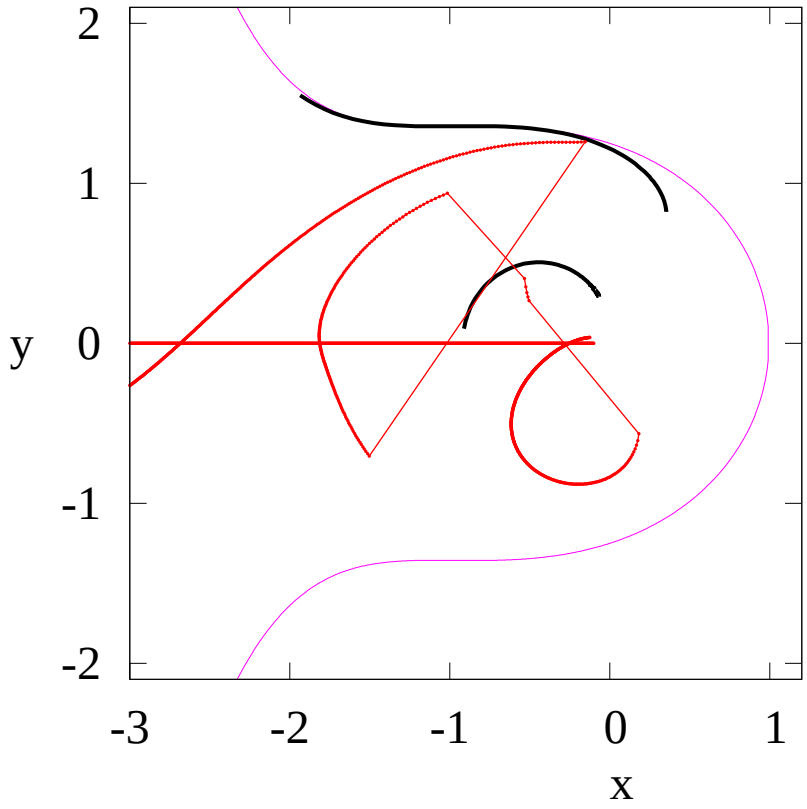


Figure 3.4: Tangecy and symmetry lines in planar crossed-fields Hamiltonian.

Section is chosen

$$\mathcal{S} : x^1 = 0 \tag{3.99}$$

and p_x^1 is eliminated using energy condition. Periodic orbits in 2d are important for understanding of 3d orbits. Periodic orbits in 2d can be derived from two (infinite) prime series of periodic orbits. Both series are σ_y symmetric. We will define each series by their in-plane stability type: Even series - with hyperbolic, odd series - with elliptic in-plane stability.

CHAPTER IV

PERIODIC ORBIT PARTITION OF THE PHASE SPACE OF THE PLANAR CROSSED-FIELDS PROBLEM

In this chapter we discuss in detail the crossed-fields Hamiltonian dynamics in 2-dof, which is obtained by setting $z(t = 0) = 0$ and $p_z(t = 0) = 0$ in Eq. (3.1) and Eq. (3.2). It follows from Eq. (3.2) that $\dot{z} = 0$ and $\dot{p}_z = 0$, therefore $z(t) \equiv 0$ and $p_z(t) \equiv 0$. The trajectories are confined to move "in the plane" and we call this system the *planar crossed-fields*. One can drop from consideration both variables in Eq. (3.1), reducing the system to a 2-dof Hamiltonian. The surface of constant energy induces nontrivial topology, as described in Section 3.1. Significance of this problem was discussed in Section 1.1. A trace of a typical

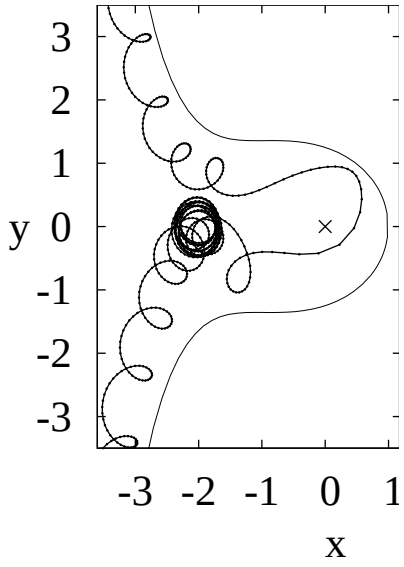


Figure 4.1: A chaotic trajectory in the crossed-fields Hamiltonian. It enters the picture from the top left corner and leaves it in the bottom left corner. Along its path transitions between asymptotic and capture regimes are clearly visible.

"hypothetical particle", in (x, y) projection, is shown in Figure 4.1. The particle enters the region from the top left corner and leaves it in the bottom left corner of the plot. As its evolution proceeds, various stages and field influences can be identified. In the $t \to \pm\infty$ limit

influence of the Coulomb potential vanishes, and dynamics is described by the magnetic field limit, discussed in Chapter 3.

Once the particle approaches the $(x = y = 0)$, influence of the Coulomb potential increases, temporarily outbalances all the other fields, gravitates the particle towards a cavity-like opening in the phase space and forces it to make one full revolution around the origin. At this point sensitivity to the initial conditions is so strong that a slight variation in the initial conditions at the entrance may easily result in the particle making two or more revolutions around the origin. Eventually the Coriolis force takes over, but before leaving into asymptotic regime, there is an interesting long-lasting "fit" near $(x, y) = (-2, 0)$ (see Figure 4.1).

This example describes general phenomena of chaotic systems, which under various circumstances and context have different physical interpretation, such as ionization in atoms (if only half of the trajectory is considered), scattering, chemical reactions, capture of asteroids etc.

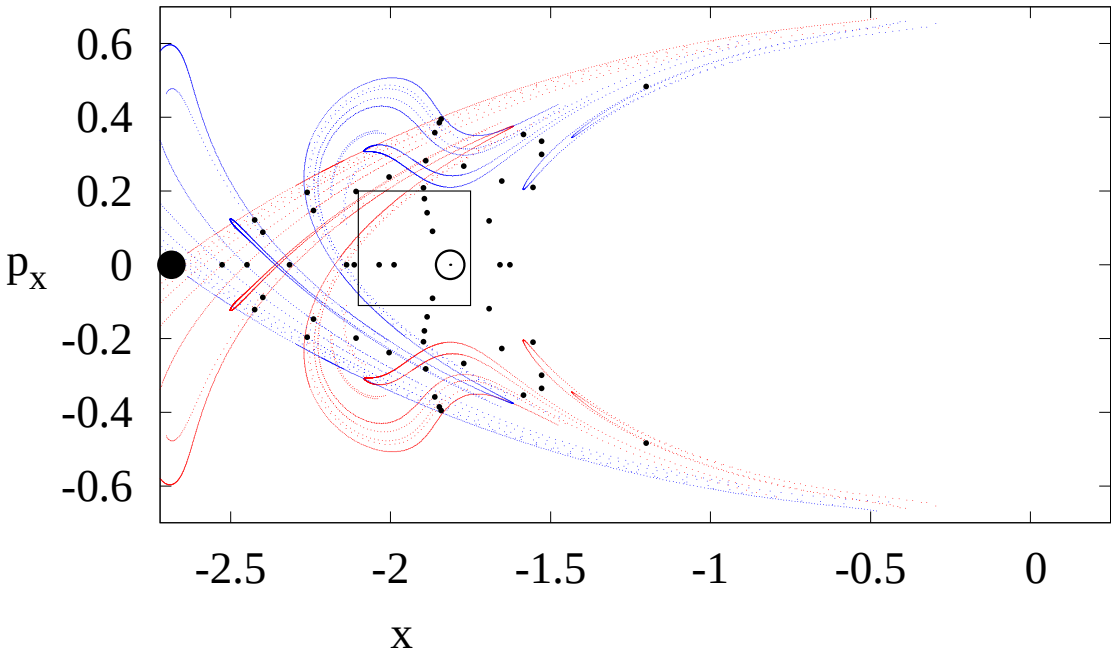


Figure 4.2: Stable and unstable manifold of a hyperbolic fixed point $p(\mathcal{O}_0)$ (solid dot). The other fixed point $p(\mathcal{O}_1)$ is indicated by a hollow dot. Unstable manifold in red, stable in blue. The discontinuities are caused by non-transversality of the surface of section.

The salient points are: a) The asymptote of the trajectory backward in time $(t \to -\infty)$

tends to (is attracted to) unstable manifold, while the asymptote of the trajectory forward in time ($t \to \infty$) is attracted to the unstable manifold of a periodic orbit $\mathcal{O}_0$. In between the two asymptotic regimes, the path of the trajectory may look completely unpredictable, and c) trajectories may get captured by hyperbolic (i.e. unstable) periodic orbits (the "fit" just before the exit.)

The principal object, governing the asymptotic behavior, turns out to be a hyperbolic periodic orbit $\mathcal{O}_0$ and its stable $W^s(\mathcal{O}_0)$ and unstable $W^u(\mathcal{O}_0)$ manifolds; it is also the same orbit that traps the trajectory in the boundary of reactive region. The projections of stable and unstable manifolds of $\mathcal{O}_0$ are shown in Figure 4.2. We will use the method of surface of section to project and study the manifolds.

4.1 Dynamical modes in terms of periodic orbits

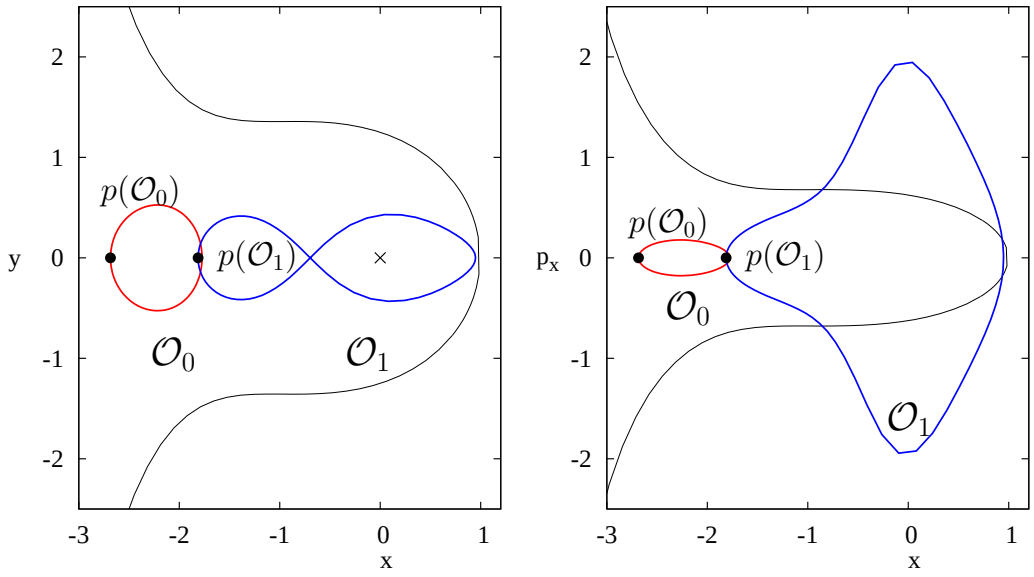


Figure 4.3: Projections of the two principal periodic orbits ($\mathcal{O}_0$ and $\mathcal{O}_1$), describing main dynamical modes of reactive trajectories in the planar crossed-fields problem. Points where orbits intersect the surface of section $\mathcal{S}$ (Eq. (3.99)) are shown as $p(\mathcal{O}_0)$ and $p(\mathcal{O}_1)$. Note that, the (x, p_x) projection of the zero velocity curve (black) does not form a boundary for the trajectories.

The stable and unstable manifolds of $p(\mathcal{O}_0)$ are shown in Figure 4.2. From this picture one can see that there should be another fixed point in between the two branches of manifolds. And indeed there is a second periodic orbit $\mathcal{O}_1$ (corresponding fixed point $p(\mathcal{O}_1)$).

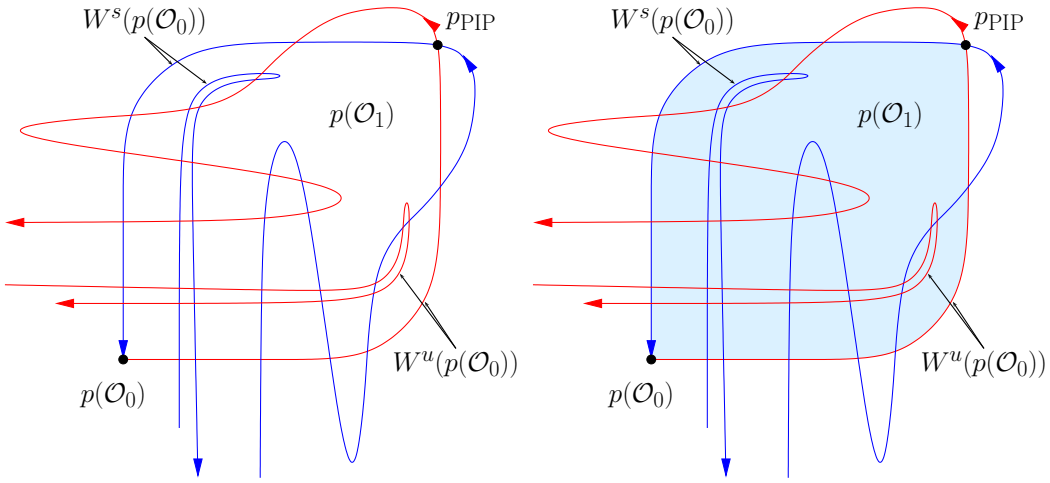


Figure 4.4: A cartoon of the homoclinic tangle generated by the orbit $\mathcal{O}_0$. Shown are half-branches of W^s and W^u which are relevant for the description of symbolic dynamics in the tangle. As a first approximation to the strange attractor, we use the area S_0 (shaded area, right panel) between two branches of W^s and W^u, joining at the *primary intersection point* $p_{\rm PIP}$. The strange attractor is contained within S_0. $p(\mathcal{O}_1)$ indicates location of the second fixed point.

The hyperbolic orbit $\mathcal{O}_0$ can be interpreted as orbit, undecided between the repulsion of electric and attraction of Coulomb forces. It is situated on top of a saddle point, originating from an equilibrium point at the critical energy $E = -2/s$. More sophisticated partition will be developed starting from these two orbits.

The intricate web formed by the manifolds W^s and W^u is called the *homoclinic tangle*. The region of the phase space, affected by the intersections of W^s and W^u, is sometimes called the "chaotic layer". The size of the chaotic layer depends on the parameters of the problem. It turns out that for our parameters, this layer is large, and therefore the importance of chaotic layer is relatively significant (see Figure 4.2).

A simplified cartoon of the homoclinic tangle is shown in the left panel of Figure 4.4. It illustrates some basic ideas about the structure of the invariant set, which we are going to construct using periodic orbits. As shown in the right panel of Figure 4.4, the starting approximation to the invariant set is the entire domain bounded by branches of W^s and W^u between the fixed point $p(\mathcal{O}_0)$ and the primary intersection point $p_{\rm PIP}$. Indeed, as shown in the first image of this area in the left panel of Figure 4.5 there is resemblance with the

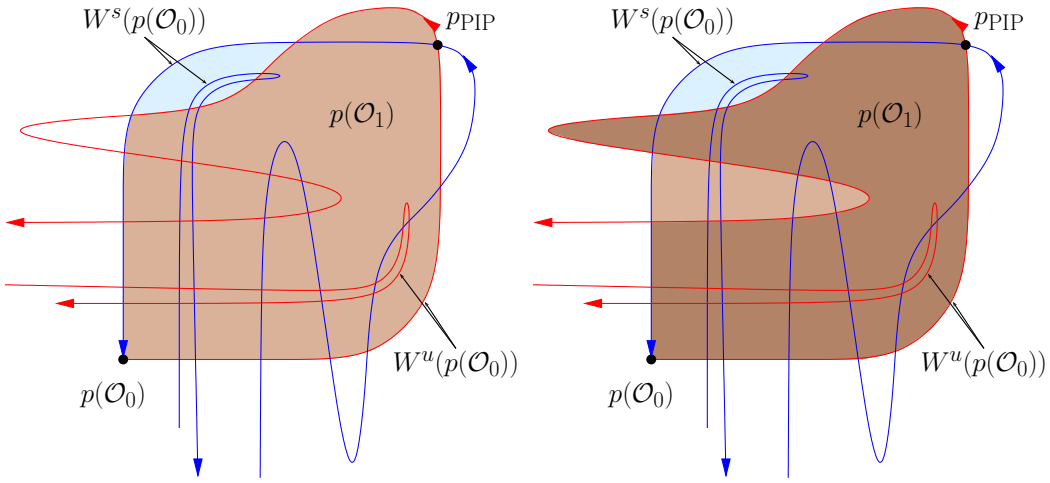


Figure 4.5: A cartoon, showing development of S_0 (see Figure 4.4). In the left panel superposed are S_0 (cyan) and $\mathcal{F}_{\mathcal{S}}(S_0)$ (brown). We can notice that the left corner of S_0 starts to stretch, and the top right corner starts to fold. We can conclude that dynamics of S_0 displays "stretch-and-fold" dynamics, which are most salient features of the Smale horseshoe. The right panel shows $\mathcal{F}_{\mathcal{S}}{}^2(S_0)$ (dark gray) superposed with $\mathcal{F}_{\mathcal{S}}(S_0)$ and S_0. We can see that more complex structures emerge, suggesting that the actual orbital dynamics is much more complicated that the Smale horseshoe. In fact we can identify regions in the new lobe that will generate a complete Smale horseshoe (see left panel of Figure 4.6).

Smale horseshoe dynamics. We can identify regions of stretching along W^u close to the point $p(\mathcal{O}_0)$ and region of folding, close to the point $p(\mathcal{O}_1)$ and p_{PIP}.

It is tempting to assume that a binary sequence could describe all trajectories. This is not so. As we can see in the right panel of Figure 4.5, the second iterate introduces another stretch-and-fold region, and complicate the structure of the invariant set. To prove that binary symbolic dynamics is not sufficient to completely describe of the invariant set I will demonstrate how to construct embedded, non-overlapping invariant sub-sets, each corresponding to a binary symbolic dynamics.

In the left panel of Figure 4.6 the shaded square S maps to a dark strip by $\mathcal{F}_{\mathcal{S}}{}^4$. The pre-images of the two strips, obtained by $S \cap \mathcal{F}_{\mathcal{S}}{}^4(S)$, intersect the dark strip. It can be shown, that this is a generic mechanism of a Smale horseshoe. The entire attractor can be obtained as an intersection of all images and all pre-images of the square S. In particular two fixed points of $\mathcal{F}_{\mathcal{S}}{}^4$ exist and are located in the intersections of $\mathcal{F}_{\mathcal{S}}{}^{-4}(S) \cup S$ and $\mathcal{F}_{\mathcal{S}}{}^4(S) \cup S$.

Our approach to constructing the attractor consists of tiling it with enough periodic

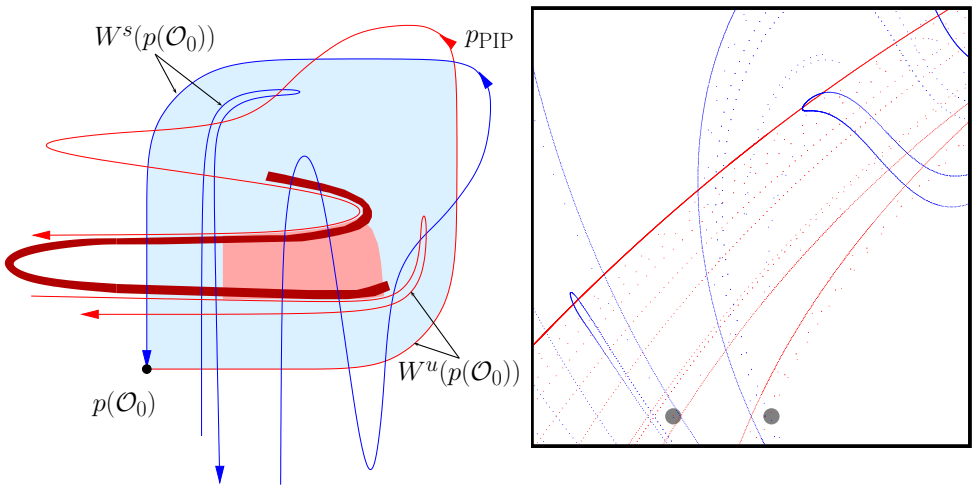


Figure 4.6: Construction of an embedded Smale horseshoe using W^s and W^u of $p(\mathcal{O}_0)$. Left panel shows cartoon, explaining the mechanism by which intersections of W^s and W^u can be used to identify location of the attractor. This information is very important from practical point of view, when we need to supply initial conditions for periodic orbit search algorithm. In the right panel, have shown calculation in the planar crossed-fields problem, Dotted lines are manifolds of $p(\mathcal{O}_0)$ (W^u red, W^s blue) and two "elementary" orbits corresponding to "stretching" (or "0") and "folding" (or "1") dynamical modes of the attractor.

orbits. If we can find all prime periodic orbits (fixed points) up to a given number of repeats. While finding simple orbits, such as the two aforementioned fixed points of ${\mathcal{F}_{\mathcal{S}}}^4$ is usually very easy in such low-dimensional systems, situation becomes significantly more complicated as longer and longer orbits have to be computed.

Together with two elementary fixed points (p_0 and p_1) we will use information about their stable and unstable manifolds W^s or W^u. Information about their linearization is contained in eigenvalues of corresponding Jacobians $D{\mathcal{F}_{\mathcal{S}}}^4(p_i)$. We have found this information sufficient to construct attractors to a high precision. Together with coordinates of fixed points p_i, we keep two vectors for each, v_i^s and v_i^u. Given two "primitive" fixed points and two vectors for each p_0 and p_1, v_0^s, v_0^u, v_1^s, v_1^u, we construct approximation to p_{10} primitive orbit by solving for the intersections $W^u(p_0) \cap W^s(p_1)$ and $W^u(p_1) \cap W^s(p_0)$ approximately.

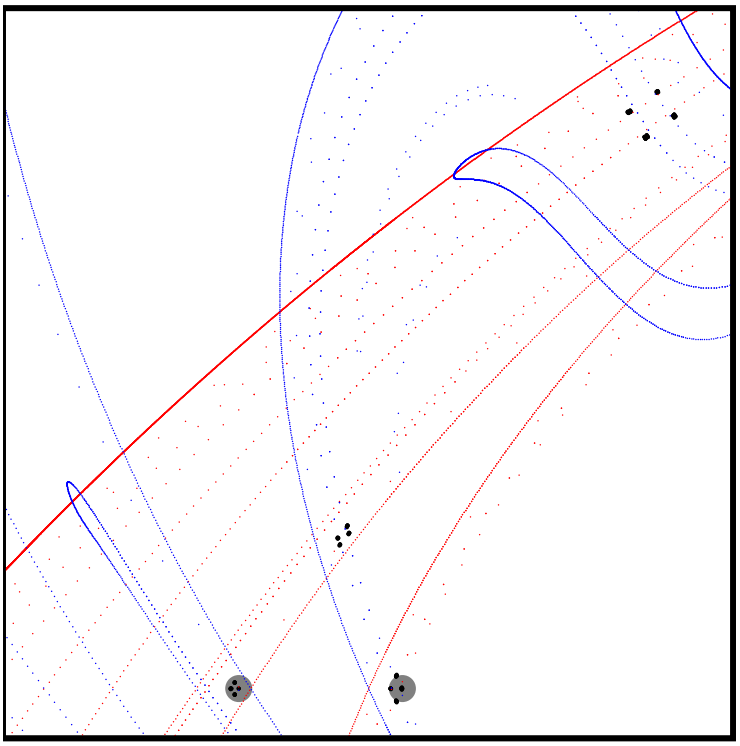


Figure 4.7: Embedded strange attractor of the planar crossed-fields problem, represented by its fixed points. All orbits with topological length have been found numerically.

Consider a set of equations for t_0, t_1, t'_0, t'_1.

$$\begin{cases} p_0 + t_0 v_0^u = p_1 + t_1 v_1^s \\ p_0 + t'_0 v_0^s = p_1 + t'_1 v_1^u \end{cases} \tag{4.1}$$

They have a unique solution if $v_0^u \wedge v_1^s \neq 0$ and $v_0^u \wedge v_1^s \neq 0$ (i.e. they are not parallel.) The two new points $p' = p_0 + t_0 v_0^u$ and $p'' = p_0 + t'_0 v_0^s$ can be used as input for the Newton's method of iterations (see Eq. (2.29)) and as linking coordinates for longer orbits. Consider an orbit

$$p_{i_0 i_1 \ldots i_{N-1}} ,$$

and construct a series of coordinates $\{q_{i_0}, \ldots, q_{i_{N-1}}\}$ by the following prescription: For each (cyclically continued if necessary) pair of adjacent i_m and i_{m+1} do: if $i_m = i_{m+1}$, then $q_{i_m} = p_{i_m}$. If $i_m \neq i_{m+1}$, then $q_{i_m} = p_{i_m} + t_{i_m} v_{i_m}^u$, where t_{i_m} solves Eq. (4.1).

The results of a calculation are displayed in the right panel of Figure 4.7, where we have zoomed in on a region of Figure 4.2, and isolated the two elementary fixed points, belonging to one such (complete) horseshoe. All periodic orbits in this attractor with length of up to 10 intersections with the surface of section have been calculated. The intersection points are displayed as dots in the Figure 4.7.

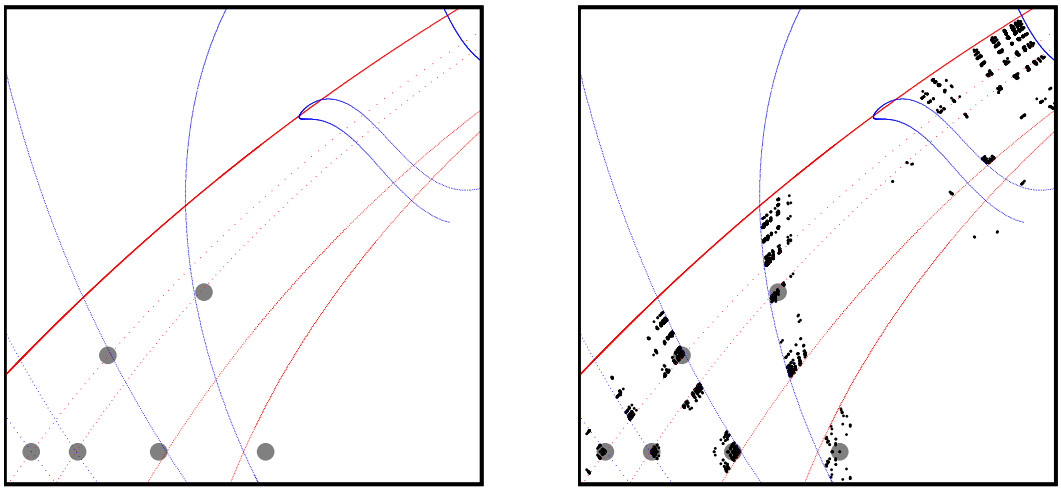


Figure 4.8: Embedded strange attractor with six symbol symbolic dynamics. Left panel: primitive orbits. Right panel: all prime orbits with up to six intersections with $\mathcal{S}$.

By the same argument, any lobe of a manifold, has infinitely many intersections with the branch of another manifold, and therefore, it is possible to construct an infinity of such horseshoes. The union of such sets, however, would strongly underestimate the size of the chaotic attractor.

Therefore, we must consider, at least at this stage a union of all the domains. The easy way is to simply gather all the prime periodic orbits, and assume that they generate a n-nary horseshoe. The issue arises where to truncate such expansion, because we have demonstrated, in principle, how to generate an infinity of primitive fixed points.

As a test of these considerations, we have assembled a complex of six periodic orbits, obtained from three horseshoes, generated following the above procedure. The orbits are shown in the left panel of Figure 4.8. The left panel shows the new elementary orbits. The

assumption is to describe a three-fold horseshoe-type attractor by means of periodic orbits (fixed points). The result of such computation is shown on the right panel of Figure 4.8, where all prime orbits with up to 6 symbols have been plotted. Our computations hint that this set is also complete. We have found all NNN prime orbits with up to 6 symbols. Normally we would expect, that the denser the coverage, the better we can control information about the phase space. Looking at the Figure 4.8, it is evident, that only a relatively small fraction of phase space that we expect to partake in transport is covered by fixed point "mesh".

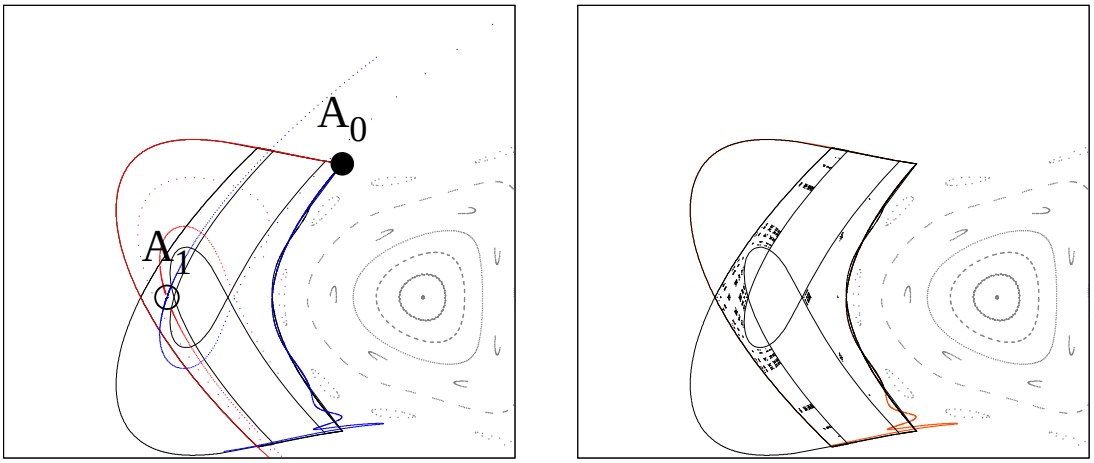


Figure 4.9: Focusing on attractor near elliptic orbit $\mathcal{O}_1$. The figure covers the area marked by a square in Figure 4.2. First we identify primitive orbits A_0 and A_1 (fixed points of ${\mathcal{F}_\mathcal{S}}^4$) and use their manifolds to identify boundaries of this attractor and the elementary cell (left panel, where first image and pre-image of the boundaries). Using methodology discussed in this Chapter and Chapter 2, we compute all prime orbits up to 10 intersections with $\mathcal{S}$. Some orbits are pruned, which can be inferred by noticing, that image/pre-image of manifolds does not completely subdivide the entire region (right panel).

A much better resolution can be achieved if a larger number of primitive fixed points is included. Our method does not require to use any specific number of primitive fixed points, and in this respect, it is universal. Results of a calculation, using 15 primitive fixed points, is displayed in Figure 4.11. Some of the shortest periodic orbits are tabulated in Table A.2.

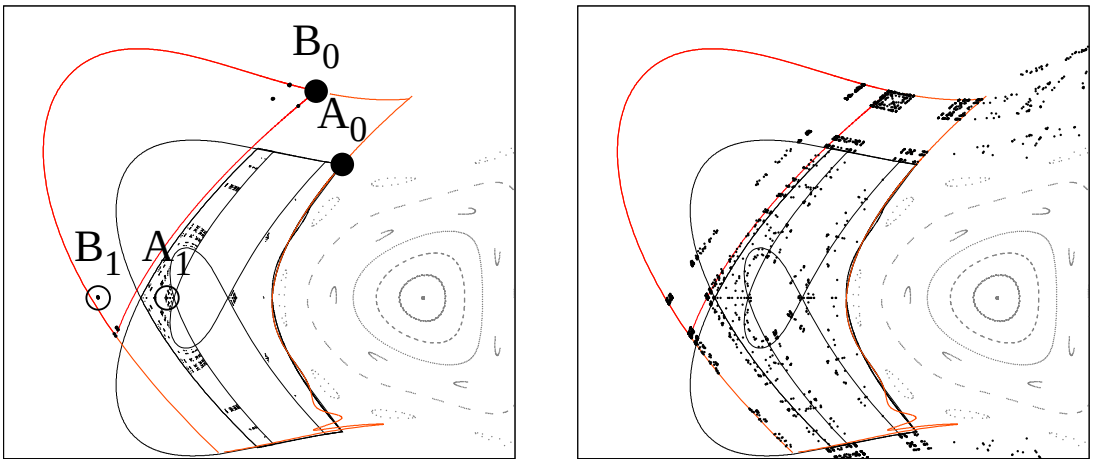


Figure 4.10: Focusing on attractor near elliptic orbit $\mathcal{O}_1$. Here, we build on results, explained in Figure 4.9 by adding two more primitive orbits B_0 and B_1 (fixed points of $\mathcal{F}_{\mathcal{S}}{}^5$. The effectiveness of methodology discussed in this Chapter and Chapter 2 is quite apparent, because computing orbits of this, more complex attractor does not pose additional complications.

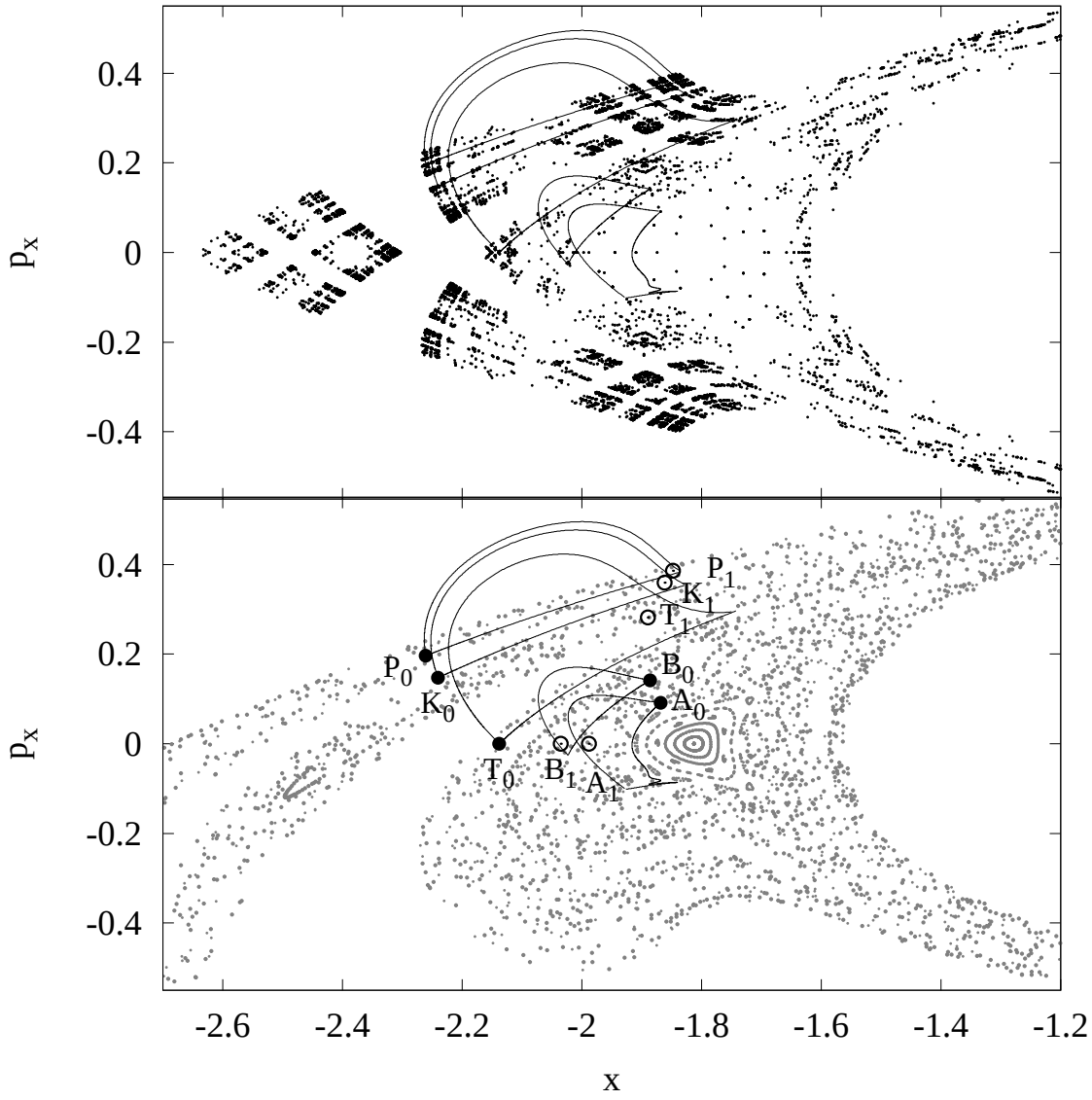


Figure 4.11: Finally, we combine all the orbits, that we consider primary, such as 15 orbits shown in the bottom panel, together with boundaries of corresponding strange attractors into one attractor (see the bottom panel), and compute periodic orbits with up to 3 intersections with $\mathcal{S}$, shown in the top panel.

CHAPTER V

NORMALLY HYPERBOLIC INVARIANT MANIFOLDS

In Chapter 4, a physical problem of ionization in atoms motivated a study of periodic orbits and how the fine details of trajectories in phase space $\mathcal{M}$ can be described by partitioning it in terms of periodic orbits. In this sense, periodic orbits were considered as building blocks, or nonlinear modes for qualitative and quantitative description of the physical problem. Motivated by extension of this problem to the 3-dof setting, we have noticed, that these concepts may be extended to include description of higher dimensional Hamiltonian systems, but the dynamical invariants, building the core of dynamics are no longer periodic orbits, but higher dimensional normally hyperbolic structures.

We will present some general and original remarks, and in Section 5.3 we present a detailed method to compute a particular family of *invariant curves*, corresponding to 2-dimensional tori in 3-dof Hamiltonian systems. The results were applied to study of trapping in molecules, presented in Chapter 7.

As it was shown, the typical scattering and ionizing trajectories are attracted to the unstable manifold (W^u) of this periodic orbit. It was shown that stable ($W^s(p)$) and unstable ($W^u(p)$) manifolds of a particular hyperbolic periodic orbit (p) intersect, and their intersections generate the strange attractor, and strange attractors are dense with fixed points (periodic orbits). Such periodic orbits can be used to quantitatively predict statistical averages of resonant, i.e. dissipative states via usage of formalism, outlined in Chapter 1.

In this way, we have outlined our main guidelines of studying chaotic systems: fundamental orbits describe coarse features of dynamics, generate relevant attractors, lastly, the attractors are described by (derivative) periodic orbits.

It was of paramount importance, that the manifolds intersect,

$$W^u(p) \cap W^s(p) \neq \varnothing$$

In Chapter 4 we studied problems reflect general situation in 2-dof Hamiltonian systems

(constrained to energy shell), where hyperbolic periodic orbits generate stable and unstable manifolds, with $\dim W^s = 2$ and $\dim W^u = 2$. Since the flow is constrained to the 3 dimensional energy shell $\mathcal{M}_E$, locally the dimension of intersection is 1 (one), by formula:

$$\dim (W^s \cup W^u) = \dim W^s + \dim W^u - \dim \mathcal{M}_E \tag{5.1}$$

In addition, the periodic orbit is a closed curve, the flow is continuous, therefore the intersection is a closed curve as well. Indeed, topological identity of intersection is a very important criterion in determining some very basic features of attractors. In a sense, if the manifolds of an invariant structure (e.g. periodic orbit) intersection is the structure of the same topology, we can expect, that there is a strange attractor, filled densely with the structures of the same dimension. In other words, in order to generate new periodic orbits, it is necessary that intersection of stable and unstable manifolds has the same dimension as the orbit.

The same argument is valid for projection of the flow on the surface of section, the periodic orbit replaced by a fixed point.

in fact what we need is

$$\dim (W^u(p) \cap W^s(p)) = \dim(p) \tag{5.2}$$

for it to be able to generate chaotic attractors.

A question arises naturally, what happens when the system has $N \geq 3$ degrees of freedom. We study some aspects of this problem, restricting to $N = 3$ and to dynamics, generated by saddle points of specific type. This study is motivated by multiple applications, and is directly related to extension of the crossed-fields problem into full three degrees of freedom, and apply the results to a problem of trapping in molecules in Chapter 7.

The general issue of symbolic dynamics in high dimensional dynamical systems is notoriously complicated, even more so when the dynamical system is Hamiltonian, and way exceeds time limits assigned to this work.

One interesting issue is the metric dimension of the attractor. Usually the rule of thumb is used, that the metric dimension is equal to $\dim W^u + 1$. In practice, quite often the

shortest chaotic orbits, $\dim W^u$ is one or a very small number even in infinite dimensional systems, such as ones studied in the context of turbulence [48]. Whenever $\dim W^u = 1$, it is considered that topological structure of an attractor is a set of embedded Smale horseshoes. We are already familiar with this situation from Chapter 4.

5.1 Normal hyperbolicity

Let K be a compact set, invariant under a map $\mathcal{F}_\mathcal{S}$, i.e.

$$\mathcal{F}_\mathcal{S} K = K. \tag{5.3}$$

We say that K is a *hyperbolic set* for $\mathcal{F}_\mathcal{S}$ if there is a continuous splitting $T_K\mathcal{S} = V^+ + V^-$ of the tangent bundle restricted to K such that

$$(T\mathcal{F}_\mathcal{S})V^- \subset V^-, \qquad (T\mathcal{F}_\mathcal{S})V^+ = V^+ \qquad \text{(invariance)}, \tag{5.4}$$

where $T\mathcal{F}_\mathcal{S}|V^\pm$ is invertible and there are $C > 0$, $\theta > 1$ with

$$\max_{x\in K} ||T\mathcal{F}_\mathcal{S}{}^{\pm n}|V^\pm|| \le C\theta^{-n} \qquad \text{for } n \ge 0.$$

Analogous mathematical definitions exist for flows and semi-flows [62].

The set K is also allowed to contain isolated fixed points $p_1, \ldots, p_N$; we require that each fixed point satisfy a hyperbolicity condition.

Unstable and stable manifolds of K are defined as forward and backward attractors in the neighborhood of K:

$$\begin{aligned}
\mathcal{V}^-_x &= \{y \in \mathcal{S} : d(\mathcal{F}_\mathcal{S}{}^n y, \mathcal{F}_\mathcal{S}{}^n x) < R \text{ for } n \ge 0\}, \\
\mathcal{V}^+_x &= \{y_0 \in \mathcal{S} : \exists (y_k)_{k\le 0} \text{ with } \mathcal{F}_\mathcal{S} y_{k-1} = y_k, \text{ and } d(y_k, \mathcal{F}_\mathcal{S}{}^k x) < R \text{ for } k \le 0\}
\end{aligned}$$

The manifolds $\mathcal{V}^\pm$ are tangent at x to $V^\pm_x$.

If $\widetilde{\mathcal{F}_\mathcal{S}}$ is C^1 close to $\mathcal{F}_\mathcal{S}$, there is a unique map $h : K \mapsto \mathcal{S}$, such that $\widetilde{\mathcal{F}_\mathcal{S}} \circ h = h \circ \mathcal{F}_\mathcal{S}$ on K. If $\widetilde{\mathcal{F}_\mathcal{S}}$ is injective on $\tilde{K} = hK$, then h is a homeomorphism and $\tilde{K}$ is a hyperbolic set for $\widetilde{\mathcal{F}_\mathcal{S}}$. The stable and unstable manifolds of $\tilde{K}$ depend continuously on $\widetilde{\mathcal{F}_\mathcal{S}}$ [62].

The above claim implies that $\mathcal{V}^\pm$ depend continuously on x and $\mathcal{V}^\pm$ depend continuously on $\mathcal{F}_\mathcal{S}$ [99].

5.2 Normally hyperbolic manifolds

The first and simplest example of hyperbolic sets is provided by K comprising of a single point – a hyperbolic fixed point $p \in \mathcal{S}$ – or a corresponding hyperbolic periodic orbit, when $\mathcal{S}$ corresponds to a surface of section. Such orbits were studied in Chapter 4.

A different example, to continue with the Hamiltonian setting, is provided by the *normally hyperbolic invariant tori*, informally also called lower dimensional tori. In d-dof Hamiltonian systems, invariant tori K_H are of dimension $\dim(T_H) \leq d$. The tori with maximal allowed dimension d (called Lagrangian tori) cannot have hyperbolic normal stability; this property is enforced by the global symplectic symmetry. Tori T_H with $\dim(T_H) < d$, however, can. Such tori in $d = 2$ systems are trivially identical to periodic orbits. The first nontrivial examples can be found in practice when $d = 3$ (see Chapter 7).

Both these examples have in common that for any $x \in K$, $\mathcal{F}_{\mathcal{S}}{}^n x$ for $n \geq 0$ will cover entire K. Whenever the internal dynamics on K is continuous, we can construct methods to compute K numerically, similar to the Newton method used to search for periodic orbits; a somewhat more complicated issue of invariant curves is discussed in Section 5.3. The essence of the former method is in fitting the parametrization of the curve so that the internal dynamics on K becomes a rigid rotation r on the circle. This is achieved by requiring that the following invariance condition holds:

$$\mathcal{F}_{\mathcal{S}} K = K \circ r \tag{5.5}$$

More complicated situation arises when discussing complex saddle in Chapter 6.

Particular cases, of a known internal dynamics have been used previously. We have implemented, and used this method extensively in this work, to compute projections of two dimensional tori. However, this method is much too restrictive. The point of the matter is that as far as dynamics *on* the manifold K is concerned, there is no reason to expect global structural stability, or knowledge-ability of internal dynamics of a given flow and given phase space.

However, the manifold as a set *can* be expected to be robust, and what is especially important, it's stable and unstable manifolds are like that, too, as was mentioned in Section 5.1.

I am not aware of constructive methods to solve (numerically) for K in general Eq. (5.3). The following section provides some ideas, but they are still on the conceptual level. They have not been tested or even implemented in this work.

The less complicated, than Eq. (5.3), is the situation that we will study in great detail in this chapter. It is concerned with properties of a normally hyperbolic set K satisfying the equation

The problem with the above approach is that internal dynamics on invariant surfaces is structurally unstable, and internal invariant structures are subject to metamorphoses as described by the KAM theory. The structural fragility is manifested in our work through problems of convergence of loops, and consequentially gaps in bifurcation diagrams. We may expect that the surface, produced by the union of all tori we have found, and some kind of interpolated surface in the gaps is an invariant surface in itself. Only because we have a wrong expectations for the parameterization of the curve (= internal dynamics), there are gaps. Therefore a method, not relying on internal parameterization is desirable.

The loop has a well defined tangent vector at each point. The tangent space is one dimensional, it is spanned by the tangent vector. The tangent vector of an invariant loop is mapped by the dynamics into a tangent vector (up to a normalization factor). This can be easily shown by considering tangent vector as difference limit (derivative of the coordinate with respect to the arc length along the loop).

Mappings of tangent vector and the loop are governed by the equation

$$x \mapsto \mathcal{F}_{\mathcal{S}}(x) \tag{5.6}$$

$$\tau(x) \mapsto D\mathcal{F}_{\mathcal{S}}(x)\tau \tag{5.7}$$

When a discretization of the loop is considered, the loop is represented by an ordered set of phase space points, assuming cyclic order:

$$\{x_i, i = 0, \ldots, N-1\} \tag{5.8}$$

The loop is assumed smooth, so that interpolation between points is effective. For the sake

of interpolation it can be considered that

$$x_0 = x_N \tag{5.9}$$

The normalized tangent at each point is a nonlinear function of the loop

$$\tau_i = \tau(x_i) = D(\{x\}; i) \tag{5.10}$$

For an example, we can use forward or symmetric approximations,

$$\tau(x_i) = \frac{x_{i+1} - x_i}{|x_{i+1} - x_i|} \tag{5.11}$$

$$\tau(x_i) = \frac{x_{i+1} - x_{i-1}}{|x_{i+1} - x_{i-1}|} \tag{5.12}$$

The equation we are going to consider can be interpreted that: tangent space must map correctly, i.e. map of the tangent space is "parallel" to the tangent space of the map. The resulting equation for a one dimensional loop reads as:

$$\tau(\mathcal{F}_{\mathcal{S}}(x)) - \lambda(x) D\mathcal{F}_{\mathcal{S}}(x)\tau(x) = 0 \tag{5.13}$$

The Jacobian in general does not preserve the length of the vector, therefore a normalization factor λ is required.

5.3 Invariant curves

We describe a method to compute two dimensional tori of the flow, by computing numerically closed invariant curves (loops) on the corresponding surface of section. This method for maps was described in [66].

We compute the invariant curves and their spectrum. Furthermore, the corresponding eigendirections are the first order approximation to the invariant manifolds (stable, unstable and central) near the curve.

This method is a concrete implementation of Eq. (5.5), namely computation of embedded invariant curves, for which the internal dynamics (dynamics on the surface) is known. When a flow is reduced to the Poincaré map $\mathcal{F}_{\mathcal{S}}$ on the surface of section $\mathcal{M}$, and the derivative of the map is obtained using formulas in Chapter 2, this method allows to compute 2-dimensional invariant tori in a 3-dof Hamiltonian system. Note that normally hyperbolic

tori can also be computed, the structure which is omnipresent in high-dimensional chaotic Hamiltonian flows, but whose detailed study has been hindered by technical difficulties [104].

We guess the type of internal dynamics to be a rotation, and attempt to parameterize the curve, respecting the internal dynamics. The curve will be parameterized as a mapping $x : \mathbb{T}^1 \mapsto \mathcal{S}$. In the numerical implementation we take torus to have length $l(\mathbb{T}^1) = 2$ (yes, two); this value was chosen in order to optimize formulas of our numerical method.

Let $\mathcal{F}_\mathcal{S}$ be a diffeomorphism of a domain $\mathcal{S} \subset \mathbb{R}^n$ ($n \geq 2$) into itself. Consider a dynamical system

$$\bar{x} = \mathcal{F}_\mathcal{S}(x) \tag{5.14}$$

We will assume that this system has an invariant curve with an irrational rotation number ω, and that there exists a (at least continuous) map $x : \mathbb{T}^1 \mapsto \mathbb{R}^n$ such that

$$\mathcal{F}_\mathcal{S}(x(\theta)) = x(\theta + \omega) \qquad \text{for all } \theta \in \mathbb{T}^1. \tag{5.15}$$

Denjoy's theorem [69, Chapter 12] states that a *rotation number* ω can be defined and that γ can be parameterized so that r is a constant shift.

In what follows we will assume that we know the rotation number $\omega \notin \mathbb{Q}$ of the invariant curve. Let $C(\mathbb{T}^1, \mathbb{R}^n)$ be the space of continuous functions from $\mathbb{T}^1$ in $\mathbb{R}^n$, and let us define the linear map $T_\omega : C(\mathbb{T}^1, \mathbb{R}^n) \mapsto C(\mathbb{T}^1, \mathbb{R}^n)$ as the translation by ω, $(T_\omega x)(\theta) = x(\theta + \omega)$. Let us define $F : C(\mathbb{T}^1, \mathbb{R}^n) \mapsto C(\mathbb{T}^1, \mathbb{R}^n)$ as

$$F(x)(\theta) = \mathcal{F}_\mathcal{S}(x(\theta)) - (T_\omega x)(\theta) \qquad \forall x \in C(\mathbb{T}^1, \mathbb{R}^n) \tag{5.16}$$

It is clear that zeros of F in $C(\mathbb{T}^1, \mathbb{R}^n)$ correspond to (continuous) invariant curves of rotation number ω.

We define the operator $T_\omega : \psi(\theta) \in C(\mathbb{T}^1, \mathbb{R}^n) \mapsto \psi(\theta+\omega) \in C(\mathbb{T}^1, \mathbb{R}^n)$ and let us consider now the following generalized eigenvalue problem: to look for pairs $(\lambda, \psi) \in \mathbb{C} \times (C(\mathbb{T}^1, \mathbb{R}^n)$ $\{0\})$ such that

$$D\mathcal{F}_\mathcal{S}(x)(\theta)\psi(\theta) = \lambda T_\omega \psi(\theta), \tag{5.17}$$

where $D\mathcal{F}_\mathcal{S}(x)$ is a differential of the map $\mathcal{F}_\mathcal{S}$ at point $x \in \mathcal{S}$. In what follows we will assume, without explicit mention, that $\omega \notin \mathbb{Q}$ (the case when $\omega \in \mathbb{Q}$ can be reduced to constant

coefficients by iterating the system a suitable number of times), and we will denote by $'$ the derivative with respect to θ.

Let $\mathcal{F}_{\mathcal{S}}$ be independent on θ explicitly in the generalized eigenvalue problem of Eq. (5.17). Then, 1 is an eigenvalue of Eq. (5.17); the corresponding eigenfunction is $x'(\theta)$. This is shown by differentiation of Eq. (5.15) with respect to θ.

Suppose that λ is an eigenvalue of Eq. (5.17). Then for any $k \in \mathbb{Z}$, $\lambda \exp(\iota k\omega)$ is also an eigenvalue of Eq. (5.17). Define $\hat{\psi}(\theta) = \exp(-\iota k\theta)\psi(\theta)$, then

$$A(\theta)\hat{\psi}(\theta) = \exp(-\iota k\theta)A(\theta)\psi(\theta) = \lambda \exp(-\iota k\theta)\psi(\theta+\omega) = \lambda \exp(\iota k\omega)T_{\omega}\hat{\psi}(\theta).$$

In particular, this shows that the closure of the set of eigenvalues of Eq. (5.17) is a union of circles with the center at the origin. If the systems is autonomous, we have shown that the closure of eigenvalues must contain the unit circle.

In dynamical systems literature, the eigenvalue problem Eq. (5.17) is frequently studied under a guise of a dynamical system, called a *skew product*:

$$\begin{cases} \bar{x} = A(\theta)x \\ \bar{\theta} = \theta + \omega \end{cases} \tag{5.18}$$

The skew product Eq. (5.18) is called reducible if there exists a (complex) change of variables $x = C(\theta)y$ such that Eq. (5.18) becomes

$$\begin{cases} \bar{y} = By \\ \bar{\theta} = \theta + \omega \end{cases} \tag{5.19}$$

where $B \equiv C^{-1}(\theta+\omega)A(\theta)C(\theta)$ does not depend on θ. The dynamics of Eq. (5.19) can be easily described by computing the eigenvalues of B. The reducibility of quasi-periodic linear systems is a well known problem in dynamical systems [10, 32, 68, 33, 34, 67, 15].

Assume that Eq. (5.18) can be reduced to Eq. (5.19) by means of transformation $x = C(\theta)y$. One can prove then, that

(a) if λ is an eigenvalue of B, then λ is an eigenvalue of Eq. (5.18);

(b) if λ is an eigenvalue of Eq. (5.18), then there exists $k \in \mathbb{Z}$ such that $\lambda \exp(\iota k\omega)$ is an eigenvalue of B.

Let us assume that λ is an eigenvalue of B, and let v be the corresponding eigenvector. Let $\psi(\theta) = C(\theta)v$. Then

$$A(\theta)\psi(\theta) = A(\theta)C(\theta)v = C(\theta+\omega)Bv = \lambda C(\theta+\omega)v = \lambda\psi(\theta+\omega) = \lambda T_\omega\psi(\theta)$$

Assume that λ is an eigenvalue of Eq. (5.17). Let $\psi(\theta)$ be the corresponding eigenfunction and let us define $\varphi(\theta) = C^{-1}(\theta)\psi(\theta)$. Then,

$$B\varphi(\theta) = BC^{-1}(\theta)\psi(\theta) = C^{-1}(\theta+\omega)A(\theta)\psi(\theta) = \lambda C^{-1}(\theta+\omega)\psi(\theta+\omega) = \lambda C^{-1}(\theta)\psi(\theta+\omega) = \lambda\varphi(\theta+\omega).$$

Without loss of generality, we can suppose that B is diagonal, $B = \text{diag}\,(\lambda_1, \ldots, \lambda_n)$. The Jordan form case can be treated in a similar way. Let us expand $\varphi(\theta)$ in Fourier series,

$$\varphi(\theta) = \sum_{k\in\mathbb{Z}} \varphi^{(k)} \exp(\iota k\theta) \qquad \varphi^{(k)} \in \mathbb{R}^n$$

One obtains

$$B\varphi^{(k)} = \lambda\varphi^{(k)} \exp(\iota k\omega)$$

As φ is not the zero function, there exists at least an index k_0 such that $\varphi^{(k_0)} \neq 0$. Let $j_0 (1 \leq j \leq n)$ be a component of $\varphi^{(k_0)}$ that is nonzero. Then, taking this component and simplifying the values $\varphi_{j_0}^{(k_0)}$ one obtains

$$\lambda_{j_0} = \lambda \exp(\iota k_0\omega)$$

that implies that λ must be of form $\lambda_{j_0} \exp(-\iota k_0\omega)$.

Two eigenvalues λ_1 and λ_2 are said to be ω-unrelated if and only if $\lambda_1 \neq \exp(\iota k\omega)\lambda_2$, $\forall k \in \mathbb{Z}$. Otherwise two such eigenvalues are called ω-related. In what follows, as the concrete value of ω will be very clear from the context, we will simply use the words "unrelated" or "related" to refer to ω-unrelated or ω-related eigenvalues.

Assume that there exist n unrelated eigenvalues $\lambda_1, \ldots, \lambda_n$ for the eigenproblem Eq. (5.15). Then equation Eq. (5.18) can be reduced to Eq. (5.19), where $B = \text{diag}\,(\lambda_1, \ldots, \lambda_2)$.

Let us call $\psi_1, \ldots, \psi_n$ the corresponding (continuous) eigenfunctions, and let us define $n \times n$ matrix $C(\theta) = (\psi_1, \ldots, \psi_n)(\theta)$. It can be shown that $C(\theta)$ defines a regular transformation that casts Eq. (5.18) into Eq. (5.19) [66].

From the above it follows that the generalized eigenvalue problem Eq. (5.17) cannot have more than n unrelated eigenvalues.

The existence of at least n unrelated eigenvalues ensures the reducibility of the system, and a reducible system cannot have more than n unrelated eigenvalues.

Therefore, for each set of n unrelated eigenvalues $\lambda_1, \ldots, \lambda_n$ of Eq. (5.17), there exits a linear transformation that brings the original system Eq. (5.18) into the reduced form Eq. (5.19), where $B = \text{diag}\,(\lambda_1, \ldots, \lambda_n)$. The modulus of these eigenvalues measures the hyperbolicity of the system and in can be immediately seen that the quantities $\log|\lambda_j|, j = 1, \ldots, n$ are the Lyapunov exponents of Eq. (5.15), so they are also the Lyapunov exponents of Eq. (5.15). The argument of the eigenvalues measures the rotation around the invariant curve and its value is defined except for multiples of ω.

5.4 Numerical implementation

We will summarize the method to solve numerically Eq. (5.15) for $F = 0$. Expand $x(\theta)$ in real Fourier series,

$$x(\theta) = a_0 + \sum_{k>0} (a_k \cos \pi k\theta + b_k \sin \pi k\theta) \qquad a_k, b_k \in \mathbb{R}^n \qquad k \in \mathbb{N}, \tag{5.20}$$

with $x(\theta)$ a 2-periodic function, i.e., $x(\theta + 2) = x(\theta)$.

Truncate the series Eq. (5.20) at a fixed value of N, and and try to determine (an approximation to) the $2N + 1$ unknown coefficients a_0, a_k, and b_k, $1 \leq k \leq N$.

We construct the discretized version of the Eq. (5.15) as follows: first, select the mesh of $2N + 1$ points on $\mathbb{T}^1$ (throughout we assume that the length of $\mathbb{T}^1 is 2$)

$$\theta_j = \frac{2j}{2N+1} \quad 0 \leq j \leq 2N$$

Given Fourier coefficients a_k, b_k, coordinates $x(\theta_j)$ can be expressed as linear functions of the coefficients a_k, b_k, i.e. $x(\theta_j) \equiv x(\{a_k\}, \{b_k\}, j)$, given by the Eq. (5.20). Accordingly, the $\mathcal{F}_{\mathcal{S}}(x(\theta_j))$, and the Eq. (5.15) can be considered a function of the coefficients a_k, b_k:

$$F_j(\{a_k\}, \{b_k\}, \omega) = \mathcal{F}_{\mathcal{S}}(x(\{a_k\}, \{b_k\}, j)) - x(\{a_k\}, \{b_k\}, j + i(\omega)) = 0 \quad 0 \leq j \leq N\,, \tag{5.21}$$

where $i(\omega) = (2N+1)\omega/2$. The coefficients a_k, b_k will be unknowns. They are obtained by a discrete Fourier transform (DFT), defined by

$$\hat{x}_k = \sum_{j=0}^{N} z_j \exp\left(-\iota \frac{\pi j k}{N}\right) \qquad 0 \le k \le 2N\,. \tag{5.22}$$

The inverse DFT is defined by

$$z_k = \frac{1}{2N+1} \sum_{j=0}^{2N} \hat{y}_j \exp\left(+\iota \frac{\pi j k}{N}\right) \qquad 0 \le k \le 2N \tag{5.23}$$

The Fourier coefficients are given by

$$a_0 = \int_0^2 x(\theta) d\theta,\; a_j = \int_0^2 x(\theta)\cos(\pi j\theta) d\theta,\; b_j = \int_0^2 x(\theta)\sin(\pi j\theta) d\theta, \quad j \ge 1\,. \tag{5.24}$$

If only first $N+1$ a_j's and N b_j's are non zero then discrete Fourier transform is equal to the trigonometric expansion. Suppose we discretized the integrals in $2N+1$ points, by taking $\theta_k = k/N$, $d\theta = 1/N$, $x_k = x(\theta_k)$, then the coefficients go to

$$a_0 \to \frac{1}{N}\sum_{k=0}^{2N} x_k, \qquad a_j \pm \iota b_j \to \frac{1}{N}\sum_{k=0}^{2N} x_k \exp\left(\pm\iota\frac{\pi j k}{N}\right), \qquad j \ge 1$$

hence

$$a_0 = \frac{1}{N}\hat{x}_0, \quad a_j = +\frac{1}{N}\Re(\hat{x}_j), \quad b_j = -\frac{1}{N}\Im(\hat{x}_j), \quad j \ge 1 \tag{5.25}$$

where $\hat{x}_j$ is the DFT of x_k.

Each step of the Newton iteration provides corrections in terms of δa_k, δb_k. Form DFT coefficients

$$\delta\hat{x}_k = \frac{\sqrt{n}}{2}\left(\delta a_k - \iota \delta b_k\right)$$

and perform inverse DFT . The result y_k should be added to original x_k.

To apply the Newton method to solve the equation $F_N = 0$, we also need to compute explicitly the differential of F_N. This can be done by applying the chain rule to the process used to compute F_N.

Examining the spectrum of DF_N, it is evident that in many cases, the union of all eigenvalues comprises a set of circles. This is related to the reducibility of the curve.

To implement numerically results of the last section we need a procedure to approximate the solutions of the generalized eigenvalue problem Eq. (5.17). To this end, we will derive

a discrete version of this equation that will be represented by a large matrix. Then, we will compute the eigenvalues and eigenvectors of this matrix by a standard numerical procedure.

Note that while an infinite-dimensional operator does not need to have eigenvalues, a finite-dimensional matrix always has the same number of eigenvalues (counted with their eigenvalues with their multiplicity) as the dimension. Then, in principle, it would be possible for the approximate eigenvalues to have nothing to do with the true spectrum of the original operator; this will be discussed in sections 3.2 and 5.

We approximate the solution by

$$F_j(a,b,\nu) + \frac{\partial F_j}{\partial a_k}\delta a_k + \frac{\partial F_j}{\partial b_k}\delta b_k + \frac{\partial F_j}{\partial \nu}\delta\nu = 0\,,$$

where a, b, ν are some values, which are close to the solution, $a+\delta a, b+\delta b, \nu+\delta\nu$.

5.4.1 Approximation of the linear operators

The idea is to derive finite-dimensional approximations for the operators $T_{-\omega}$ and $A(\theta)$, and then to multiply the corresponding matrices.

5.4.1.1 Discretization of $A(\theta)$

We recall that the matrix $A(\theta)$ is defined $D\mathcal{F}_{\mathcal{S}}(x(\theta))$, where $x(\theta)$ is a parameterization of the invariant curve. For any $\phi(\theta) \in C(\mathbb{T}^1, \mathbb{R}^n)$, define $\psi(\theta)$, to produce the Fourier coefficients of $\psi(\theta)$. As is usual in this context, we will compute and use a truncation of this matrix, according to the truncation used for the Fourier series (see section 1.1).

The computation of the differential of the map Eq. (5.17) can be obtained by means of the chain rule: if we denote by a_k one of the Fourier coefficients on x_N, we have

$$\frac{\partial[\mathcal{F}_{\mathcal{S}}(x(\theta_j))]}{\partial a_k} = D\mathcal{F}_{\mathcal{S}}(x(\theta))\frac{\partial x(\theta)}{\partial a_k}(\theta_j)$$

where $D\mathcal{F}_{\mathcal{S}}(p)$ is the Jacobian of $\mathcal{F}_{\mathcal{S}}$ at given point $p \in \mathbb{R}^n$. Note that that $D\mathcal{F}_{\mathcal{S}}$ can be easily computed and (we recall that a_k corresponds to a cosine)

$$\frac{\partial x(\theta)}{\partial a_k}(\theta_j) = I_n \cos(k\theta_j)$$

where I_n is an identity $n \times n$ matrix. Similar formulae just with sin replacing cos for coefficients b_k. From these formulae one can assemble the full derivative matrix of Eq. (5.17),

the constituents are $(2N+1)^2$ blocks of $n \times n$ real matrices, which in turn are assembled using formulae like just above.

The differential Eq. (5.20) is trivial, since the Fourier coefficients depend linearly on the values of the function. Finally, these two matrices are multiplied to produce the discretized approximation to $A(\theta)$.

5.4.1.2 Discretization of T_ω

The rotation $\theta \mapsto \theta + \omega$, when applied to real Fourier series, can be seen as rotations of angle $k\omega$ in each subspace $\{\cos(k\theta), \sin(k\theta)\}$. The matrix in this representation is block-diagonal, with 2×2 blocks of matrices of rotation by an angle $k\omega$.

Define

$$\begin{cases} c_{ij} = \cos \pi i \theta_j = \cos(\pi ij/N), \quad 0 \le i \le 2N,\, 1 \le j \le N \\ s_{ij} = \sin \pi i \theta_j = \sin(\pi ij/N), \quad 0 \le i \le 2N,\, 1 \le j \le N \\ \tilde{c}_{ij} = \cos \pi i(\theta_j + \omega) = \cos(\pi ij/N + \pi i\omega), \quad 0 \le i \le 2N,\, 1 \le j \le N \\ \tilde{s}_{ij} = \sin \pi i(\theta_j + \omega) = \sin(\pi ij/N + \pi i\omega), \quad 0 \le i \le 2N,\, 1 \le j \le N \end{cases} \tag{5.26}$$

Note that $c_{0k} = \tilde{c}_{0k} = 1$ and $s_{0k} = \tilde{s}_{0k} = 0$. With this notation the structure of the derivative matrix

$$DF = \left(\; (J_i - \mathbf{1})/2, \quad J_i c_{i1} - \mathbf{1}\tilde{c}_{i1}, \quad J_i s_{i1} - \mathbf{1}\tilde{s}_{i1}, \quad \ldots J_i c_{iN} - \mathbf{1}\tilde{c}_{iN}, \quad J_i s_{iN} - \mathbf{1}\tilde{s}_{iN} \; \right), \tag{5.27}$$

In order to be able to vary the rotation number ν, we need derivative $\frac{\partial F(x_i)}{\partial \nu}$.

$$\frac{\partial F(x_i)}{\partial \nu} = -\frac{\partial x(\theta_i + \nu)}{\partial \theta} = -\pi \sum_{j=1}^{n-1} (j b_j \cos \pi j(\theta_i + \nu) - j a_j \sin \pi j(\theta_i + \nu)) \tag{5.28}$$

5.5 Accuracy of the eigenvalues

Let $\{\lambda_j\}_{j=1}^m$ be the eigenvalues of the m-dimensional discretization of $T_{-\omega} \circ A(\theta)$, and let $\{v_j\}_{j=1}^m$ be the corresponding eigenvectors. To simplify the discussion, let us assume that Eq. (5.17) is reducible, and let μ_0 be one of the eigenvalues of the reduced matrix B. Then, the operator $T_{-\omega} \circ A(\theta)$ must have all the values $\mu_k \equiv \exp(\iota k\omega)(k \in \mathbb{Z})$ as eigenvalues. Of course, the discretized version of the operator only contains a finite number of those

values and, as is usual in these situations, not all of them have the same accuracy. The reasons for these differences in precision will be made clear later on. Hence, the output of the eigenvalue computation is a (finite) sequence of approximated eigenvalues, with different errors, and without *a priori* knowledge of which eigenvalues are the most accurate. Let us assume that $\psi(\theta)$ is an eigenfunction of eigenvalue λ. In the proof of proposition 2.2 we have seen that $\exp(-\iota k\theta)\psi(\theta)$ is also an eigenfunction of eigenvalue $\lambda \exp(\iota k\omega)$. Moreover, if $\psi(\theta) = \sum_j \psi_j \exp(\iota j\theta)$, let us also assume that the norm

$$||\psi||^{(p)} = \sum_j |\psi_j||j|^p$$

is well defined form some $p \in \mathbb{N}$. Norms like this are associated with function spaces with different degree of differentiability. The important point here is that these norms are easy to compute if we know the Fourier coefficients of ψ, and that they are unbounded when $|k|$ goes to infinity. We will use this last property to detect the most accurate eigenfunctions. The basic idea is the following: as we are truncating the Fourier series at a given order, say N, the truncation error can be measured by

$$TE(\psi, N) = \sum_{|j|>N} |\psi_j||j|^p. \tag{5.29}$$

It is clear that if we consider an eigenfunction such as $\exp(-\iota k\theta)\psi(\theta)$, expressions, such as Eq. (5.29) can only be small for a reduced set of values of $|k|$. So , these eigenfunctions can be better approximated by our discretization. Note that the eigenfunction that make small $TE(\psi, N)$, also make $||\psi||^{(p)}$ small. Therefore, after computing the eigenvectors for the discretized problem, we can compute the norms $||\cdot||^{(p)}$ for each of them and select those with the smallest norm, since they should be the more accurate ones. In practice, we found that norms with $p = 1$ are adequate for our purposes.

5.5.1 Hyperbolic directions

The hyperbolicity is easily seen since then eigenvalues of norm different from 1 appear. Let us focus first on the case in which there are eigenvalues with zero imaginary part. In this situation, only one of the eigenvalues of each equivalence class is real. The corresponding

(real) eigenfunctions span linear subspaces that are the stable or unstable manifolds of the origin for the system Eq. (5.16). These subspaces are also the first-order approximation to the invariant manifolds of the invariant curve whose normal behavior is represented by Eq. (5.17).

The case in which system is hyperbolic but without real eigenvalues is a situation that can appear in Hamiltonian systems with a complex saddle point. In this case the reduced matrix has four distinct complex eigenvalues, λ, λ^{-1}, $\bar{\lambda}$, $\bar{\lambda}^{-1}$. So we have to pick out a suitable value λ and test that the remaining three are also eigenvalues.

5.6 Notes concerning the implementation

With the previous definitions it is clear that if $x(\theta)$ is a Fourier series corresponding to an invariant curve then, for any $\varphi \in \mathbb{T}^1$, $y(\theta) \equiv x(\theta + \varphi)$ is a different Fourier series corresponding to the same invariant curve as $x(\theta)$. This implies that the differential of the function F around the invariant curve will have, at least, a one-dimensional kernel. This introduces numerical difficulties when solving the linear system that appears in the Newton method. To solve this problem we use the Singular Value Decomposition.

A singularity appears as our approximation draws very close to a correct solution. There, it does not matter that oscillation frequency was fixed. If all points on the loop were shifted by the same (arbitrary) angular value, which induces (opposite) shift in Fourier coefficient pairs (a_i, b_i) - we would still have a perfectly valid solution. So it is important that the matrix we're inverting approaches singularity. There is a cure, however - prescription called SVD (Singular Value Decomposition.)

LAPACK SVD and `C++` implementation SVD takes matrix A and (In LAPACK notation) computes U, Σ and V, such that $A = U\Sigma V^{\mathrm{T}}$, where (in case of square A) U and V are orthogonal matrices, Σ is diagonal. Solution of linear set of equations $Ax = b$ very conveniently can be written as $x = V\Sigma^{-1}(U^{\mathrm{T}} \cdot b)$.

Since `C++` is our programming language of choice whereas LAPACK and BLAS libraries are implemented in `Fortran` language, we have to take into account differences in matrix storage: matrices in `C++` column index runs first which is the opposite from `Fortran` - so if

we give A to SVD solver in written in `Fortran` LAPACK, it will calculate SVD of A^{T} and return matrices,say $\tilde{U}$, $\tilde{V}$ and Σ. By quick inspection we can write the solution to the same equation $Ax = b$ in terms of what `Fortran` gave us: $x = \tilde{U}^{\mathrm{T}}\Sigma^{-1}(\tilde{V} \cdot b)$.

We note that LAPACK software package [2, 90] has open source routines for solving generalized eigenproblem Eq. (5.17). A few useful routines are listed in the table below

Routine	Description
dgesv	Generalized eigenvalue problem using LU decomposition
dgesdd	Generalized eigenvalue problem using SVD
dgemv	BLAS level 2, matrix-vector multiplication

5.7 Initial conditions

In Hamiltonian systems, tori come in families. If we define $\gamma_i(\theta; p) = p\mathbf{v}_i^L \exp(\iota\theta) + z_0$, then

$$\mathcal{F}_{\mathcal{S}}(\gamma_i(\theta; p)) = \gamma(\theta + \omega_i; p) + \mathcal{R}(\gamma(\theta; p) - z_0) \tag{5.30}$$

Existence of solutions in the full system is considered by the KAM theory.

Transport in nearly integrable Hamiltonian systems is believed to proceed along resonant zones, or "Arnold web" [3, 113, 19, 77, 119]. Two-tori seem to be good candidates to form a "backbone" of resonant zones, and two-tori with elliptic normal linear stability may be sticky, following arguments along the same general lines as in the two-dimensional case. Linear stability analysis implies the existence of two unit eigenvalues in the spectrum of the loop: One eigenvalue is oriented along the tangent of the loop, and the second is the symplectic conjugate of the first. Its existence implies continuous family of tori. More detailed analysis shows that loops can be continued but only from one irrational rotation number to another irrational. Each rational value of rotation number should destroy the invariant curve. In many instances these details are minute and we are unable to resolve them due to numerical errors. We have investigated the destruction of tori approaching some rational numbers.

By construction the Jacobian matrix has two pairs of complex uni-modular eigenvalues, ($\exp \pm\iota\omega_1$,$\exp \pm\iota\omega_2$). The inertial manifold is four dimensional, and each pair of the eigenvalues defines two invariant symplectic vector subspaces in the manifold, each of dimension

two. They are skew orthogonal with respect to each other. The action of the Jacobian induces rotations in these subspaces, with rotation numbers ω_1, and ω_2. We shall consider action of the Jacobian matrix on a two dimensional symplectic (area preserving) vector space. Action of the Jacobian is isomorphic to that of the rotation matrix

$$\mathrm{R}_\omega = \begin{pmatrix} \cos\omega & -\sin\omega \\ \sin\omega & \cos\omega \end{pmatrix}, \tag{5.31}$$

which has circles centered at the origin as invariant surfaces. The representation of the Jacobian in particular coordinate system maps the circle into an ellipse. In general, a two dimensional matrix J with determinant one, and eigenvalues $\exp \pm\iota\omega$ in coordinates can be written as

$$\mathrm{J} = \begin{pmatrix} \cos\omega + q\sin\omega & -Q(1+q^2)\sin\omega \\ \sin\omega/Q & \cos\omega - q\sin\omega \end{pmatrix} \tag{5.32}$$

As is it maps real plane into real plane, $\mathrm{J} : \mathbb{R}^2 \mapsto \mathbb{R}^2$, but we can make it act on complex vector space $\mathbb{C}$, by identifying $\mathbb{R}^2$ with $\mathbb{C}$. Any vector $\mathbf{x}$ can be written in arbitrary basis $\{\mathbf{v}^i\}$ as $\mathbf{x} = \sum_m \mathbf{v}^i x_m$, where $x_m = \langle \mathbf{v}_m, \mathbf{x}\rangle$, where $\{\mathbf{v}_i\}$ is a set of dual vector basis, defined by $\langle \mathbf{v}_i, \mathbf{v}^j\rangle = \delta_{ij}$. Suppose that $\{\mathbf{V}^i\}$ is a set of the right eigenvectors of J, and $\{\mathbf{V}_i\}$ is a set of the left eigenvectors of J. Then, in general $\mathrm{J} = \sum_m \lambda_m \mathbf{V}^m \mathbf{V}_m$, but we apply it to $\mathbb{R}^2$, in which case we obtain $\mathrm{J} = \sum_{mn} \mathrm{R}_{\omega mn} \mathbf{V}^m \mathbf{V}_n$. Assume that we have a transformation, $\mathbf{x} \mapsto \boldsymbol{\xi} = \sum_i \mathbf{V}^i \langle \mathbf{V}_i, \mathbf{x}\rangle$. We have, that $\xi_i = \langle \mathbf{V}_i, \mathbf{x}\rangle$. We also find that $\xi'_i = \langle \mathbf{V}_i, \mathbf{x}'\rangle$, and we find that $\xi'_i = \mathrm{R}_{\omega ij}\xi_j$, namely, that this is the transformation, that maps the ellipse in the original coordinates into the "circle" coordinates, namely, we can find that J induces a map on ξ, such that $\boldsymbol{\xi} \mapsto \mathrm{R}_\omega \boldsymbol{\xi}$. The geometry of the ellipse can be determined as follows. Find eigenvector of matrix J: $\mathbf{V} = \lambda[\iota + q, Q]^{\mathrm{T}}$, where λ is arbitrary normalization factor. The real and imaginary parts of V are by definition on the invariant ellipse. Take $\lambda = \exp \iota s$, and define $\mathbf{V}'(s) + \iota\mathbf{V}''(s) = \mathbf{V}(s)$, where $\mathbf{V}'(s) = [q\cos s - \sin s, Q\cos s]^{\mathrm{T}}$, $\mathbf{V}''(s) = [\cos s + q\sin s, Q\sin s]^{\mathrm{T}}$, and look for extrema of these vectors with respect to s. We find $f(s) = |\mathbf{V}''|^2 = (Q^2+q^2)\cos^2 s + \sin^2 s + 2q\sin s\cos s$, and $|\mathbf{V}'|^2 = f(s+\pi/2)$, and $f(s+\pi) = f(s)$. We find $f_s(s) = (Q^2+q^2-1)\sin 2s + 2q\cos 2s = 0$, and $\tan 2s = 2q/[1-(Q^2+q^2)]$. The major axes are found by substituting this solution into the expression

for $f(s)$.

In this way we can find good approximations to surface of section of an invariant 2-tori and the rotation number can be estimated by calculating minimum of $\min_\omega |\mathcal{F}_\mathcal{S}(\gamma)(s) - \gamma(s+\omega)|$.

Consider a point x anywhere on the loop γ, and a point y on γ, close to x. The map $\mathcal{F}_\mathcal{S}$, maps them to points on the loop, $x \mapsto x'$, $y \mapsto y'$. Since $y - x$ is assumed small, y approximately maps to $y' \approx x' + \mathrm{J}(x)(y-x)$, where $\mathrm{J}(x) = \partial\mathcal{F}_\mathcal{S}(x)/\partial x$ is the Jacobian matrix at point x. By taking the limit $y \to x$ along the loop we conclude that tangent vector $\tau(s) = d\gamma(s)/ds$ maps to $\tau(s) \mapsto \tau'\phi_s(s)$, and $\tau' = \tau \circ \phi(s)$. The symplectic symmetry has the property that there is a row vector, $[\tau^{\mathrm{T}}\mathbb{I}]$, that maps $\tau'^{\mathrm{T}}\mathbb{I}\mathrm{J}(x(s)) = (1/\phi_s)\tau^{\mathrm{T}}\mathbb{I}$.

5.8 Constraints

To get rid of the explicit coordinate dependence, we will implement an invariant constraint, none other than the action, $\oint \mathbf{p}\, d\mathbf{q}$. In our considerations, phase space vector is stored in format as $\mathbf{x} = (x^0, x^1, x^2, x^3, \ldots) = (\mathbf{q}_0, \mathbf{p}_0, \mathbf{q}_1, \mathbf{p}_1, \ldots)$, hence the invariance condition is

$$I = \int_0^2 \sum_{\alpha=0}^{f-1} x^{2\alpha+1}\dot{x}^{2\alpha} d\theta = I_0$$

We expand the variables in Fourier basis (see Eq. (5.20)) $x(\theta) = \sum A_i f_i(\theta)$, and $\dot{x}(\theta) = \sum B_i f_i(\theta)$, where $\langle f_i f_j\rangle = \delta_{ij} d_j$. Our choice of basis functions is,

$$f(\theta) = (1/2, \cos(\pi\theta), \sin(\pi\theta), \cos(2\pi\theta), \sin(2\pi\theta), \ldots)$$

, where $A = (a_0, a_1, b_1, a_2, b_2, \ldots)$ and $B = (0, b_1\pi, -a_1\pi, 2b_2\pi, -2a_2\pi, \ldots)$, moreover $d_0 = 1/2$ and $d_{>0} = 1$, and therefore

$$I = \sum_j \sum_{\alpha=0}^{f-1} d_j A_j^{2\alpha+1} B_j^{2\alpha} = \sum_{j>0} \sum_{\alpha=0}^{f-1} \pi j \left(a_j^{2\alpha+1} b_j^{2\alpha} - b_j^{2\alpha+1} a_j^{2\alpha}\right)$$

If we wish to write down a mathematically sound formula, we can proceed by defining a vector array $\boldsymbol{\alpha}_j^\beta : \boldsymbol{\alpha}_j^\beta = (a_j^\beta, b_j^\beta)$, or $\boldsymbol{\alpha}_j = (\mathbf{a}_j, \mathbf{b}_j)$. Then the outer product of $\boldsymbol{\alpha}^\alpha \wedge \boldsymbol{\alpha}^\beta$ is what we need: $\boldsymbol{\alpha}_j^\alpha \wedge \boldsymbol{\alpha}_j^\beta = a_j^\alpha b_j^\beta - b_j^\beta a_j^\alpha$. and we can write

$$I = \sum_{j>0} \sum_{\alpha=0}^{f-1} \pi j \boldsymbol{\alpha}_j^{2\alpha+1} \wedge \boldsymbol{\alpha}_j^{2\alpha}$$

Something more ad-hoc can be used. For example, require the first "oscillatory pair" (a_1, b_1) to have a prescribed value, namely $E_1(a,b) = (|a_1|^2 + |b_1|^2)/2 \equiv E$. In this case additional constraint is:

$$a_1\delta a_1 + b_1\delta b_1 + (|a_1|^2 + |b_1|^2)/2 = E$$

If we define

$$\bar{a}_k = a_k\sqrt{n}/2 = \Re(\hat{x}_k), \qquad \bar{b}_k = b_k\sqrt{n}/2 = -\Im(\hat{x}_k)$$

and multiply the equation,

$$\frac{\sqrt{n}}{2}F_j(a,b,\nu) + \frac{\partial F_j}{\partial a_k}\delta\bar{a}_k + \frac{\partial F_j}{\partial b_k}\delta\bar{b}_k + \frac{\sqrt{n}}{2}\frac{\partial F_j}{\partial \nu}\delta\nu = 0$$

The Newton iteration is performed with a modifications in Jacobian

$$\bar{a}_1\delta\bar{a}_1 + \bar{b}_1\delta\bar{b}_1 + (|\bar{a}_1|^2 + |\bar{b}_1|^2)/2 = 4E/n$$

and

$$\frac{\partial x(\theta_i+\nu)}{\partial\theta} = \frac{2\pi}{\sqrt{n}}\sum_{j=1}^{n-1}\left(j\bar{b}_j\cos\pi j(\theta_i+\nu) - j\bar{a}_j\sin\pi j(\theta_i+\nu)\right) .$$

CHAPTER VI

DYNAMICAL SKELETON OF A SADDLE IN CROSSED-FIELDS PROBLEM

6.1 Transformations by Lie series and structure of the linearization

Perturbation analysis is done by through a generating function $G(q,p)$, by applying

$$H' = \exp[\cdot, G]H = H + [H,G] + \frac{1}{2}[H,[H,G]] + \dots \tag{6.1}$$

And to obtain the inverse transformation it's the same formula with $-G$ instead of G.

To obtain analytic first correction to periodic point, we shift coordinate origin to saddle point $(-s,0,0,s/2,0,0)$ and expand Hamiltonian to third order:

$$H = -2/s + \frac{(p_1 - q_2/2)^2 + (p_2 + q_1/2)^2 + p_3^2}{2} - \frac{3q_1^2 - r^2}{2s^2} - \frac{q_1(5q_1^2 - 3r^2)}{2s^4} + \dots \tag{6.2}$$

There is one isolated equilibrium point, for $E = -2/s$, i.e. $\mu = s$. This energy is called "Stark" saddle point energy. This is the energy at which classical ionization becomes possible.

$$x = -s,\ y = z = p_x = 0,\ p_y = sB/2,\ p_z = 0 \tag{6.3}$$

If energy exceeds "Stark" saddle point energy ($\mu > s$), the system becomes open, making it possible for the escape from nuclear to external region through a channel in a neighborhood of a saddle point. Dynamics in this area is especially sensitive to initial conditions and hyperbolic. In the context of atomic physics this phenomenon models (chaotic) ionization. In a more general setting this system is a suitable model to investigate problems of absolutely different origins: chemical reactions and astrodynamics for it is a minimalist model to capture complicated dynamics of three degrees of freedom systems near partial saddle points.

Eigenvalues of linearization Eq. (3.3) of Eq. (3.2) around the saddle point (6.3) show that there is one pair of hyperbolic eigenvalues, $\pm\lambda_h$ (hence the name: saddle point), and

two pairs of elliptic eigenvalues $\lambda_L = \pm\iota\omega_V$, $\lambda_L = \pm\iota\omega_L$). In the linearization, vertical oscillations are decoupled from the horizontal oscillations. We obtain frequency of vertical oscillations

$$\omega_V = s^{-3/2} \tag{6.4}$$

For the remaining eigenvalues we solve eigenvalue equation,

$$\begin{bmatrix} U_1 & (-B/2)\mathbf{1} \\ (B/2)\mathbf{1} & U_2 \end{bmatrix} \begin{bmatrix} v \\ w \end{bmatrix} = \lambda \begin{bmatrix} v \\ w \end{bmatrix} \tag{6.5}$$

Where

$$U_i = \begin{bmatrix} 0 & 1 \\ u_i & 0 \end{bmatrix}, \; u_1 = 2\omega_V^2 - B^2/4, \; u_2 = -\omega_V^2 - B^2/4. \tag{6.6}$$

We have equations

$$\begin{cases} U_1 v - (B/2)w = \lambda v \\ U_2 w + (B/2)w = \lambda w \end{cases}$$

Substituting second of these into the first, we obtain

$$\left(U_2U_1 + (\lambda^2 + (B^2/4))\mathbf{1} - \lambda(U_1 + U_2)\right) v = 0$$

which yields equation

$$(\lambda^2 + 2\omega_V^2)(\lambda^2 - \omega_V^2) - \lambda^2(2\omega_V^2 - B^2) = 0$$

which expands into

$$\lambda^4 + \lambda^2(B^2 - \omega_V^2) - 2\omega_V^2 = 0 \tag{6.7}$$

which yield two conjugate pairs of solutions. We find

$$\omega_L = \left\{ \frac{\sqrt{(B^2 - \omega_V^2)^2 + 8\omega_V^4} + B^2 - \omega_V^2}{2} \right\}^{1/2} \tag{6.8}$$

$$\lambda_h = \left\{ \frac{\sqrt{(B^2 - \omega_V^2)^2 + 8\omega_V^4} - (B^2 - \omega_V^2)}{2} \right\}^{1/2} \tag{6.9}$$

If magnetic field dominates, $B/\omega_V \gg 1$, frequencies are

$$\omega_L \sim \sqrt{B^2 - \omega_V^2}, \qquad \lambda_h \sim \sqrt{2\omega_V^2}$$

In the opposite limit, $B \to 0$, we have

$$\omega_e \sim \sqrt{2\omega_V^2}, \qquad \lambda_h \sim \sqrt{2\omega_V^2}$$

The equilibrium is isolated, therefore generically crossed fields Hamiltonian does not have an equilibrium. The Stark equilibrium gives rise to a set of periodic orbits and normally hyperbolic two dimensional tori.

6.2 The foliation of a saddle by invariant curves

In suitable coordinates, the Eq. (6.2) can be cast into form

$$H = H_0 + \lambda_0 q_0 p_0 + \frac{\omega_1}{2}(q_1^2 + p_1^2) + \frac{\omega_2}{2}(q_2^2 + p_2^2) + \dots \tag{6.10}$$

Note, that the surface, defined by

$$\frac{\omega_1}{2}(q_1^2 + p_1^2) + \frac{\omega_2}{2}(q_2^2 + p_2^2) = H - H_0 \tag{6.11}$$

is invariant (disregarding the higher terms in the expansion) under the dynamics. However, any given point will not explore the entire surface. It is foliated by other dynamically invariant structures – two dimensional tori: $q_i^2 + p_i^2 = \alpha_i$, and $\alpha_1 + \alpha_2 = H - H_0$. "Poles" at $\alpha_1 = 0$ or $\alpha_2 = 0$.

Such manifold is normally hypebolic. Its stable and unstable manifolds intersect and branches of these manifolds form boundaries in phase space. It would be interesting to investigate possibility to use such manifolds to partition the phase space, in analogy with the periodic orbit partition, studied in Chapter 4. The role of periodic orbits would be replaced, perhaps, by such structures, defined by Eq. (6.11). This remains a formidable task. We have numerically investigated the foliation of this structure in invariant two dimensional tori. For initial conditions, we have used high order (10 in action) numerical normal forms using the Lie bracket formalism and and power series expansion of Hamiltonian of Eq. (3.1). Then, to compute the actual tori, we have utilized methods to solve Eq. (5.5), described in Chapter 5.

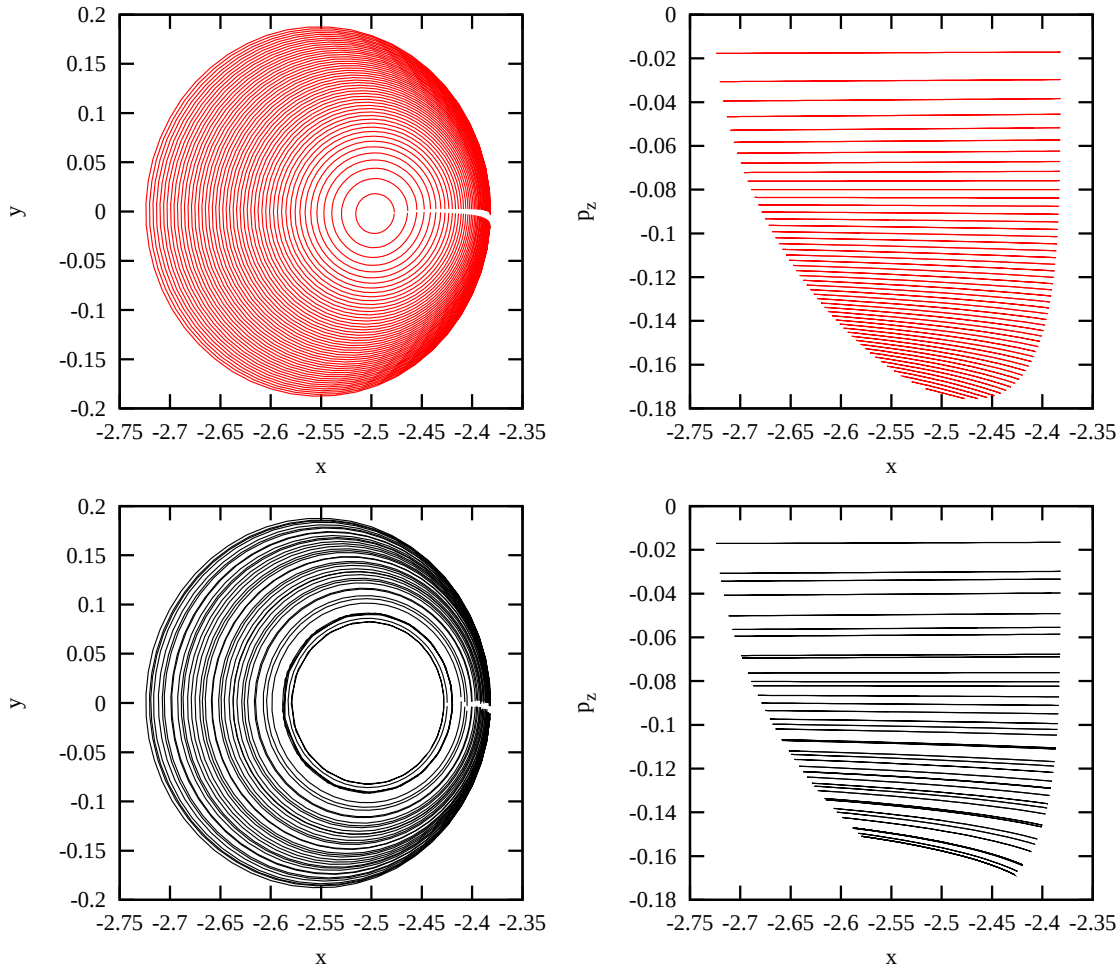


Figure 6.1: Projections to the surface of section $\mathcal{S}$ of two dimensional tori of crossed-fields Hamiltonian in 3-dof setting. The projections of two dimensional tori are one dimensional closed loops. Left panel: initial conditions, generated using high order normal forms via Lie series. Right panel: results of application of methods, described in Chapter 5. Large gaps are where the Newton method did not converge.

CHAPTER VII

CHAOS IN THE OCS MOLECULE



Figure 7.1: Space filling model of OCS molecule. In molecules, such as OCS energy flows unevenly, repeatedly going back and forth between trapping and roaming. We identify bottlenecks between diffusive and chaotic behavior, and describe generic mechanisms of these transitions, taking the carbonyl carb-sulph as a case study. The bottlenecks are found to be lower-dimensional tori; their bifurcations and unstable manifolds govern the transition mechanisms.

In this chapter we study capture of trajectories, associated to problems of anomalous diffusion, and deviations of reaction rates from predictions of statistical (RRKM) theories of uni-molecular reactions (see Section 1.2). The model of OCS molecule was chosen as a Hamiltonian that displays generic properties of 3-dof Hamiltonian systems. As such it displays features that can be found in atomic physics, molecular reactions, even dynamics of solar system or galaxies.

After introducing the Hamiltonian, its symmetries and the surface of section, we will study short periodic orbits. We will see that in order to explain the phenomenon of capture (see Figure 7.3, Figure 7.3) we have to use concepts and methods of Chapter 5. We will related this phenomenon to capture of trajectory in crossed-fields problem, as displayed in Figure 4.1, where a trajectory was captured by an unstable (hyperbolic) periodic orbit $\mathcal{O}_0$. Here, in OCS molecule, we will show the relevant phase space structures are unstable (normally hyperbolic) 2-dimensional invariant tori. Such tori are a new, little explored concept in physics.

7.1 The Hamiltonian model

The classical model of the planar (rotation-less) carbonyl sulfide OCS molecule has been studied in details in Refs. [17, 25, 28, 26, 86]. The coordinates of this system are two inter-atomic distances $R_1 = d(C,S)$, $R_2 = d(C,O)$, the bending angle of the molecule $\alpha = \widehat{OCS}$, and three momenta P_1, P_2, P_α which are canonically conjugate to R_1, R_2 and α, respectively (see Figure 7.2). We note that the third inter-atomic distance $R_3 = d(O,S)$ is expressed as a function of R_1, R_2 and α:

$$R_3 = \left(R_1^2 + R_2^2 - 2R_1R_2\cos\alpha\right)^{1/2}.$$

The Hamiltonian for this system is

$$H(R_1,R_2,\alpha,P_1,P_2,P_\alpha) = T(R_1,R_2,\alpha,P_1,P_2,P_\alpha) + V(R_1,R_2,\alpha), \tag{7.1}$$

where T and V are kinetic and potential energies, respectively. The kinetic energy T has the standard form of $\frac{\sum \overrightarrow{p_i}}{2\mu_i}$. In intrinsic coordinates it is

$$\begin{aligned} T(R_1,R_2,\alpha,P_1,P_2,P_\alpha) = {} & \frac{\mu_1 P_1^2}{2} + \frac{\mu_2 P_2^2}{2} + P_\alpha^2\left(\frac{\mu_1}{2R_1^2} + \frac{\mu_2}{2R_2^2} - \frac{\mu_3\cos\alpha}{R_1R_2}\right) \\ & + \mu_3 P_1 P_2\cos\alpha - \mu_3 P_\alpha\sin\alpha\left(\frac{P_1}{R_2} + \frac{P_2}{R_1}\right) \end{aligned} \tag{7.2}$$

where μ_i are the reduced masses. The analytic expression of the potential has been proposed based on existing experimental data [39] and can be summarized as:

$$V(R_1,R_2,\alpha) = \sum_{i=1}^{3} V_i(R_i) + V_I(R_1,R_2,R_3). \tag{7.3}$$

where $V_i(R_i)$ can be expressed in terms of Morse potentials

$$V^{\mathrm{M}}(R;\beta,R_0) = \left(1 - \exp\left[-\beta(R-R_0)\right]\right)^2 \tag{7.4}$$

$$V_i(R_i) = D_i V^{\mathrm{M}}(R_i;\beta_i,R_i^0) \tag{7.5}$$

$$V_I = P(R_1,R_2,R_3)\prod_{i=1}^{3}\left(1 - \tanh\gamma_i(R_i - R_i^0)\right), \tag{7.6}$$

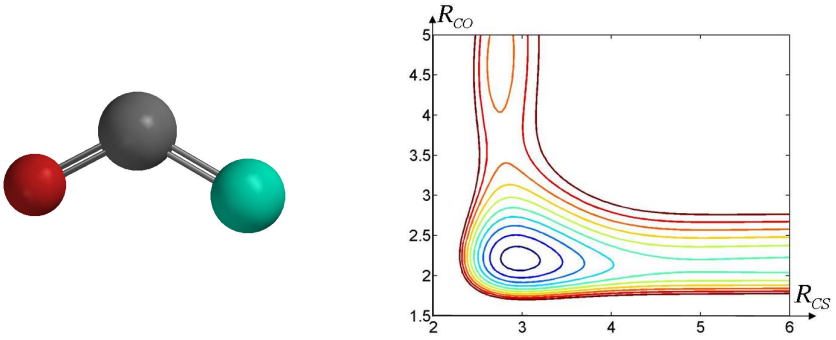


Figure 7.2: Cartoon of the OCS and equipotential surfaces of the potential V given by Eq (Eq. (7.3)) in the (R_1, R_2) plane.

The interaction potential V_I is called the Sorbie-Murrell potential, and $P(R_1, R_2, R_3)$ is a quartic polynomial in each of its variables. All the coefficients of the potential are provided in [17]. In particular, R_i^0 are the equilibrium distances of OCS in collinear ($\alpha = \pi$) configuration: $R_1^0 = 2.9508$, $R_2^0 = 2.2030$, $R_3^0 = R_1^0 + R_2^0$ (in atomic units). Contours of the potential V in collinear configuration are shown in Figure 7.2.

As a dynamical system, we first define the phase space, $\mathcal{M} \subset \mathbb{R}^5 \times \mathbb{T}$, $H(R_1, P_1, R_2, P_2, \alpha, P_\alpha) - E = 0$ parameterized by intrinsic coordinates $x = (R_1, P_1, R_2, P_2, \alpha, P_\alpha) \in \mathcal{M}$, $(R_1, P_1, R_2, P_2, P_\alpha) \in \mathbb{R}^5$, $\alpha \in \mathbb{T}$. The dynamical evolution law is defined by the differential equations, that the coordinates x satisfy. They are obtained using the standard Hamiltonian formalism from Eq. (7.1)

$$\begin{aligned} dR_i/dt &= \partial H/\partial P_i \\ d\alpha/dt &= \partial H/\partial P_\alpha \\ & \qquad i = 1, 2, \\ dP_i/dt &= -\partial H/\partial R_i \\ dP_\alpha/dt &= -\partial H/\partial \alpha \end{aligned}$$

Their explicit form is very complex and we will not write them out.

7.2 Discrete symmetries

The Hamiltonian of Eq. (7.1) has exact and approximate discrete symmetries. They can be used to facilitate the analysis of the dynamics, in particular clarify the multiplicity numbers

of orbits. The OCS Hamiltonian (Eq. (7.1)) is, quite simply "velocity square plus potential", and therefore it has high degree of symmetry, induced by the "time-reversibility". We describe the symmetry structure, exact and approximate, discussing separately angular and radial components.

Periodic orbits that are related by any of the above symmetry operations or their combinations are physically indistinguishable because their projections onto configuration space are identical. It is important to account for only one periodic orbit per family of symmetries. Its multiplicity is either 2 if the orbit is symmetric with respect to time reversal symmetry, or 4 if it is not. In order not to over-count orbits it is important to work in an energy dependent symmetry reduced cell of the surface of section, $\Omega(E)$ which guarantees, for instance, that if two fixed points in the cell are distinct, they correspond to physically distinguishable periodic orbits.

7.2.1 Angular symmetries

Time reversal symmetry, which in this case is triple (one in each degree of freedom), induces point group C_{2v} ("pmm" in crystallographic classification) on intrinsic coordinates, which act only on coordinates P_1, P_2, α and P_α, while R_1 and R_2 are left invariant. Elements of C_{2v} are e,σ_1,σ_2 and i, where elements of C_{2v} are usually referred to as identity e, reflection σ_1, reflection σ_2, inversion (rotation by 180 deg) i,

$$e(P_1, P_2, \alpha, P_\alpha) = (P_1, P_2, \alpha, P_\alpha) \tag{7.7}$$

$$\sigma_1(P_1, P_2, \alpha, P_\alpha) = (P_1, P_2, 2\pi - \alpha, -P_\alpha) \tag{7.8}$$

$$\sigma_2(P_1, P_2, \alpha, P_\alpha) = (-P_1, -P_2, 2\pi - \alpha, P_\alpha) \tag{7.9}$$

$$i(P_1, P_2, \alpha, P_\alpha) = (-P_1, -P_2, \alpha, -P_\alpha) \tag{7.10}$$

The group C_{2v} has four elements: $\dim(C_{2v}) = 4$. The cyclic of its elements properties are:

$$e^2 = i^2 = \sigma_1^2 = \sigma_2^2 = e \tag{7.11}$$

$$\sigma_1\sigma_2 = \sigma_2\sigma_1 = i. \tag{7.12}$$

We exploit the C_{2v} symmetry group to count multiplicities of trajectories and to simplify the dynamics by reducing it to a generating cell of the symmetry group.

7.2.2 Approximate radial symmetry

We discuss approximate symmetry arising from the form of potential energy, Eq. (7.3) gives rise to approximate two-fold symmetry. Eq. (7.3) can be written in the form of

$$U = D_1 V^{\mathrm{M}}(R_1; \beta_1, R_1^0) + D_2 V^{\mathrm{M}}(R_2; \beta_2, R_2^0) + V_I(R_1, R_2), \tag{7.13}$$

Using $\bar{D} = (D_1 + D_2)/2$, and $\delta D = (D_2 - D_1)/2$, we can rewrite the potential as

$$U(R_1, R_2) = U_0(R_1, R_2) + U_I(R_1, R_2), \tag{7.14}$$

$$U_0(R_1, R_2) = \bar{D} V^{\mathrm{M}}(R_1; \beta_1, R_1^0) \tag{7.15}$$

where

$$U(R_1, R_2) = \delta D \left(V^{\mathrm{M}}(R_2; \beta_2, R_2^0) - V^{\mathrm{M}}(R_1; \beta_1, R_1^0) \right) + V_I(R_1, R_2), \tag{7.16}$$

This partition is seemingly artificial, but there is something behind the scenes that it helps capture: approximate symmetry. The non-vanishing difference $\delta D = (D_2 - D_1)/2$ and the interaction potential V_I destroys the exact symmetry, produced by the identical V^{M} terms in the "unperturbed" potential. We discuss this symmetry.

With respect to linear transformations

$$L(a, b)R = aR + b, \tag{7.17}$$

Morse potentials transform as

$$V^{\mathrm{M}}(L(a, b)R; \alpha, R_0) = V^{\mathrm{M}}(R; a\alpha, (R_0 - b)/\alpha) \tag{7.18}$$

Considering a transformation on the potentials of the form

$$T(R_1, R_2) = (L(a_1, b_1)R_2, L(a_2, b_2)R_1) \tag{7.19}$$

We require that

$$U_0(T(R_1, R_2)) = U_0(R_1, R_2) \tag{7.20}$$

The requirement translates to a set of conditions on parameters

$$a_2\beta_2 = \beta_1 \quad \frac{R_2^0 - b_2}{a_2} = R_1^0$$
$$a_1\beta_1 = \beta_2 \quad \frac{R_1^0 - b_1}{a_1} = R_2^0$$

Proof of the consistency of the set of equations is the solution itself:

$$a_1 = \beta_2/\beta_1 \quad b_1 = \frac{\beta_1 R_1^0 - \beta_2 R_2^0}{/\beta_1} \tag{7.21}$$
$$a_2 = \beta_1/\beta_2 \quad b_2 = \frac{\beta_2 R_2^0 - \beta_1 R_1^0}{/\beta_2} \tag{7.22}$$

Using a single parameter $p = \beta_2/\beta_1$, the solution can be written as

$$a_1 = p \qquad b_1 = R_1^0 - pR_2^0 \tag{7.23}$$
$$a_2 = p^{-1} \quad b_2 = R_2^0 - p^{-1}R_1^0 \tag{7.24}$$

Two symmetry lines are obtained by solving $L(a_1, b_1)R_2 = R_1$ and $L(a_2, b_2)R_1 = R_2$. Two equations describe the same line, the consistency is assured by the solution 7.23. In particular, we obtain the equation for this line

$$R_2 = \frac{\beta_1}{\beta_2}(R_1 - R_1^0) + R_2^0 \tag{7.25}$$

In case of exact symmetry, the symmetry line would be a natural boundary of the elementary cell of dynamics. All orbits could be classified with respect to this symmetry as having a symmetric partner, or being self symmetric, as usually. When we do not have the exact symmetry the cell boundary argument is no longer valid, however, the orbits can still be classified in this way, in particular, with regards to their degeneracy.

7.2.3 Surface of section

A Poincaré (first return) map can be constructed as a map $\mathcal{F}_\mathcal{S} : \mathcal{S} \mapsto \mathcal{S}$, of the surface of section manifold $\mathcal{S} \subset M$ which is a codimension-one sub-manifold of M. The choice of surface of section is not unique, and the best choices should "capture all the features of the dynamical system", meaning that any trajectory should intersect the $\mathcal{S}$.

Intuition tells us, that molecule in the energy range of interest oscillates about the $(\alpha = \pi, P_\alpha = 0)$ subspace. This subspace is an invariant 2-degree of freedom subspace.

This case was studied elsewhere [28] and will be ignored in this work. Hence we can assume that it is never satisfied. Since the molecular motion in the (α, P_α) degree of freedom is libration, all trajectories pass through the inflection point (in the (α, P_α) projection), and taking $P_\alpha = 0$ will capture all the dynamics, except in the collinear sub-manifold.

We defined the Poincaré surface of section by $P_\alpha = 0$, $\dot{P}_\alpha > 0$. The important case of collinear OCS was studied elsewhere [28], therefore in this chapter we focus on three degrees of freedom dynamics.

The projection of a generating cell onto surface of section can be defined by $\alpha \in (0, \pi]$, $P_1 \geq 0$,$P_2 \in \mathbb{R}$, $P_\alpha = 0$, $\dot{P}_\alpha \geq 0$.

The method of surface of section transforms continuous time structures in six dimensional phase space into lower dimensional structures. Apart from the collinear configuration, bending motion is oscillatory and any trajectory generically crosses zero bending velocity. Therefore, by choosing $P_\alpha = 0$ for a section condition we capture all the features of dynamics. The angle of the section is a multi-valued function of the four remaining coordinates and energy, $\alpha = \alpha(R_1, P_1, R_2, P_2, P_\alpha = 0, E)$. This multivaluedness can be eliminated by fixing the elementary cell $\Omega(E)$. Thus we are left with a domain $\Omega(E)$ in a four dimensional phase space.

In order to visualize what is happening in phase space, we consider two dimensional projections of the Poincaré sections of the above trajectories, with a particular attention on the transition region.

The surface of section $\mathcal{S}$ is defined as a codimension one section of the energy manifold, such that the flow is nowhere tangent to the section. In the case of planar OCS, this section is four dimensional. A Poincaré (first return) map can be constructed as a map $\mathcal{F}_\mathcal{S} : \mathcal{S} \mapsto \mathcal{S}$. The choice of surface of section is not unique, and the best choices should "capture all the features of the dynamical system", meaning that any trajectory should intersect $\mathcal{S}$. Here, intuition tells us that the molecule in the energy range of interest oscillates about the $(\alpha = \pi, P_\alpha = 0)$ subspace. In addition, we notice that this subspace is invariant [as well as the subspace $(\alpha = 0, P_\alpha = 0)$]. The dynamics on this sub-manifold, called collinear OCS (which entails a dynamics with two degrees of freedom), was extensively studied in Refs. [28].

Since the molecular motion in the (α, P_α) degree of freedom is libration, all trajectories pass through the inflection point (in the (α, P_α) projection), and taking $P_\alpha = 0$ will capture all the dynamics, except in the collinear submanifold. We defined the Poincaré surface of section by $P_\alpha = 0$ with $\dot{P}_\alpha > 0$.

We choose a four dimensional parameterization of the surface of section $\mathcal{S}$ which consists of R_1, P_1, R_2 and P_2. Since $P_\alpha = 0$ on $\mathcal{S}$, $\alpha = f(R_1, P_1, R_2, P_2, 0; E)$ is a solution of

$$H(R_1, R_2, \alpha, P_1, P_2, 0) - E = 0, \tag{7.26}$$

such that $\dot{P}_\alpha > 0$. We solve Eq. (7.26) numerically using a Newton's method. It should be noted that if the Newton's map converges, it might not converge to a point on $\mathcal{S}$. It remains to be checked that $\dot{P}_\alpha > 0$ at this specific point. Due to the symmetries, if α is a solution $-\alpha$ is a solution (on the surface $P_\alpha = 0$). Then if the Newton's iteration ended on a point α for which $\dot{P}_\alpha < 0$, then the correct point on $\mathcal{S}$ is the same one with $-\alpha$ instead.

7.3 Observations of trapping and transitions

The "stickiness" phenomenon in dynamical systems can only be caused by marginally stable structures. In the context of this problem such structures are periodic orbits with completely elliptic linear stability. If the state of a system corresponds to a trajectory, initiated exactly on (very close to) a periodic orbit, the system will take forever (extremely long) to reach equilibrium, since the energy will remain confined on (close to) the periodic orbit. Further away, though, it is expected that, at least for a short time, the trajectory will mimic the dynamics of the periodic orbit by continuity. After this *trapping* time, the trajectory might explore a larger domain in phase space, turning *chaotic*. We focus on such trajectories. The numerical experiment is conducted as follows: First, two short periodic orbits $\mathcal{O}_a$ and $\mathcal{O}_b$ were selected , which satisfy the stability requirement in a given energy range. They are displayed in Figure 7.9 and Figure 7.9. Then initial conditions are sampled from the neighborhood of these orbits and trajectories that display trapping are investigated. The neighborhoods were chosen large enough, so that the majority of trajectories were chaotic from the start. Each trajectory was integrated for an interval of time, corresponding to 512 to 1024 intersections with the surface of section. For example if trajectory is initially

near a fixed point corresponding to $\mathcal{O}_a$ at energy $E = 0.09$ and is integrated for 1042 intersections, the total integration time can be estimated, assuming that it takes about $T_0 = 2622.68$ a. u. $= 0.0634$ ps between consecutive points of intersection. Then we have $T_{\text{total}} \approx\approx 64$ ps.

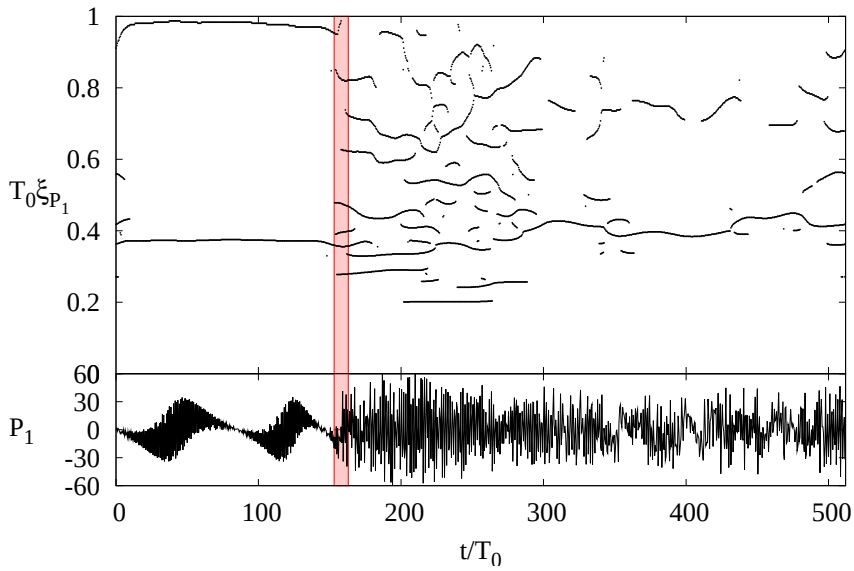


Figure 7.3: Upper panel: Time-series of one component $P_1(t)$ of a trajectory which is initially close to the periodic orbit $\mathcal{O}_a$. The energy is $E = 0.09$ a. u.. Time t is plotted in units of T_0, the period of $\mathcal{O}_a$ ($T_0 = 0.063$ ps $= 2843.88$ a. u.). The integration time is approximately $512T_0 = 34$ ps. Lower panel: Ridges of the time-frequency decomposition of $P_1(t)$. The frequencies of $P_1(t)$ are denoted ξ_{P_1}, and are represented in units of T_0^{-1}. The gray band locates the transition region.

A finite segment of any infinite trajectory can be represented mapping its coordinates at specified instances of time t_i. We found four methods of data representation useful. First three are stroboscopic representations, the fourth is surface of section representation. We assume that

> Every representation contain the same information, but naturally emphasize different features of a given segment of trajectory.

The stroboscopic representations are useful to see the instantaneous frequencies of trajectories (see time-frequency method below) and are concerned with representing trajectory data

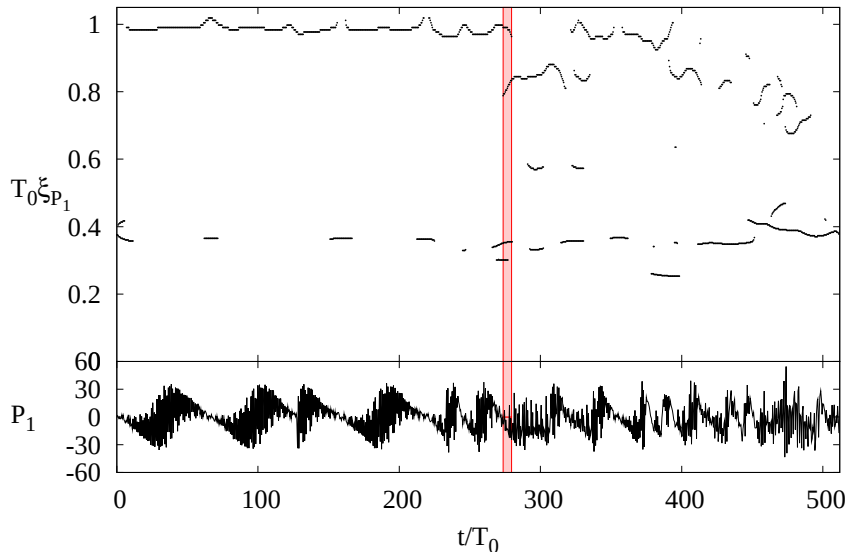


Figure 7.4: Upper panel: Time-series of one component $P_1(t)$ of a trajectory which is initially close to the periodic orbit $\mathcal{O}_a$. The energy is $E = 0.1$ a. u.. Time t is plotted in units of T_0, the period of $\mathcal{O}_a$ ($T_0 = 0.063$ ps $= 2843.88$ a. u.). The integration time is approximately $512T_0 = 34$ ps. Lower panel: Ridges of the time-frequency decomposition of $P_1(t)$. The frequencies of $P_1(t)$ are denoted ξ_{P_1}, and are represented in units of T_0^{-1}. The gray band locates the transition region.

taken at fixed intervals of time

$$x(t_i) = (R_1(t_i), P_1(t_i), R_2(t_i), P_2(t_i), \alpha(t_i), P_\alpha(t_i)), \qquad 0 \leq i < N, t_{i+1} - t_i = \Delta$$

Since we are mostly interested in low frequencies, it is adequate to take $\Delta = T/4$, where T is the period of an appropriate periodic orbit. We make an assumption that

> The dynamical features of any segment of trajectory are distributed among all degrees of freedom

Based on this assumption we claim that for the purpose of frequency analysis, it is sufficient to study one arbitrary coordinate.

The surface of section representation is useful to investigate localization and phase space structures (tori) and are concerned with representing intersections of trajectory with the surface of section

$$x(t_i) = (R_1(t_i), P_1(t_i), R_2(t_i), P_2(t_i)) \in \mathcal{S}, \qquad 0 \leq i < N, x(t_{i+1}) = \mathcal{F}_\mathcal{S}(x(t_i))$$

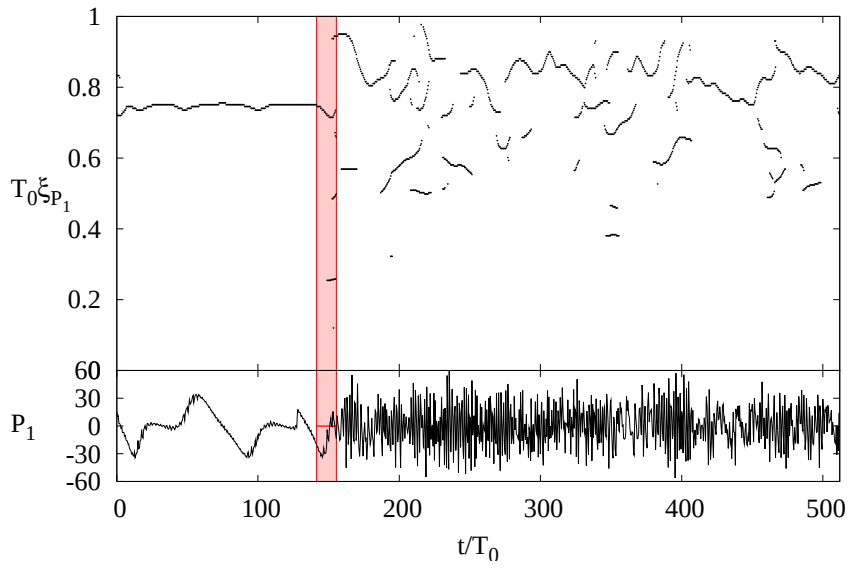


Figure 7.5: Upper panel: Time-series of one component $P_1(t)$ of a trajectory which is initially close to the periodic orbit $\mathcal{O}_e$. The energy is $E = 0.09$ a. u.. Time t is plotted in units of T_0, the period of $\mathcal{O}_a$ ($T_0 = 0.063$ ps $= 2843.88$ a. u.). The integration time is approximately $512T_0 = 34$ ps. Lower panel: Ridges of the time-frequency decomposition of $P_1(t)$. The frequencies of $P_1(t)$ are denoted ξ_{P_1}, and are represented in units of T_0^{-1}. The gray band locates the transition region.

We display sections as a pair of two dimensional plots of canonically conjugate variable pairs (R_1,P_1) and (R_2,P_2), for instance Figure 7.16. Following our assumptions we use the following representations

Time-frequency analysis of one coordinate

The time series of one coordinate

(R_1,R_2) plot of time series

Either one or both of (R_1,P_1) and (R_2,P_2) plots of section data.

Time-frequency analysis (described below) is a very useful tool to visualize and detect segments of trajectory that undergo transitions between trapping and chaos by looking at their (appropriately defined) instantaneous frequencies. See Figure 7.3, Figure 7.3, Figure 7.3, Figure 7.3.

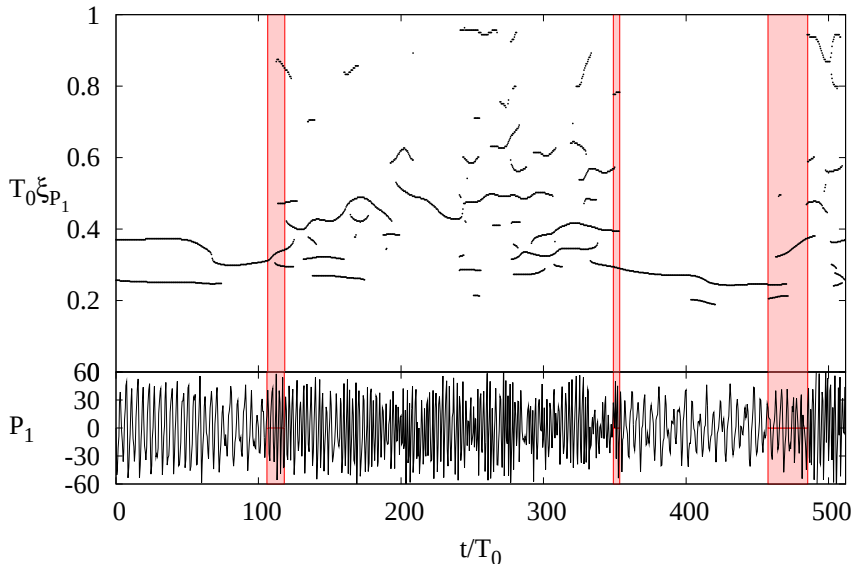


Figure 7.6: Upper panel: Time-series of one component $P_1(t)$ of a trajectory which is initially close to the periodic orbit $\mathcal{O}_e$. The energy is $E = 0.09$ a. u.. Time t is plotted in units of T_0, the period of $\mathcal{O}_a$ ($T_0 = 0.063$ ps $= 2843.88$ a. u.). The integration time is approximately $512T_0 = 34$ ps. Lower panel: Ridges of the time-frequency decomposition of $P_1(t)$. The frequencies of $P_1(t)$ are denoted ξ_{P_1}, and are represented in units of T_0^{-1}. The gray band locates the transition region.

7.3.1 Time-frequency analysis

Each trajectory is decomposed into the time-frequency plane by recording the ridges in the scalogram obtained using a wavelet decomposition [18]. More precisely, the continuous wavelet transform of an observable $f(t)$ (like for instance a coordinate of the trajectory) gives a time-scale representation of the trajectory and is given by

$$Wf(u,s) = \frac{1}{\sqrt{s}} \int_{-\infty}^{+\infty} f(t)\psi^* \left(\frac{t-u}{s}\right) dt, \tag{7.27}$$

where the mother wavelet ψ is chosen to be a Gabor (modulated Gaussian) wavelet, also called Morlet-Grossman wavelet: $\psi(t) = e^{i\eta t}e^{-t^2/2\sigma^2}/(\sigma^2\pi)^{1/4}$. The time-frequency representation is obtained by the relation between the scale s and the frequency ξ:

$$\xi = \frac{\eta}{s}. \tag{7.28}$$

We will consider the normalized scalogram

$$P_W f(u, \xi = \eta/s) = \frac{1}{s}|Wf(u,s)|^2,$$

which can be interpreted as the energy density in the time-frequency plane. The ridges of P_W can be interpreted as instantaneous frequencies, or more rigorously, the set of frequencies for a given time interval. Some striking results applying this method are displayed in Figure 7.3, 7.3, 7.3 and Figure 7.3, where $P_1(t)$ has been selected for a signal $f(t)$. From the analysis, we notice that each of these trajectories have a transition point, which has been marked by a shaded band. An interesting example is displayed in Figure 7.3, where we can observe a recapture by different structures.

7.4 Periodic orbit choreography in OCS

Many interesting features of this dynamical system can be inferred by analyzing properties of its periodic orbits. A few periodic orbits have been identified for different energy regimes in [103]. In particular, one periodic orbit ($\mathcal{O}_a$, see Figure 7.9) was singled out as important in capture processes.

We shall characterize position of the orbits by coordinates on the surface of section $\mathcal{S}$. The orbit (cycle) is characterized by $k \in \mathbb{Z}^+$, the number of times it intersects the surface of section, i.e. the smallest such k, that

$$z = {\mathcal{F}_{\mathcal{S}}}^k(z),$$

and its linear stability type. For the latter, we need two real numbers $\mathbf{s} = (s_1, s_2)$, and a symbol describing the type of orbit. Our notation for the periodic orbits is summarized in the following:

(ee) , θ_1, θ_2 Orbits are of elliptic-elliptic linear stability, two complex eigenvalues $\lambda_i = \exp(\pm\iota\theta_i)$, $i = 1, 2$

(eh) , θ, Λ Orbits are of hyperbolic-elliptic linear stability, and have a pair of real eigenvalues Λ, Λ^{-1} and a pair of complex eigenvalues $\exp \pm\iota\theta$

(hh) , Λ_1, Λ_2 Orbits are of doubly-hyperbolic linear stability and have two pairs of real eigenvalues $\Lambda_i, {\Lambda_i}^{-1}$, $i = 1, 2$

(h$*$) , Λ, θ Orbits are a co-called complex saddle, i.e. all four eigenvalues are complex and $\neq 1$ in modulus, $\Lambda_{1,2} = \Lambda \exp(\pm\iota\theta), \Lambda_{3,4} = \Lambda^{-1} \exp(\pm\iota\theta)$

Moreover, to characterize the overall degree of hyperbolicity of orbit we define a parameter S as a product of its eigenvalues with modulus > 1, i.e.

$$S = \prod_{i:|\lambda_i|\geq 1} \Lambda_i \tag{7.29}$$

We proceed to description of short periodic orbits. At low energies, we have found two $k = 1$ orbits, displayed in Figure 7.4. From the lowest energies studied, up to about $E = 0.8$, both these orbits have (ee) type.

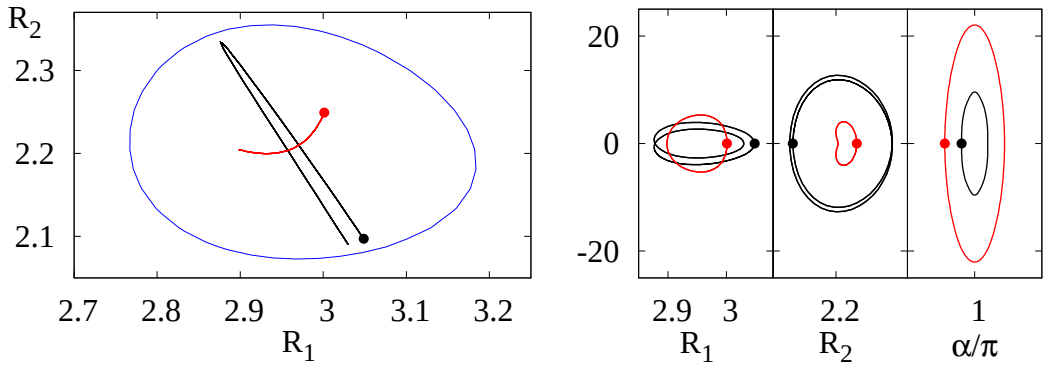


Figure 7.7: Elementary ($k = 1$) periodic orbits $\mathcal{O}_b$ (red) and $\mathcal{O}_e$ (black) at $E = 0.01$ in various projections. Together with orbit projections, fixed points of the Poincaré map are shown as thick dots. In the left panel (R_1, R_2 projection) the zero velocity curve ($T = 0$) of collinear configuration ($\alpha = \pi$) shown as blue curve.

Further metamorphoses of orbit $\mathcal{O}_b$ are displayed in Figure 7.4. Close to $E = 0.08$ In this bifurcation, it turns (eh) , and $\mathcal{O}_a$ emerges with (ee) stability. At higher energies $\mathcal{O}_a$ changes stability type several times, likely bifurcating again, however the emergent orbits have $k > 1$.

Periodic orbits play an important role by being indicators for local qualitative features of the trajectories, and they are central in understanding features of capture. In particular, the ones with shortest periods play the role of organizing centers determining qualitative features of the dynamics in their vicinity. Because of their generating properties they are referred to as "primitive" orbits.

In addition, these structures turn out to be important for the determination of other invariant structures such as higher period periodic orbits, two and three dimensional invariant tori. The period determines the local recurrence time, and the normal stability determines

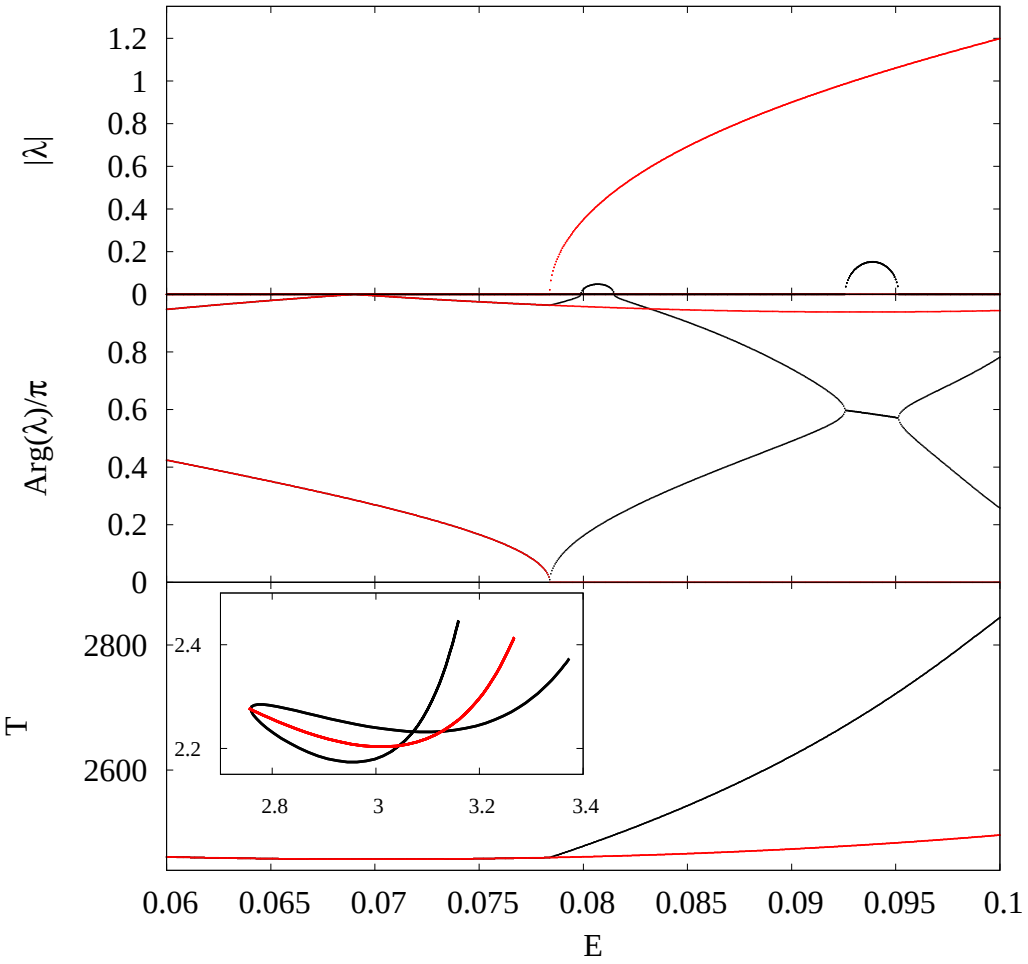


Figure 7.8: Bifurcation and stability diagram of periodic orbit $\mathcal{O}_b$. At the pitchfork bifurcation one pair of eigenvalues of $\mathcal{O}_b$ leave the unit circle along the real axis, turning $\mathcal{O}_b$ (eh) . At the bifurcation, orbit $\mathcal{O}_a$ is born with (ee) stability. This orbit has approximately double the period of $\mathcal{O}_b$, but because it has $k = 1$, it is a prime orbit of $\mathcal{F}_{\mathcal{S}}$ (see also Figure 7.9.) Inset: (R_1,R_2) projection at $E = 0.08$.

whether the dynamics in the neighborhood is rotational (elliptic stability), hyperbolic (real eigenvalues), mixed (mixtures of two previous), or complex hyperbolic (complex eigenvalues, with moduli different from one).

Periodic orbits are fixed points of the Poincaré map. Consider a fixed point equation

Solutions of this equation correspond to periodic orbits that makes k cycles in the (α, P_α) plane. Orbits with $k = 1$ will be referred to as "elementary" periodic orbits.

Add periodic orbits for low energies, $E = 0.01$, then discuss their metamorphoses as the energy of $E = 0.10$ is reached. How other orbits can be obtained using properties of

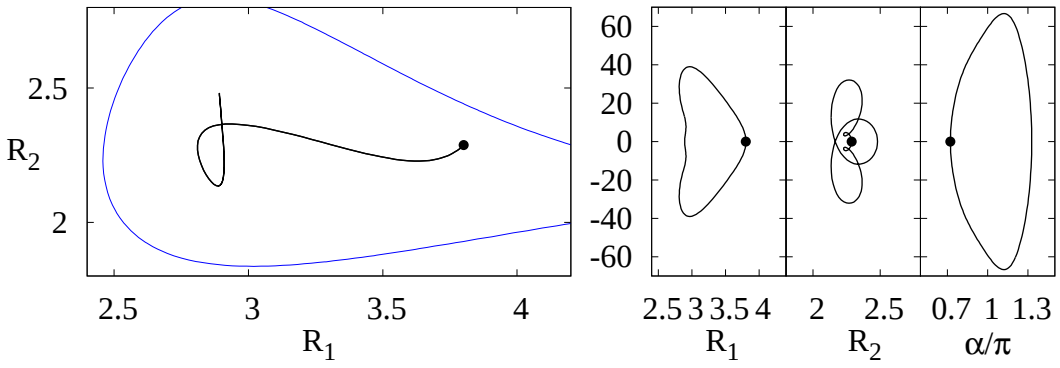


Figure 7.9: Plots of periodic orbit $\mathcal{O}_a$, at $E = 0.10$. Projections plotted (From left to right): (R_1, R_2), (R_1,P_1), (R_2, P_2), (α/π, P_α). Together with orbit projections, fixed point of the Poincaré map is shown as black dots. In the (R_1, R_2) the potential curve, corresponding to $\alpha = \pi$ and kinetic energy $T = 0$ is plotted as a blue line (see also Figure 7.4.)

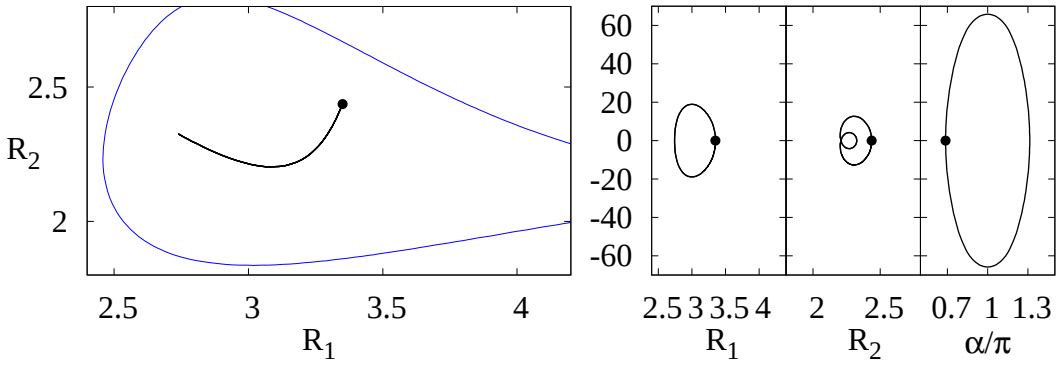


Figure 7.10: Plots of periodic orbit $\mathcal{O}_b$, at $E = 0.10$. Projections plotted (From left to right): (R_1, R_2), (R_1,P_1), (R_2, P_2), (α/π, P_α). Together with orbit projections, fixed point of the Poincaré map is shown as black dots. In the (R_1, R_2) the potential curve, corresponding to $\alpha = \pi$ and kinetic energy $T = 0$ is plotted as a blue line (see also Figure 7.4.)

elementary orbits.

Th number and properties of these orbits depend on a problem.

The first type of structure we identify are periodic orbits which constitutes the backbone of the dynamics [24].

Periodic orbit bifurcations happen as energy is varied. Usually these are (Hamiltonian) pitchfork bifurcations, resulting in "doubling" of orbit. In the section, however this does not necessarily lead to "period" doubling. In particular, the focal orbit of this chapter, $\mathcal{O}_a$ is a result of a pitchfork bifurcation of orbit $\mathcal{O}_b$, shown in Figure 7.4, however, both orbits $\mathcal{O}_a$, and $\mathcal{O}_b$ are one-return orbits in the surface of section.

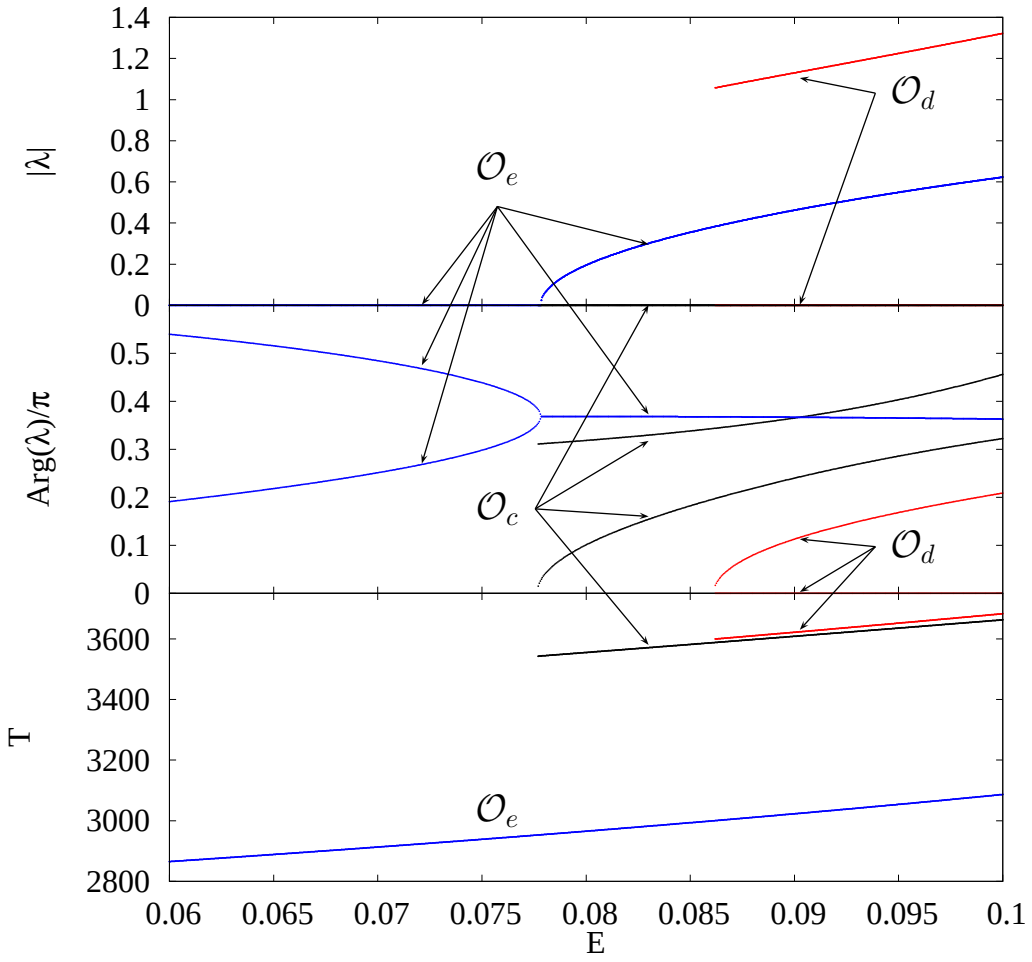


Figure 7.11: Bifurcation and stability diagram for orbits $\mathcal{O}_c$, $\mathcal{O}_d$, $\mathcal{O}_e$. All the eigenvalues are represented in this plot. If only one curve represents an orbit, then two eigenvalues are complex, and have the same argument. Otherwise, when an orbit is represented by two distinct curves, it is of type (hh) .

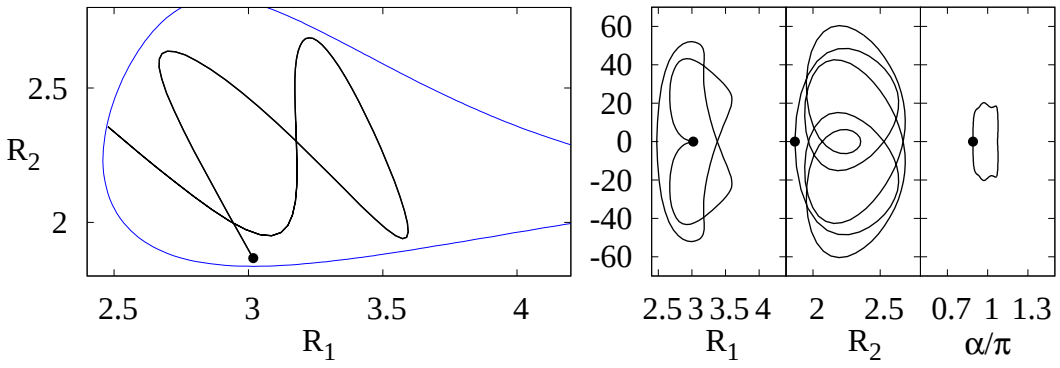


Figure 7.12: Projections of an orbit $\mathcal{O}_c$ and intersection point with the surface of section $p(\mathcal{O}_c)$ for the $E = 0.10$. In the left panel ((R_1, R_2 projection)) also shown the zero velocity curve ($T = 0$) of the collinear configuration

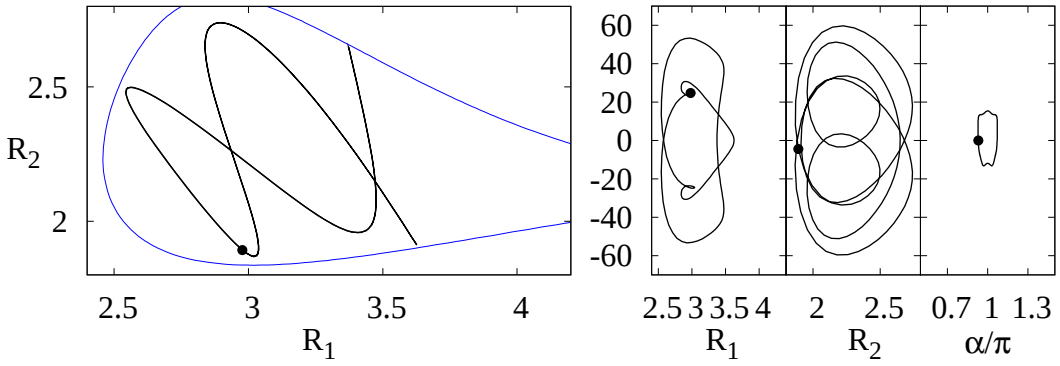


Figure 7.13: Projections of an orbit $\mathcal{O}_d$ and intersection point with the surface of section $p(\mathcal{O}_d)$ for the $E = 0.10$. In the left panel ((R_1, R_2 projection)) also shown the zero velocity curve ($T = 0$) of the collinear configuration

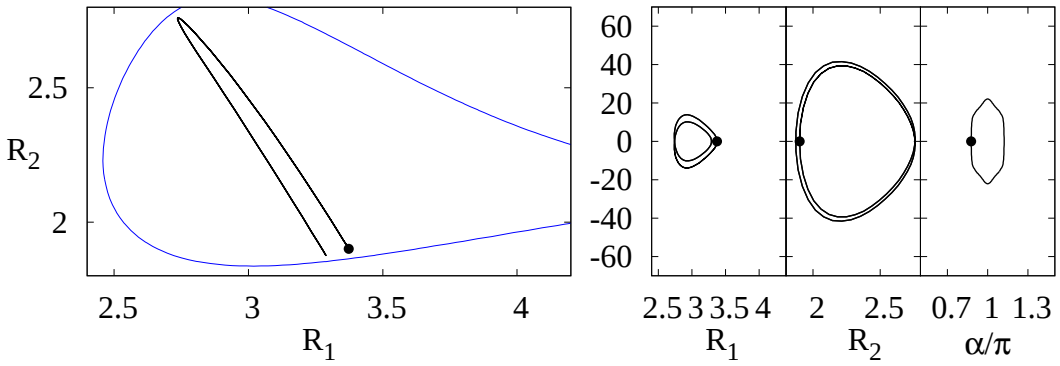


Figure 7.14: Projections of an orbit $\mathcal{O}_e$ and intersection point with the surface of section $p(\mathcal{O}_e)$ for the $E = 0.10$. In the left panel ((R_1, R_2 projection)) also shown the zero velocity curve ($T = 0$) of the collinear configuration

7.5 Trappings and transitions: bottlenecks and mechanisms

Investigating chaotic transport in phase space amounts to studying various structures which affect the dynamics. For example, rapid diffusion through phase space takes place through

the so-called accelerator modes [97]. In contrast, sticky structures like resonant islands or tori influence the dynamics by strongly slowing down the trajectories passing nearby. All these structures are responsible for anomalous diffusion and fractal kinetics in the system (for recent surveys, see Refs. [124, 123] and references therein). Identifying these structures and the mechanisms behind trapping, escape and roaming is essential for understanding the transport properties of a given system. Given that there are many such structures in a realistic system, the only realistic hope for forming a generally valid picture of transport is to locate invariant structures which are responsible for the main changes in the transport properties. In chemistry, such structures are referred as transition states or bottlenecks.

The specific question we address is: What are the structures in the phase space of OCS which is a fully three degree-of-freedom system that act as partial barriers to the diffusion of chaotic trajectories and what are their linear and nonlinear stability properties? What are these structures allowing transitions to other parts of phase space? In three dimensions, these invariant structures can be invariant tori with dimensions one (i.e. periodic orbits), two or three [74, 44, 20]. These structures can also include the stable/unstable manifolds.

Before going to the identification of such structures and the mechanisms for transitions, we provide details of these transitions by studying some observables and some adequate decomposition in the time-frequency plane. These decompositions allow us to identify accurately the transition region. A relevant Poincaré section of the dynamics reveal that in the region, the transition accumulate around particular curves. These curves are associated with invariant tori.

Using a combination of trajectory diagnostic tools like Lyapunov maps [103, 45], time-frequency analysis [18], and methods from the theory of dynamical systems like periodic and quasiperiodic orbit computations [104, 66], we relate the phenomenon of trapping to invariant structures in phase space and to lower-dimensional invariant tori (with a relation to their normal stability properties) in particular. It is commonly assumed that in "typical" Hamiltonian systems with a large number of degrees of freedom N, the relative measure of N-dimensional invariant tori (N local integrals) is either zero or one [43]. The implication is that chaotic systems with large N approach conditions of the stochastic ansatz, and hence,

the trapping phenomenon described above is insignificant. On the other hand, it has been established recently that high order resonances form robust islands of secondary structures with positive measure [59].

7.5.1 Calculations: Initial conditions

We have used two approaches to construct the initial loop. One could use data from the trajectory and select the segment containing the slow phase. Alternatively, one could make use of Eq. (Eq. (5.30)). The short time dynamics close to the fixed point is described well within the linear approximation. One could use eigenvectors of the $D\mathcal{F}_{\mathcal{S}}$ to construct an approximate initial loop γ_0. The rotation number ω is a free parameter. We typically choose a parameter which minimizes the residual $|\mathcal{F}_{\mathcal{S}}(\gamma_0) - \gamma_0 \circ \phi_\omega|$. This completes the selection process. Then we run a Newton optimizer on γ_0, which converges or fails. Even if the optimizer has converged, we cannot with certainty claim that a smooth two dimensional torus was found. We have noticed that crude discretization can wash out the details of non-smooth curves. In particular, sometimes doubling the number of points in the discretization makes convergent data diverge. In most cases the reliability of solutions is almost certain can be ascertained by testing the spectrum of the solution: a smooth solution should contain unit eigenvalue. Once a solution with a specific ω is found, we simply increment the frequency parameter $\omega \to \omega + \delta\omega$ and restart the search.

To describe the phenomenon we can introduce two time scales. We define the *capture time* as a time interval during which the trajectory is distinctly regular. We will abstain from defining exactly what are the boundaries of capture interval in acknowledgment of the fact that when trajectory loses regularity it does so gradually. To quantify this "escape" we introduce the *escape time*, $t_{\rm esc}$. Geometrically the two different timescales describe influence of different invariant phase space structures on a trajectory. Either of the characteristic times can be extracted from the stroboscopic data or surface of section data. The two time scales usually satisfy

$$t_{\rm trap} \gg t_{\rm esc} \tag{7.30}$$

We define the interval of regularity as the interval of time whose the segment of trajectory is

approximately quasiperiodic. This interval can be identified from various modes of representation. In the ridge plot, it is the interval which comprises of a small amount of persistent throughout the interval *principal* ridges with small average variation. It is allowed to have short lived ridges close to the principal ridges. Another indication of this interval is salient beating pattern in the time series plot.

To investigate the existence of lower dimensional invariant tori, we consider a fixed point with fully elliptic linear stability (surface of section of a (ee) periodic orbit). We will approximate the inertial manifold in the neighborhood of the fixed point by the tangent space at the fixed point, and dynamics in the inertial manifold by the linearization of the map at the fixed point, as described in Chapter 5. Such a loop has twofold degeneracy. One of them can be related to the arbitrariness of choice of the initial point, the second can be related to arbitrariness of the radius of the circle. Since the nonlinear corrections modify the rotation angle, one of the degeneracies can be lifted by specifying a fixed rotation angle ω. It implies that this way the family of tori, parameterized by ω can be obtained. Indeed, our search routine converges for a range of rotation numbers. Starting with ω, that is close to eigenfrequency of the Jacobian matrix, it is possible to obtain new invariant tori.

We have explored a large number of plots obtained by time–frequency analysis such as Figs. 7.3, 7.3, 7.3, 7.3. One distinguishing feature of regular segments in all of them is presence of two leading frequencies. One of them can be related to period of a relevant periodic orbit. To make the connection obvious we have plotted the relative frequency (relative frequency of the periodic orbit is 1). Having investigated the projection of trajectories on the surface of section, we found that the segment with the regular trajectory is approximately uniformly distributed in the neighborhood of a closed curve. Taking into consideration these circumstances we have come to the conclusion that segments of trajectories with regular dynamics "shadow" quasiperiodic two frequency solutions, in other words, 2-tori.

In order to approximate such torus, two approaches have been found useful. The continuation in parameter space was described earlier in Chapter 5. Here we describe a more direct and an efficient way to attack the problem. In the surface of section we are looking for a single frequency, the rotation number ω. It can be extracted using, for example,

Frequency map analysis of Laskar [31]. On the section of data, used in Figure 7.3, corresponding to $0 < t < t_{\text{trap}} \approx 300T_0$, we found approximate rotation number equal to $\omega_{\text{cap}} \approx 0.605558 \approx 3/5$. In this case, every 5-th iteration of the surface of section map will cover the curve uniformly and with the right parameterization, and the result, after interpolation and smoothing if required can be used a first approximation. Using this approach we have found tori, responsible for the near-regular dynamics.

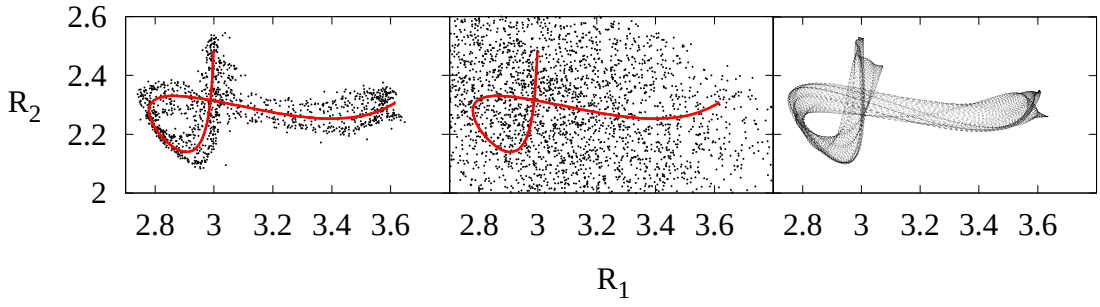


Figure 7.15: Projections of the trajectory near a periodic orbit $\mathcal{O}_a$ (with period T_0), analyzed in Figure 7.3. The trajectory is represented in (R_1, R_2) plots, broken down into segments, corresponding to the *trapping stage* (left panel) and chaotic stage (center panel). The bottleneck of transition from diffusion to hyperbolicity can be identified as a two-dimensional invariant torus (right panel.) The trajectory is sampled at fixed time intervals $T_0/2$. The orbit $\mathcal{O}_a$ is shown as a solid curve in the center.

In order to identify bottlenecks of transition from diffusion to chaos, we monitor the progress of invariant phase space structures along the transition channel using rotation numbers. The results are summarized in Figure 7.17, which is central to understanding this transition. In a trapping region around the elliptic periodic orbit $\mathcal{O}_a$ (left panel of Figure 7.5.1), the rotation numbers are obtained from the frequency map analysis [73] on the surface of section. It can be characterized by a single $\omega_{\text{trap}} \approx 0.60556$, implying that a two-dimensional torus is the relevant invariant structure in the trapping process. Having computed a family of two-dimensional tori, parameterized by rotation numbers ω, it is evident that ω_{trap} places the torus on the hyperbolic branch of the bifurcation diagram represented in Figure 7.17. This implies that the escape is mediated by manifolds of a torus with hyperbolic normal stability. The duration of the trapping stage is approximately 150 returns on Σ, and is consistent with the maximal Lyapunov exponent $\lambda < 0.05$. Processes

associated with the escape from the trapping region can be better understood by analyzing the tangent space of the elliptic periodic orbit $\mathcal{O}_a$ that locally has the structure of a direct product (center + center) $\mathbb{T} \times \mathrm{I}_1 \times \mathbb{T} \times \mathrm{I}_2$, with the periodic orbit at the origin. The elements of the two intervals $\mathrm{I}_i \subset \mathbb{R}$ are rotation numbers ω_i, which are not unique in general: The choice is fixed by requiring $\lim_{\mu \to 0} \omega_i = \omega_i^0$, where μ is a measure of the torus and ω_i^0 are stability angles of the elliptic periodic orbit $\mathcal{O}_a$ ($\omega_1^0 = 0.24500633$ and $\omega_2^0 = 0.37046872$). The Poincaré map induces rotations on $\mathbb{T}$, $r_{\omega_1} \times 1 \times r_{\omega_2} \times 1$, where r_ω is a rotation on $\mathbb{T}$ with the rotation number ω. Partial (or complete) resonances are determined by one (or two) resonance conditions $n\omega_1 + m\omega_2 + k = 0$, where (n, m, k) are integers such that $|n| + |m| + |k| > 0$. The most striking trapping effects are observed for partial resonances of the type $\mathbb{T} \times \mathrm{I}_1 \times \{0\} \times \{0\}$, and $\{0\} \times \{0\} \times \mathbb{T} \times \mathrm{I}_2$. Choosing either of the two situations, a resonance channel has been constructed by finding the two-dimensional invariant tori for $\omega_i \in \mathrm{I}_i$. In order to find these tori we consider the Poincaré map $\mathcal{F}_\Sigma : \Sigma \mapsto \Sigma$. Tori may have hyperbolic normal linear stability, therefore a search for them cannot rely on methods exploiting "stickiness" properties. The sections of two-dimensional invariant tori are one-dimensional closed curves (called hereafter "loops"). We consider loops as discretizations of $\gamma : \mathbb{T} \mapsto \Sigma$ (with periodic boundary condition $\gamma(s) = \gamma(s+1)$) and require that the Poincaré map $\mathcal{F}_\Sigma$, restricted to the loop is equivalent to a rigid rotation r_ω. This translates into an invariance condition:

$$\mathcal{F}_\Sigma(\gamma(s)) = \gamma(s + \omega). \tag{7.31}$$

Equation (7.31) is solved using damped Newton iterations for the Fourier coefficients of $\gamma(s)$. The linear stability properties of the loop are determined by (Λ, ψ), solutions of the generalized eigenvalue problem:

$$D\mathcal{F}_\Sigma(s)\psi(s) = \Lambda\psi(s + \omega). \tag{7.32}$$

Equation (7.32) has a one-dimensional kernel, which we eliminate using singular value decomposition. The initial data for the Newton iterations $\gamma_0(s)$ and ω were obtained using one of the following two methods : The first method uses the trapping region of the trajectory (see Figure 7.3). We estimate ω using Fourier-like methods [73], and truncate the continued

ω	value	Cont. frac.
ω_A^c	0.240711317575	[4, 6, 2, 11, 5, 5...]
ω_B^c	0.215852976389	[4, 1, 1, 1, 2, 1, 1, 1, 1, 2, 1, 1...]
ω_C^c	0.608654398762	[1, 1, 1, 1, 4, 45, 1, 1, 1, 1...]
ω_D^c	0.605804087926	[1, 1, 1, 1, 6, 3, 2, 2, 1...]

Table 7.1: Rotation numbers of the two-dimensional invariant tori at the bifurcation points A, B, C, D shown in Fig. 4.

fraction expansion of $\omega = [a_1, a_2, \ldots]$ before the first large a_i so that $\omega_0 = P/Q$. Then we take sequences of trapping region data every Q iterations and combine them to obtain $\gamma_0(s)$. A refined value of ω can be estimated by minimizing $|\mathcal{F}_\Sigma \circ \gamma_0 - \gamma_0 \circ r_\omega|$. The second method combines continuation in ω with the direct product structure in the neighborhood of the periodic orbit. The surface of section derivative $D\mathcal{F}_\Sigma$ at the periodic orbit has two pairs of complex eigenvalues $\exp[\pm\iota\omega_i^0]$, $i = 1, 2$. The eigenvectors define mutually skew orthogonal symplectic vector spaces $V_i = \mathbb{R}^2$. It is assumed here that the linear approximation is effective in the neighborhood of the periodic orbit.

The set of two-dimensional tori is found to be discontinuous at the gaps in Figure 7.17 due to complete resonances (periodic orbits) and secondary invariant structures. Normal stability is typically elliptic for small $|\omega - \omega_i^0|$. We identify the two-dimensional invariant torus at the period doubling bifurcation point as a bottleneck of a given resonance channel. The rationale follows from the theory of dynamical systems: Beyond the bifurcation point at $\omega = \omega^c$, the normal stability changes to hyperbolic. This change affects trajectories passing by its neighborhood. One recurrent observation is that the continued fraction expansion of bifurcation rotation numbers has a tail composed of small integers (see Tab. 7.1). This feature is reminiscent of the observation that the continued fraction expansion of the frequency of the last invariant torus in generic Hamiltonian systems with two degrees of freedom is noble (with a tail of ones) in many situations [26].

The reliability of the numerical solution can be tested by examining its Floquet multipliers, given by Eq. (7.32). An exact solution consists of a set of complex numbers with up to three different absolute values: 1, Λ, $1/\Lambda$. Significant variation from these values signals an unreliable solution.

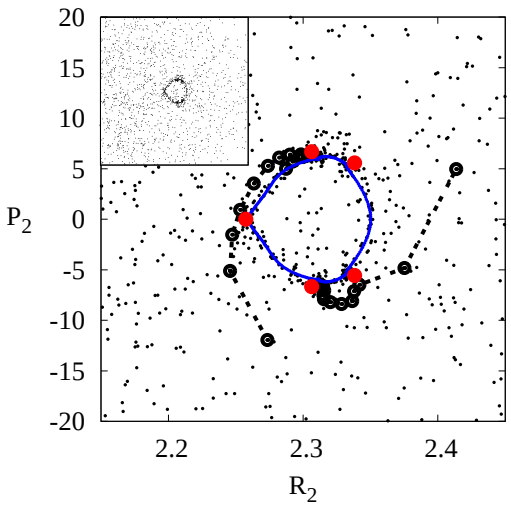


Figure 7.16: Poincaré section of the trajectory near a periodic orbit $\mathcal{O}_a$, analyzed in Figs. 7.3 and Figure 7.5.1. The bottleneck (a two-dimensional torus) is a loop (blue) at the bifurcation point ("D" in Figure 7.17). The trajectory is trapped in the vicinity of a loop (which is clearly seen from the inset). The escape stage is shown as two "tentacles," which extend along the unstable manifolds of a resonant periodic orbit (the five red dots around the center).

In conclusion, our findings indicate that trapping and escape are mediated by the same sequence of events, and an approximate boundary, which separates trapped and chaotic behavior, can be found in analogy with the boundaries that separate reactants from products in Transition State Theory [91], where sharply defined phase space structures [93, 79, 80, 117] play this role.

In a broader context, our work forms yet another stimulus to reconsider the relevance of local integrals and partial resonances in realistic, chaotic Hamiltonian systems with many degrees of freedom. Here, we have explained a paradoxical situation, namely that integral surfaces with *positive* Lyapunov exponents (i.e., not "sticky") can trap chaotic trajectories. Widespread observations of repeated trapping-escape-chaotic processes in short trajectory segments provide evidence that these effects are generic and occurring frequently in many settings ranging from plasmas to celestial mechanics.

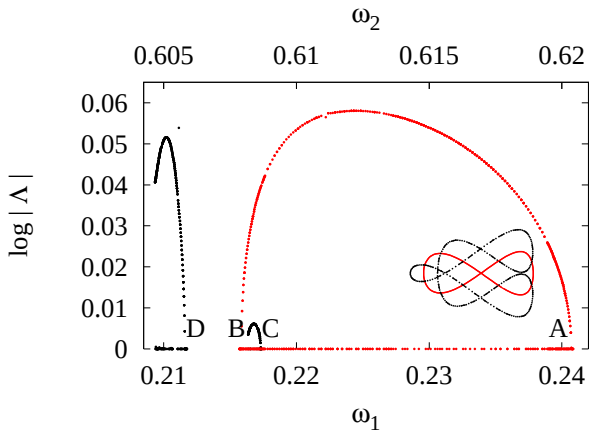


Figure 7.17: Fine structure of invariant tori, scanned along the transition channel. The plot shows how Lyapunov exponents depend on the rotation number ω. The points of frequency halving bifurcations ("A"– "D") can be interpreted as bottlenecks of transition from diffusion to hyperbolicity. Red dots: family of loops arising from the periodic orbit $\mathcal{O}_a$. Black dots: frequency halved loop, emerging at the bifurcation point "A". Insets display (R_1,P_1) projections of loops near the bifurcation point "A". Red: loop with elliptic normal stability and $\omega = \omega_1 \approx 0.24067$. Black: loop with hyperbolic normal stability and $\omega = \omega_2 = (\omega_1 + 1)/2 \approx 0.62033$.

CHAPTER VIII

CONCLUSIONS

We investigate chaotic ionization of highly excited hydrogen atom in crossed electric and magnetic fields (Rydberg atom) and anomalies in vibrational energy relaxation of carbonyl sulfide (OCS) molecule. Both systems are modeled by Hamiltonians with three degree of freedom. It is now commonly accepted that trajectories, simulating Rydberg atoms and molecules in highly excited states exhibit some degree of chaos. Classical statistical methods to determine reaction rates (Transition State Theory) are based on the assumption that energy redistribution is exponentially fast and uniform throughout the phase space. Evidence, accumulated over the past several decades, shows a very complex nonuniform dynamics in such systems, leading to *chaotic* transport, *stickiness* and *intermittency* phenomena. We investigate various aspects of transport in 2- and 3-degree of freedom (dof) Hamiltonian systems in the conditions of *hard chaos* and uncover phase space structures, that a) cause chaotic transport, and b) slow it down.

Our main achievements are

Developing general methods to partition the phase space of complex 2-dof Hamiltonian system in terms of periodic orbits. We have applied our methods to describe, and compute a large number of periodic orbits of the planar crossed-fields problem.

Developing methods to compute unstable invariant tori in general 3-dof Hamiltonian systems and

Successfully applying these methods to explain the phenomenon of trapping in molecules. This phenomenon is relevant in chemistry because it leads to energy flow slower than that predicted by RRKM theories .

Results we obtain are general in their nature and have implications for chaotic high-dimensional Hamiltonian systems beyond the particular systems discussed in this work.

I would like to stress several possible directions of research in area, related to my thesis:

To develop methods for partitioning high dimensional Hamiltonian systems. Our work has indicated how this may be possible using normally hyperbolic invariant manifolds.

Further develop periodic orbit approach using our periodic orbit partition.

The problem of nontransversal intersections is a major impediment to efficient calculations. Possibly using multiple surfaces of section, or devising clever algorithms to avoid these intersections would provide valuable tools for calculations similar to ours.

APPENDIX A

CROSSED-FIELDS RELATED MATERIAL

A.1 Hamiltonian and scaling: Atomic to scaled units

In SI units, the Lagrangian of the crossed-fields problems is written as

$$L = \frac{m_e \dot{x}^2}{2} + \frac{e}{2m_e c}\mathbf{A}\cdot\mathbf{v} + \frac{e}{4\pi\epsilon_0|\mathbf{r}|} + \mathbf{F}\cdot\mathbf{r} \tag{A.1}$$

Where it is customary to take the vector potential in symmetric gauge $\mathbf{A} = \mathbf{B}\times\mathbf{r}$. Here, $\mathbf{r} = (x, y, z)$, $|\mathbf{r}| = \sqrt{x^2+y^2+z^2}$, $\mathbf{B} = (0, 0, B)$, $\mathbf{F} = (F, 0, 0)$. To minimize the number of constants, one can introduce two scaling factors. Atomic units are obtained by scaling the length to the Bohr radius a_B and Lagrangian (action) to the Planck's constant $\hbar$ or, equivalently, momentum to $\hbar/a_B$. A few relevant physical constants are listed in the Table A.1

Table A.1: Physical constants, relevant for scaling to atomic units in the crossed-fields problem. The bottom line shows scaling factor of the magnetic field.

Description	Symbol	Value
Bohr radius	a_B	$0.5291772108\times10^{-10}\,\mathrm{m}$
Planck's constant	$\hbar$	$1.054571\times10^{-34}\,\mathrm{J}$
Speed of light	c	$2.99792458\times10^{8}\,\mathrm{m/s}$
Charge of electron	e	$1.60217653\times10^{-19}\,\mathrm{C}$
Mass of electron	m_e	$9.1093826\times10^{-31}\,\mathrm{kg}$
Magnetic Field	$m_e a_B^3 e/\hbar^2 c$	$2.25\times10^{5}\,\mathrm{T}$

In atomic units the Hamiltonian reads as

$$H_{\text{a.u.}} = \frac{p^2}{2} + \frac{B}{2}L_z + \frac{B^2}{8}(x^2+y^2) - 1/|\mathbf{r}| + Fx \tag{A.2}$$

The "scaled" coordinates in the crossed-fields problem usually refer to the coordinates, scaled using the following procedure. The Hamiltonian Eq. (3.1) apparently has three parameters: the field strengths B and F and the total energy E. By scaling distance and time units once more, the so-called scaled units are obtained, and Hamiltonian explicitly

depends only on two parameters. Using this scaling, one of the parameters can be set to arbitrary numerical value, to unit, for example. Momenta scale as $[P] = LT^{-1}$, magnetic field $[B] = T^{-1}$, electric field $[F] = L^{-2}$, energy (Hamiltonian) $[H] = L^{-1}$. It is useful to introduce field and energy "sizes" which have length dimensions. $\mathcal{R}_F : F = \mathcal{R}_F^{-2}$ and $\mathcal{R}_H : \mathcal{H} = -2\mathcal{R}_H^{-1}$. Most popular scaling is to eliminate magnetic field by scaling B to unity.

This scaling can be viewed as scaling of time to Larmor period (inverse of a Larmor frequency) B^{-1}.

The two relevant scale factors are time scale $t_M = \Omega t_N$ and length scale, $\mathbf{Q}_M = \Omega^{2/3}\mathbf{Q}_N$.

$$\begin{aligned} \mathcal{H} &= \Omega^{2/3}E; \quad T = \Omega^{-1}t \\ \mathbf{P} &= \Omega^{1/3}\mathbf{p}; \quad \mathbf{Q} = \Omega^{-2/3}\mathbf{q} \end{aligned} \tag{A.3}$$

Electric field elimination can be viewed as time scaling to cyclic period of electric periodic orbit $\mathcal{R}_F^{3/2}$ and of energy to that of the (negative of) saddle point potential $\mathcal{R}_F^{-1}$. Thus the two scaling factors are $t_E = \mathcal{R}_F^{-3/2}t_N$ and $\mathbf{Q}_E = \mathcal{R}_F^{-1}\mathbf{Q}_N$. Namely

$$\begin{aligned} \mathcal{E} &= \mathcal{R}_F^{-1}E; \quad\quad T = \mathcal{R}_F^{3/2}t \\ \mathbf{P} &= \mathcal{R}_F^{-1/2}\mathbf{p}; \quad \mathbf{Q} = \mathcal{R}_F\mathbf{q} \end{aligned} \tag{A.4}$$

Converting from one scaling to a different is easy. Just assume that initial coordinates are not scaled and apply a particular scaling. For example, to go from magnetic scaling to electric, the appropriate transformation is (A.4) with $\Omega = 1$, and the resulting Hamiltonian is

$$\mathcal{H}_F = \left[(p_x - \mathcal{R}_F^{3/2}y/2)^2 + (p_y + \mathcal{R}_F^{3/2}x/2)^2 + p_z^2\right]/2 - 1/r + x$$

A.2 Values of field parameters, used in experiment or ab-initio calculations

In [84, 85] ab-initio calculations used $F = 5140\,\mathrm{V/cm}$, $B = 6, 12.5, 21\,\mathrm{T}$.

In [41], experimental photoabsorption spectrum $B = 6.002\,\mathrm{T}$, $F = 750...1000\,\mathrm{V/cm}$

In [120], experiments were done on $B = 6\,\mathrm{T}$, $F = 2000, 3000, 4000\,\mathrm{V/cm}$.

Table A.2: The shortest periodic points in the homoclinic tangle of figure 4.7 to figure 4.11, S_4, planar crossed fields problem.

Symbol	N	Coordinates				T	Λ
A_0	4	-1.868233200938	0.091472869325	0.182945738649	0.446847460817	32.4086359138	4.7313666090e+00
A_1	4	-1.988269334707	-0.000000000001	-0.000000000001	0.517166286449	32.6953422695	-3.3628816852e+00
B_0	5	-1.886017172669	0.141723056272	0.283446112544	0.465509887597	40.9930457776	1.7099138034e+01
B_1	5	-2.035249538414	-0.000000000000	-0.000000000000	0.544663154238	41.3146606919	-2.9580478590e+01
A_0A_1	8	-1.971311243789	0.042481530008	0.084963060015	0.507949063780	65.2796106882	-7.8429379174e+00
A_0B_0	9	-1.919335868072	0.109651882815	0.219303765631	0.481750633406	73.4523315227	8.7358606814e+01
A_0B_1	9	–	–	–	–	–	–
A_1B_0	9	-2.010459030851	0.000000000000	0.000000000000	0.530291746133	73.7119382177	-1.0859611906e+02
A_1B_1	9	–	–	–	–	–	–
B_0B_1	10	-1.916001123206	0.136250876262	0.272501752525	0.483472404143	82.2861286305	-5.3066823455e+02
$A_0A_0A_1$	12	-1.948350593921	0.076302000715	0.152604001430	0.496180978751	97.7020371882	-3.9197016035e+01
$A_0A_0B_0$	13	-1.924720156784	0.103942454578	0.207884909156	0.484403448070	105.8826262248	4.1790384467e+02
$A_0A_0B_1$	13	–	–	–	–	–	–
$A_0A_1A_1$	12	-1.962693975199	0.044909883075	0.089819766151	0.502836017133	97.9485804644	3.9662351252e+01
$A_0A_1B_0$	13	–	–	–	–	–	–
$A_0A_1B_1$	13	–	–	–	–	–	–
$A_0B_0A_1$	13	-1.909258450661	0.105945358723	0.211890717446	0.474957632635	106.1512596395	-5.0372110083e+02
$A_0B_0B_0$	14	-1.921885983013	0.110589765936	0.221179531873	0.483461540635	114.4497610257	1.5103058282e+03
$A_0B_0B_1$	14	-1.943305742148	0.112143821019	0.224287642039	0.496883366438	114.7418478353	-2.2187975398e+03
$A_0B_1A_1$	13	–	–	–	–	–	–
$A_0B_1B_0$	14	–	–	–	–	–	–
$A_0B_1B_1$	14	–	–	–	–	–	–
$A_1A_1B_0$	13	–	–	–	–	–	–
$A_1A_1B_1$	13	–	–	–	–	–	–
$A_1B_0B_0$	14	-2.011597798884	0.000000000000	0.000000000000	0.530958617046	114.7092264881	-1.9212148594e+03
$A_1B_0B_1$	14	-2.020873328792	0.024111661224	0.048223322449	0.536663399208	115.0044423532	2.8320699050e+03
$A_1B_1B_0$	14	–	–	–	–	–	–
$A_1B_1B_1$	14	–	–	–	–	–	–
$B_0B_0B_1$	15	-1.904772603906	0.145647714756	0.291295429511	0.478020217142	123.2717517105	-8.9319555809e+03
$B_0B_1B_1$	15	-1.915216004062	0.136410737519	0.272821475037	0.483009537988	123.6043523179	1.5861824667e+04

REFERENCES

[1] Abraham, R. and Marsden, J. E., *Foundations of Mechanics.* Reading, Mass.: Benjamin/Cummings, 2nd ed., 1978.

[2] Anderson, E., Bai, Z., Bischof, C., Blackford, S., Demmel, J., Dongarra, J., Du Croz, J., Greenbaum, A., Hammarling, S., McKenney, A., and Sorensen, D., *LAPACK Users' Guide.* Philadelphia, PA: Society for Industrial and Applied Mathematics, third ed., 1999.

[3] Arnold, V. I., "Instabilities of dynamical systems with several degrees of freedom," *Sov. Math. Dokl.*, vol. 5, pp. 581–585, 1964.

[4] Balian, R. and Bloch, C., "Distribution of eigenfrequencies for the wave equation in a finite domain: Iii. eigenfrequency density oscillations," *Ann. Phys.*, vol. 69, no. 1, pp. 76–160, 1971.

[5] Balian, R. and Bloch, C., "Solution of the Schrödinger equation in terms of classical paths," *Ann. Phys.*, vol. 85, pp. 514–545, 1974.

[6] Bartsch, T., *The hydrogen atom in an electric field and in crossed electric and magnetic fields: Closed-orbit theory and semiclassical quantization.* PhD thesis, University of Stuttgart, Germany, 2002.

[7] Bellomo, P., Farrelly, D., and Uzer, T., "Excitation and stability of ultrahigh Rydberg states in stray electric fields," *J. Phys. Chem. A*, vol. 101, p. 8902, 1997.

[8] Bensimon, D. and Kadanoff, L. P., "Extended chaos and the disappearance of KAM trajectories," *Physica D*, vol. 13, p. 82, 1984.

[9] Bethe, H. A. and Salpeter, E. E., *Quantum Mechanics of One- and Two-Electron Atoms.* N.Y.: Plenum, 1977.

[10] Bogoliubov, N. N., Mitropolskii, Y. A., and Samoĭlenko, A. M., *Methods of Accelerated Convergence in Nonlinear Mechanics.* Berlin: Springer, 1976.

[11] Bogomol'nyĭ, E. B., "Photoabsorption by atoms in external fields near the ionization threshold," *Sov. Phys. JETP*, vol. 69, no. 2, pp. 275–283, 1989.

[12] Bowen, R., *Equilibrium States and the Ergodic theory of Anosov Diffeomorphisms.* N.Y.: Springer, 1975.

[13] Bowen, R., *On Axiom A Diffeomorphisms.* Providence: Amer. Math. Soc., 1978.

[14] Braun, P. A. and Solov'ev, E. A., "The Stark effect for the hydrogen atom in a magnetic field," *Sov. Phys. JETP*, vol. 59, no. 1, pp. 38–46, 1984.

[15] Broer, H. W. and Simó, C., "Hill's equation with quasi-periodic forcing: resonance tongues, instability pockets and global phenomena," *Bol. Soc. Bras. Mat.*, vol. 29, pp. 253–293, 1998.

[16] Brunello, A. F., Farrelly, D., and Uzer, T., "Hydrogen atom in circularly polarized microwaves: Chaotic ionization via core scattering," *Phys. Rev. A*, vol. 55, pp. 3730–3745, 1997.

[17] Carter, D. and Brumer, P., "Intramolecular dynamics and nonlinear mechanics of model OCS," *J. Chem. Phys.*, vol. 77, p. 4208, 1982.

[18] Chandre, C., Wiggins, S., and Uzer, T., "Time-frequency analysis of chaotic systems," *Physica D*, vol. 181, pp. 171–196, 2003.

[19] Chirikov, B. V., Ford, J., and Vivaldi, F., "Some numerical studies of Arnold diffusion in a simple model," in *Nonlinear Dynamics and the Beam-Beam Interaction* (Month, M. and Herrera, J. C., eds.), vol. 57 of *AIP Conference Proceedings*, (Brookhaven National Laboratory), pp. 272–340, American Institute of Physics, American Institute of Physics, 1979.

[20] Cincotta, P. and Simó, S., "Simple tools to study global dynamics in non-axisymmetric galactic potentials," *A&AS*, vol. 147, p. 205, 2000.

[21] Connerade, J.-P., *Highly Excited Atoms*. UK: Cambridge University Press, 1998.

[22] Cushman, R. and Sadovskii, D. A., "Monodromy in the hydrogen atom in crossed fields," *Physica D*, vol. 142, pp. 166–196, 2000.

[23] Cvitanović, P., Artuso, R., Mainieri, R., Tanner, G., and Vattay, G., *Chaos: Classical and Quantum*. Copenhagen: Niels Bohr Institute, 2007. `www.ChaosBook.org/version11`.

[24] Cvitanović, P., Artuso, R., Mainieri, R., Tanner, G., and Vattay, G., *Chaos: Classical and Quantum*. Copenhagen: Niels Bohr Institute, 2007. `www.ChaosBook.org/version11`.

[25] Davis, M. J., "Exponential separation and long-time correlation in collinear OCS," *Chem. Phys. Lett.*, vol. 110, no. 5, pp. 491–495, 1984.

[26] Davis, M. J., "Bottlenecks to the intramolecular energy transfer and the calculation of relaxation rates," *J. Chem. Phys.*, vol. 83, p. 1016, 1985.

[27] Davis, M. J. and Gray, S. K., "Unimolecular reactions and phase space bottlenecks," *J. Chem. Phys.*, vol. 84, no. 10, pp. 5389–5411, 1986.

[28] Davis, M. J. and Wagner, A., "The intramolecular dynamics of highly excited OCS," in *Resonances in Electron-Molecule Scattering, van der Waals Complexes, and Reactive Chemical Scattering* (Truhlar, D. G., ed.), vol. 263 of *ACS Symposium Series*, American Chemical Society, 1984.

[29] Dignam, M. M. and Sipe, J. E., "Semiconductor superlattice exciton states in crossed electric and magnetic fields," *Phys. Rev. B*, vol. 45, p. 6819, 1992.

[30] Du, M. L. and Delos, J. B., "Effect of closed classical orbits on quantum spectra: Ionization of atoms in a magnetic field. i. physical picture and calculations," *Phys. Rev. A*, vol. 38, pp. 1896–1912, Aug 1988.

[31] Dumas, H. S. and Laskar, J., "Global dynamics and long-time stability in hamiltonian systems via numerical frequency analysis," *Phys. Rev. Lett.*, vol. 70, p. 2975, 1993.

[32] Eliasson, L. H., "Floquet solutions for the 1-dimensional quasi-periodic Schrödinger equation," *Commun. Math. Phys.*, vol. 146, pp. 447–482, 1992.

[33] Eliasson, L. H., "Reducibility and point spectrum for linear quasi-periodic skew-products," in *Proc. Int. Congress of of Mathematicians*, vol. 2, pp. 779–787, 1998.

[34] Eliasson, L. H., "Almost reducibility of linear quasi-periodic systems," in *Proc. Sympos. Pure Math.*, vol. 69, (Providence, RI), pp. 679–705, Amer. Math. Soc., 2001.

[35] Farantos, S. C. and Murrell, J. N., "On the transition from quasiperiodic to stochastic classical motion on real polyatomic potential energy surfaces," *Chem. Phys.*, vol. 55, pp. 205–214, 1981.

[36] Fermi, E., Pasta, J. R., and Ulam, S., "Studies of nonlinear problems.," Tech. Rep. Report LA-1940, Los Alamos, 1955.

[37] See, e.g., articles in the Focus Issue *The Fermi-Pasta-Ulam Problem: The First Fifty Years*, Chaos **15**(1) (March 2005).

[38] Flöthmann, E. and Welge, K. H., "Crossed-field hydrogen and the three-body Sun-Earth-Moon problem," *Phys. Rev. A*, vol. 54, no. 3, pp. 1884–1888, 1996.

[39] Foord, A., Smith, J. G., and Whiffen, D. H., "An anharmonic force field for carbonyl sulphide," *Mol. Phys.*, vol. 29, no. 6, pp. 1685–704, 1975.

[40] Forst, W., *Theory of Unimolecular Reactions.* NY: Academic Press, 1973.

[41] Freund, S., Ubert, R., Flöthmann, E., Welge, K., Wang, D. M., and Delos, J. B., "Absorption and recurrence spectra of hydrogen in crossed electric and magnetic fields," *Phys. Rev. A*, vol. 65, 2002.

[42] Friedrich, H. and Wintgen, D., "The hydrogen atom in a uniform magnetic field - an example of chaos," *Phys. Rep.*, vol. 183, p. 37, 1989.

[43] Froeschlé, C., "On the number of isolating integrals in systems with three degrees of freedom," *Astrophysics and Space Science*, vol. 14, no. 1, pp. 110–117, 1971.

[44] Froeschlé, C., Gonczi, R., and Lega, E., "The fast lyapunov indicator: a simple tool to detect weak chaos. Application to the structure of the main asteroidal belt," *Planet. Space Sci.*, vol. 45, pp. 881–886, 1997.

[45] Froeschlé, C., Lega, E., and Gonczi, R., "Fast Lyapunov indicators. Application to asteroidal motion," *Celest. Mech. Dyn. Astr.*, vol. 67, pp. 41–62, 1997.

[46] Gallagher, T. F., *Rydberg Atoms.* UK: Cambridge University, 1994.

[47] Garton, W. R. S. and Tomkins, F. S., "Diamagnetic Zeeman effect and magnetic configuration mixing in long spectral series of Ba I," *Astrophys. J.*, vol. 158, p. 839, 1969.

[48] Gibson, J. F., Halcrow, J., and Cvitanović, P., "Visualizing the geometry of state space in plane Couette flow," *arXiv:0705.3957v4 [physics.flu-dyn]*, 2007.

[49] Gibson, L. L., Schatz, G. C., Ratner, M. A., and Davis, M. J., "Phase space bottlenecks: A comparison of quantum and classical intramolecular dynamics for collinear OCS," *J. Chem. Phys.*, vol. 86, p. 3263, 1986.

[50] Gillilan, R. E., "Invariant surfaces and phase space flux in three-dimensional surface diffusion," *J. Chem. Phys.*, vol. 93, p. 5300, 1990.

[51] Gillilan, R. E. and Ezra, G. S., "Transport and turnstiles in multidimensional hamiltonian mappings for unimolecular fragmentation: Application to van der waals predissociation," *J. Chem. Phys.*, vol. 94, p. 2648, 1991.

[52] Glasstone, S., Laidler, K. J., and Eyring, H., *The Theory of Rate Processes.* Wiley, NY, 1941.

[53] Gourlay, M. J., Uzer, T., and Farrelly, D., "Asymmetric-top description of Rydberg-electron dynamics in crossed external fields," *Phys. Rev. A*, 1993.

[54] Gray, S. K. and Rice, S. A., "Phase space bottlenecks and statistical theories of isomerization reactions," *J. Chem. Phys.*, vol. 86, no. 4, pp. 2020–2035, 1987.

[55] Gutzwiller, M. C., "Phase-integral approximation in momentum space and the bound states of an atom. ii," *J. Math. Phys.*, vol. 10, no. 6, pp. 1004–1021, 1969.

[56] Gutzwiller, M. C., *Chaos in Classical and Quantum Mechanics.* N.Y.: Springer, 1990.

[57] Hamilton, I. and Brumer, P., "Intramolecular relaxation in $n = 2$ Hamiltonian systems: The role of the K entropy," *J. Chem. Phys.*, vol. 78, pp. 2682–2690, 1983.

[58] Hardy, G. H. and Wright, E. M., *An Introduction to the Theory of Numbers.* Oxford, 1979.

[59] Haro, A. and de la Llave, R., "New mechanisms for lack of equipartition of energy," *Phys. Rev. Lett.*, vol. 85, no. 9, pp. 1859–1862, 2000.

[60] Hasegawa, H., Robnik, M., and Wunner, G., "Classical and quantal chaos in the diamagnetic Kepler problem : Part ii. quantal aspects : New trends in chaotic dynamics of hamiltonian systems," *Prog. Theor. Phys. Suppl.*, vol. 98, p. 198, 1989.

[61] Herzberg, G., "Rydberg molecules," *Annu. Rev. Phys. Chem.*, vol. 38, p. 27, 1987.

[62] Hirsch, M. W., Pugh, C. C., and Shub, M., *Invariant Manifolds.* N.Y.: Springer, 1977.

[63] Holle, A., Wiebusch, G., Main, J., Hager, B., Rottke, H., and Welge, K. H., "Diamagnetism of the hydrogen atom in the quasi-Landau regime," *Phys. Rev. Lett.*, vol. 56, pp. 2594–2597, Jun 1986.

[64] Iu, C., Welch, G. R., Kash, M. M., Kleppner, D., Delande, D., and Gay, J. C., "Diamagnetic rydberg atom: Confrontation of calculated and observed spectra," *Phys. Rev. Lett.*, vol. 66, no. 2, pp. 145–148, 1991.

[65] Jaffé, C., Farrelly, D., and Uzer, T., "Transition state theory without time-reversal symmetry: Chaotic ionization of the hydrogen atom," *Phys. Rev. Lett.*, vol. 84, pp. 610–613, 2000.

[66] Jorba, À., "Numerical computation of the normal behaviour of invariant curves of n-dimensional maps," *Nonlinearity*, vol. 14, pp. 943–976, 2001.

[67] Jorba, A., Ramírez-Ros, R., and Villanueva, J., "Effective reducibility of quasiperiodic linear equations close to constant coefficients," *SIAM. J. Math. Anal.*, vol. 28, pp. 178–188, 1997.

[68] Jorba, A. and Simó, C., "On the reducibility of linear differential equations with quasiperiodic coefficients," *J. Diff. Equ.*, vol. 98, pp. 111–124, 1992.

[69] Katok, A. and Hasselblatt, B., *Introduction to the Modern Theory of Dynamical Systems*, vol. 54 of *Encyclopedia of mathematics and its applications*. UK: Cambridge University, 3 ed., 1995.

[70] Kolmogorov, A., "On the conservation of quasi-periodic motions for a small change in the Hamiltonian function," *Dokl. Akad. Nauk SSSR*, vol. 98, pp. 527–530, 1954. (in russian).

[71] Kolmogorov, A., "Preservation of conditionally periodic movements with small change in the Hamilton function," in *Stochastic Behaviour in Classical and in Quantum Hamiltonian Systems* (Casati, G. and Ford, J., eds.), vol. 93 of *Lecture Notes in Physics*, pp. 51–56, Berlin: Springer, 1979.

[72] Kustaanheimo, P. and Stiefel, E., "Perturbation theory of Kepler motion based on spinor regularization," *J. Ang. Math*, vol. 218, pp. 204–219, 1965.

[73] Laskar, J., "Frequency analysis for multi-dimensional systems. Global dynamics and diffusion," *Physica D*, vol. 67, pp. 257–281, 1993.

[74] Laskar, J., "Introduction to frequency map analysis," in *Hamiltonian Systems with Three or More Degrees of Freedom. NATO ASI Series, Series C: Mathematical and Physical Sciences Vol. 533* (Simó, C., ed.), (Dordrecht), p. 134, Kluwer, 1999.

[75] Li, Y. and Yi, Y., "On Poincaré - Treshchev tori in Hamiltonian systems," *Proc. Diff. Eqns.*, pp. 136–151, 2003.

[76] Li, Y. and Yi, Y., "A quasi-periodic Poincaré's theorem," *Math. Ann.*, vol. 326, pp. 649–690, 2003.

[77] Lichtenberg, A. J. and Lieberman, M. A., *Regular and Chaotic Dynamics*, vol. 38 of *Applied Mathematical Sciences*, ch. 6: Three of More Degrees of Freedom, pp. 373–456. Springer, second ed., 1992.

[78] Lorenz, E. N., "Deterministic non-periodic flow," *J. Atmos. Sci.*, vol. 29, pp. 130–141, 1963.

[79] MacKay, R. S., "Flux over a saddle," *Phys. Lett. A*, vol. 145, p. 425, 1990.

[80] MacKay, R. S., "A variational principle for invariant odd-dimensional submanifolds of an energy surface for hamiltonian systems," *Nonlinearity*, vol. 4, p. 155, 1991.

[81] MacKay, R. S., Meiss, J. D., and Percival, I. C., "Transport in Hamiltonian systems," *Physica D*, vol. 13, p. 55, 1984.

[82] Main, J., Wiebusch, G., Holle, A., and Welge, K. H., "New quasi-Landau structure of highly excited atoms: The hydrogen atom," *Phys. Rev. Lett.*, vol. 57, pp. 2789–2792, Dec 1986.

[83] Main, J., Wiebusch, G., Welge, K., Shaw, J., and Delos, J. B., "Recurrence spectroscopy: Observation and interpretation of large-scale structure in the absorption spectra of atoms in magnetic fields," *Phys. Rev. A*, vol. 49, pp. 847–868, Feb 1994.

[84] Main, J. and Wunner, G., "Ericson fluctuations in the chaotic ionization of the hydrogen atom in crossed magnetic and electric fields," *Phys. Rev. Lett.*, vol. 69, p. 586, 1992.

[85] Main, J. and Wunner, G., "Rydberg atoms in external fields as an example of open quantum systems with classical chaos," *J. Phys. B*, vol. 27, pp. 2835–2848, 1994.

[86] Martens, C. C., Davis, M. J., and Ezra, G. S., "Local frequency analysis of chaotic systems in multidimensional systems: Energy transport and bottlenecks in planar OCS," *J. Chem. Phys.*, vol. 142, 519–528 1987.

[87] May, R., "Simple mathematical models with very complicated dynamics," *Nature*, vol. 261, pp. 459–467, 1976.

[88] Meyer, K. R., "Jacobi elliptic functions from a dynamical systems point of view," *American Mathematical Monthly*, vol. 108, 2001.

[89] Muratore-Ginanneschi, P., "Path integration over closed loops and Gutzwiller's trace formula," *Phys. Rep.*, vol. 383, p. 299, 2003.

[90] Netlib: a collection of mathematical software, papers, and databases `www.netlib.org`.

[91] Pechukas, P., "Statistical approximations in collision theory," in *Dynamics of Molecular Collisions, Part B* (Miller, W. H., ed.), ch. 6, N.Y.: Plenum, 1976.

[92] Perry, A. D. and Wiggins, S., "KAM tori are very sticky: rigorous lower bounds on the time to move away from an invariant Lagrangian torus with linear flow," *Physica D*, vol. 71, p. 102, 1994.

[93] Pollak, E. and Pechukas, P., "Transition states, trapped trajectories, and classical bound states embedded in the continuum," *J. Chem. Phys.*, vol. 69, no. 3, pp. 1218–1226, 1978.

[94] Raithel, G., Fauth, M., and Walther, H., "Quasi-Landau resonances in the spectra of rubidium Rydberg atoms in crossed electric and magnetic fields," *Phys. Rev. A*, vol. 44, p. 1898, 1991.

[95] Raithel, G., Fauth, M., and Walther, H., "Atoms in strong crossed electric and magnetic fields: Evidence for states with large electric-dipole moments," *Phys. Rev. A*, vol. 47, p. 419, 1993.

[96] Robinson, P. J. and Holbrok, K. A., *Unimolecular Reactions.* Wiley, NY, 1972.

[97] Rom-Kedar, V. and Zaslavsky, G., "Islands of accelerator modes and homoclinic tangles," *Chaos*, vol. 9, p. 697, 1999.

[98] Ruelle, D., "The Lorenz attractor and the problem of turbulence," in *Turbulence and Navier Stokes Equations* (Teman, R., ed.), N.Y.: Springer, 1976.

[99] Ruelle, D., *Statistical Mechanics, Thermodynamic Formalism.* Reading, MA: Addison-Wesley, 1978.

[100] Sadovskii, D. A. and Zhilinskii, B. I., "Tuning the hydrogen atom in crossed fields between the Zeeman and Stark limits," *Phys. Rev. A*, vol. 57, no. 4, pp. 2867–2884, 1998.

[101] Schmelcher, P., "Delocalization of excitons in a magnetic field," *Phys. Rev. B*, vol. 48, p. 14642, 1993.

[102] Semparithi, A. and Keshavamurthy, S., "Intramolecular vibrational energy redistribution as state space diffusion: Classical-quantum correspondence," *J. Chem. Phys.*, vol. 125, p. 141101, 2006.

[103] Shchekinova, E., Chandre, C., Lan, Y., and Uzer, T., "Analyzing intramolecular dynamics by Fast Lyapunov Indicators," *J. Chem. Phys.*, vol. 121, p. 3471, 2004.

[104] Simó, C., "Effective computations in celestial mechanics and astrodynamics," in *Modern Methods of Analytical Mechanics and their Applications* (Rumyantsev, V. V. and Karapetyan, A. V., eds.), vol. 387 of *CISM Courses and Lectures*, N.Y.: Springer, 1998.

[105] Sinai, Y. G., "," *Acta. Phys. Aust. Suppl.*, vol. X, p. 575, 1973.

[106] Skodje, R. T. and Davis, M. J., "A phase space analysis of the collinear I+HI reaction," *J. Chem. Phys.*, vol. 88, no. 4, pp. 2429–2456, 1988.

[107] Smale, S., "Differentiable dynamical systems," *Bull. Amer. Math. Soc.*, vol. 73, pp. 747–817, 1967.

[108] Smale, S., *The Mathematics of Time.* N.Y.: Springer, 1980.

[109] Solov'ev, E. A., "Second-order perturbation theory for a hydrogen atom in crossed electric and magnetic fields," *Sov. Phys. JETP*, vol. 58, no. 1, pp. 63–66, 1983.

[110] Starace, A. F., "Quasi-Landau spectrum of a hydrogen like atom in a high magnetic field," *J. Phys. B*, vol. 6, no. 4, pp. 585–590, 1973.

[111] Stiefel, E. L. and Scheifele, G., *Linear and Regular Celestial Mechanics.* N.Y.: Springer, 1971.

[112] Tanner, G., Hansen, K., and Main, J., "The semiclassical resonance spectrum of hydrogen in a constant magnetic field," *Nonlinearity*, vol. 9, pp. 1641–1670, 1996.

[113] Tennyson, J. L., Lieberman, M. A., and Lichtenberg, A. J., "Diffusion in near-integrable Hamiltonian systems with three degrees of freedom," in *Nonlinear Dynamics and the Beam-Beam Interaction* (Month, M. and Herrera, J. C., eds.), vol. 57 of *AIP Conference Proceedings*, (Brookhaven National Laboratory), pp. 272–301, American Institute of Physics, American Institute of Physics, 1979.

[114] Toda, M., "Global aspects of chemical reactions in multidimensional phase space," *Adv. Chem. Phys.*, vol. 130A, p. 337, 2005.

[115] Turco, R. P., Whitten, R. C., Toon, O. B., Pollack, J. B., and Hamill, P., "OCS, stratospheric aerosols and climate," *Nature*, vol. 283, pp. 283–285, 1980.

[116] Uzer, T., "Rydberg electrons in crossed fields: A paradigm for nonlinear dynamics beyond two degrees of freedom," *Physica Scripta*, vol. T90, p. 176, 2001.

[117] Uzer, T., Jaffé, C., Palacián, J., Yanguas, P., and Wiggins, S., "The geometry of reaction dynamics," *Nonlinearity*, vol. 15, p. 957, 2002.

[118] von Milczewski, J., Diercksen, G. H. F., and Uzer, T., "Intramanifold chaos in Rydberg atoms in external fields," *Phys. Rev. Lett.*, vol. 73, pp. 2428–2431, 1994.

[119] von Milczewski, J., Diercksen, G. H. F., and Uzer, T., "Computation of the Arnol'd web for the hydrogen atom in crossed electric and magnetic fields," *Phys. Rev. Lett.*, vol. 76, p. 2890, 1996.

[120] Wiebusch, G., Main, J., Krüger, K., Rottke, H., Holle, A., and Welge, K. H., "Hydrogen atom in crossed magnetic and electric fields," *Phys. Rev. Lett.*, vol. 62, pp. 2821–2824, 1989.

[121] Wiggins, S., *Introduction to Applied Nonlinear Dynamical Systems and Chaos*, vol. 2 of *Texts in Applied Mathematics*. Springer, 1990.

[122] Yeazell, J. A., Raithel, G., Marmet, L., Held, H., and Walther, H., "Observation of wave packet motion along quasi-Landau orbits," *Phys. Rev. Lett.*, 1993.

[123] Zaslavsky, G. M., *Hamiltonian Chaos and Fractional Dynamics*. Oxford: Oxford University Press, 2005.

[124] Zaslavsky, G., "Chaos, fractional kinetics, and anomalous transport," *Phys. Rep.*, vol. 371, pp. 461–580, 2002.

VITA

Rytis Paškauskas was born in Vilnius, Lithuania on April 9, 1977. He received his B.S. in Physics from the University of Vilnius in 1999 and came to Georgia Tech School of Physics in Fall 2000.